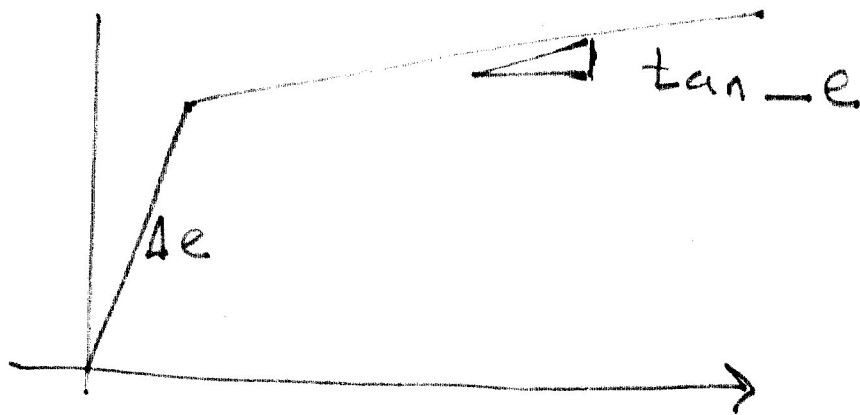


Constitutive Modeling in WARP 3D



- 1) Isotropic hardening $\beta = 1.0$

$$H' = E E_T / (E - E_T)$$

Yield stress increases proportional to plastic modulus.

- 2) Kinematic Hardening $\beta = 0.0$
 the yield surface remains constant but translates and translation is governed by $H' = E E_T / (E - E_T)$

- 3) $0 < \beta < 1$ part of the hardening is isotropic and part is kinematic.
 $\beta = .25$ means 25% of hardening is kinematic.

E_T = target modulus

E = Young's modulus

Notation in Wang 3-D manual
VARP3D

$$\xi' = t' - \alpha$$

$$\frac{\xi' \xi'}{2} - k^2 = 0$$

$$\dot{d} = \dot{d}^e + \dot{d}^p$$

$$\vec{n} = \frac{\xi'}{\|\xi'\|}$$

$$\dot{d}^p = \dot{\lambda} n \quad \dot{\lambda} \geq 0$$

OUR NOTATION

$$\xi' = S_{ij} - \alpha_{ij}$$

$$\frac{(S_{ij} - \alpha_{ij})(S_{ij} - \alpha_{ij})}{2} - k^2 = 0$$

$$\dot{\epsilon} = \dot{\epsilon}^e + \dot{\epsilon}^p$$

$$n_{kl} = \frac{S_{kl} - \alpha_{kl}}{\sqrt{(S_{ij} - \alpha_{ij})(S_{ij} - \alpha_{ij})}}$$

$$n_k = \frac{S_{kl} - \alpha_{kl}}{\sqrt{2}}$$

$$\dot{\epsilon}_{ij}^p = \dot{\lambda} n_{kl}$$

$$\text{or } \dot{\epsilon}^p = \frac{1}{H} \langle S_{kl} n_{kl} \rangle$$

H = plastic modulus

Other Material Models in WARP3D

Gurson:

$$g(\sigma_e, \sigma_m, \bar{\sigma}, f)$$

$$= \left(\frac{\sigma_e}{\bar{\sigma}} \right)^2 + 2q_1 f \cosh\left(\frac{3q_2 \sigma_m}{2\bar{\sigma}} \right) - (1 + q_3 f^2) = 0$$

$\bar{\sigma}$ = Mises of matrix

σ_m = mean (macroscopic) stress.

σ_e = Effective stress of composite (matrix + voids)

q_1, q_2, q_3 = constants.

f = void volume fraction.

$$df = df_{\text{growth}} + df_{\text{nucleation}}$$

$$df_{\text{growth}} = (1-f) d\epsilon^P : I = (1-f) d\epsilon^P \frac{P}{R}$$

$$df_{\text{nucleation}} = A(\bar{\epsilon}^P) d\bar{\epsilon}^P$$

$$\rightarrow A(\bar{\epsilon}^P) = \frac{f_N}{S_N \sqrt{2\pi}} \exp\left[-\frac{1}{2} \left(\frac{\bar{\epsilon}^P - \epsilon_N}{S_N}\right)^2\right]$$

← Chu - Needleman form of A

f_N = void nucleating particles

S_N = standard deviation

$\bar{\epsilon}^P$ = effective plastic strain

P. 3-7-4 Table 3.7 provides the constants for this model.

Strain Rate Dependent Response

$$\dot{\epsilon}_{ij}^P = D \left[\left(\frac{\bar{\sigma}}{\sigma_e} \right)^m - 1 \right] S_{ij}$$

$$D \approx 1.0$$

$$m = 35$$

$\sigma_e = \text{const} = \text{normalized yield stress value} \approx \text{measure of strength}$

This is a power law visco-plastic model. This is in effect similar to the Bodner model we discussed earlier. Depending on the value of m different rate dependencies can be accounted for

$\bar{\sigma}$ = Effective stress.

Cohesive Zone Modeling

3.8 Material Model Type: *cohesive*

This material model idealizes the fracture process in solids as the gradual separation across initially thin and coincident surfaces which may in general be non-planar. The loss of cohesion and thus crack formation-extension within a solid may be viewed as the progressive decay of otherwise intact tension and shear tractions across the adjacent surfaces. The introduction of interface constitutive models that determine the current normal and shear tractions from relative displacement jumps across the surfaces provides a description for the progressive fracture process. At sufficiently large displacement jumps across the interface surfaces, the models degrade the tractions to zero thereby creating new, traction-free surfaces within the volumetric finite element model. Further, the *cohesive* zone model introduces an intrinsic length-scale in the local fracture process via the specified *cohesive*-fracture energy which enables fracture process zones on the specimen-component scale to evolve as a natural outcome of the computations.

Cohesive Zone Modeling

2 Interface Model

Attention is directed toward an interface supporting a nominal traction field \mathbf{T} (force/unit reference area) which, in general, has both normal and shearing components. Two material points, A and B , initially on opposite sides of the interface, are considered and the interfacial traction is taken to depend only on the displacement difference across the interface, $\Delta\mathbf{u}_{AB}$. At each point of the interface, we define

$$U_n = \mathbf{n} \cdot \Delta\mathbf{u}_{AB}, \quad U_t = \mathbf{t} \cdot \Delta\mathbf{u}_{AB}, \quad U_b = \mathbf{b} \cdot \Delta\mathbf{u}_{AB} \quad (2.1)$$

and

$$T_n = \mathbf{n} \cdot \mathbf{T}, \quad T_t = \mathbf{t} \cdot \mathbf{T}, \quad T_b = \mathbf{b} \cdot \mathbf{T} \quad (2.2)$$

$\Psi (\Delta_n, \Delta_t, q)$ is the structure of the potential function.

$$T_n = \frac{\partial \Psi}{\partial \Delta_n} \quad T_t = \frac{\partial \Psi}{\partial \Delta_t}$$

are the tractions

Traction separation curves are

$$T_n - \Delta_n \quad \text{and} \quad T_t - \Delta_t$$

Fracture Energies are

$$\Gamma_n = \int_0^{\delta_n} T_n (\Delta_n, \Delta_t = 0) d\Delta_n$$

$$\Gamma_t = \int_0^{\delta_t} T_t (\Delta_n = 0, \Delta_t) d\Delta_t$$

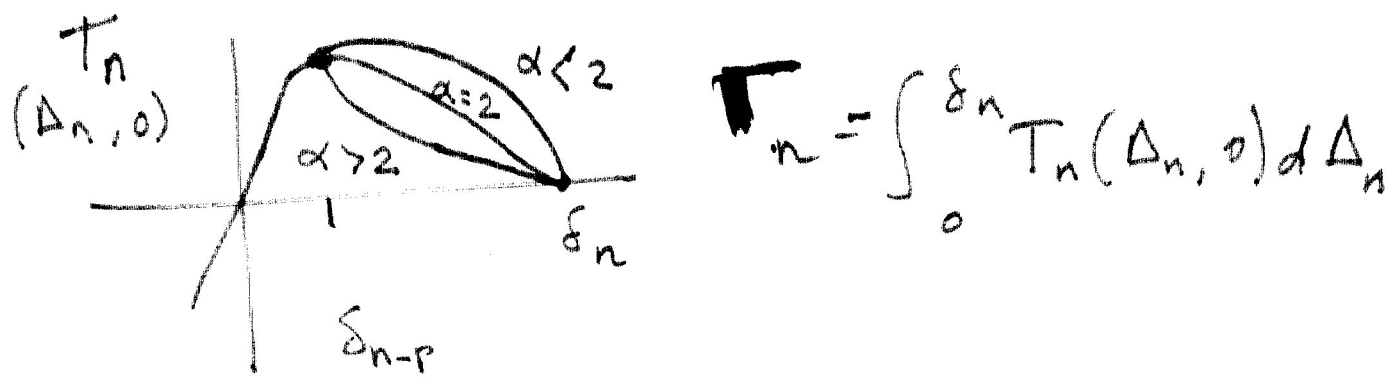
δ_n denotes the value of Δ_n when the normal traction T_n degrades to zero.

$\bar{T} - \bar{\Delta}$ effective traction - displacement relationship is of the form

$$\text{such that } \bar{\Delta} = \sqrt{\beta^2 \Delta_t^2 + \Delta_n^2}$$

where β is a scalar constant, to assign a weight factor to the shear mode contribution.

Park - Paulino-Roesler



$$\Gamma_n = \int_0^{\epsilon_n} T_n(\Delta_n, 0) d\Delta_n$$

Complete failure occurs when $T_n = 0$
 Complete shear failure occurs when $T_t = 0$
 The area Γ_n defines mode I toughness.
 The shape parameters are introduced to define material softening response.
 Material input parameters are provided in Table 3.8.2 of the Warp3D user's guide.

Input parameters are

- $T_{n-p}, T_{t-p}, \Gamma_n, \Gamma_t, \alpha, \beta,$
- $\lambda_n, \lambda_t,$ stiffness compression multiplier

Exponential Option (p. 3.8-10)

- 9.

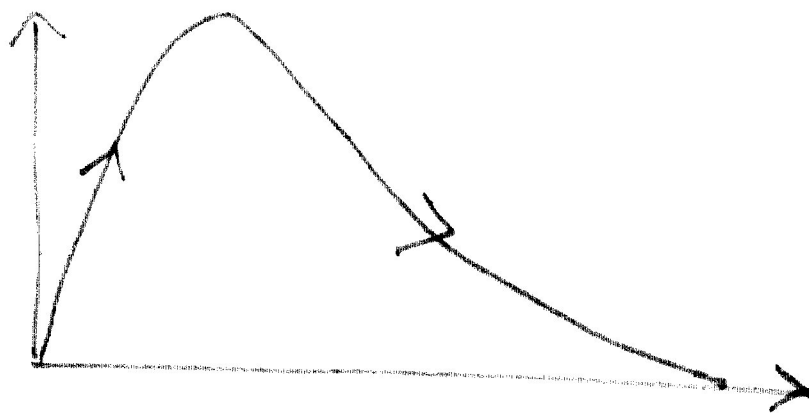
$$\bar{\Delta} = \sqrt{\beta^2 \Delta_t^2 + \Delta_n^2} = \text{Displacement Jump across interface } (\beta \text{ scalar parameter})$$

→
resultant traction vector

$$\bar{T} = \frac{\bar{T}}{\bar{\Delta}} (\beta^2 \Delta_t + \Delta_n n)$$

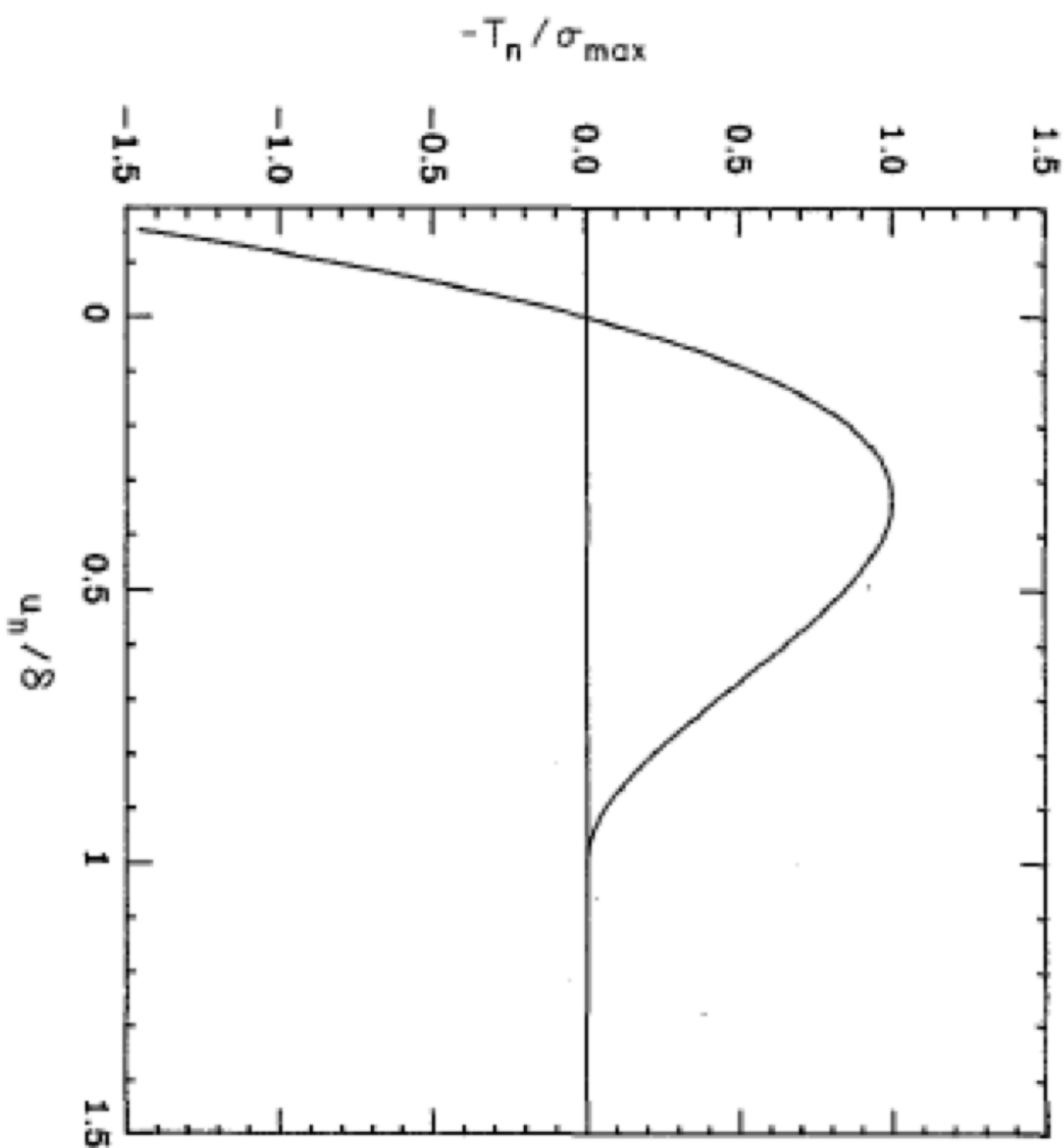
$$\bar{T} = \sqrt{\beta^{-2} \|T_t\|^2 + T_n^2}$$

\bar{T}
 \bar{T}_p



$$\bar{T} = \exp(1.0) \bar{T}_p \frac{\bar{\Delta}}{\bar{\Delta}_p} \exp\left(-\frac{\bar{\Delta}}{\bar{\Delta}_p}\right)$$

This option combines the normal & shear tractions into a single effective traction (\bar{T}). A single traction-separation curve is then used.



In equations (2.1) and (2.2), \mathbf{n} , \mathbf{l} , \mathbf{b} form a right-hand coordinate system chosen so that positive u_n corresponds to increasing interfacial separation and negative u_n corresponds to decreasing interfacial separation.

The mechanical response of the interface is described through a constitutive relation that gives the dependence of the tractions T_n , T_t , and T_b on u_n , u_t , and u_b . Here, this response is specified in terms of a potential $\phi(u_n, u_t, u_b)$, where

$$\phi(u_n, u_t, u_b) = - \int_0^{u_n} [T_n du_n + T_t du_t + T_b du_b] \quad (2.3)$$

As the interface separates, the magnitude of the tractions increases, achieves a maximum, and ultimately falls to zero when complete separation occurs. The magnitude of the tractions is taken to increase monotonically for negative u_n . Relative shearing across the interface leads to the development of shear tractions, but the dependence of the shear tractions on u_t and u_b is taken to be linear. The specific potential function used is

$$\begin{aligned}
& \phi(u_n, u_r, u_b) \\
&= \frac{27}{4} \sigma_{\max} \delta \left\{ \frac{1}{2} \left(\frac{u_n}{\delta} \right)^2 \left[1 - \frac{4}{3} \left(\frac{u_n}{\delta} \right) + \frac{1}{2} \left(\frac{u_n}{\delta} \right)^2 \right] \right. \\
&\quad \left. + \frac{1}{2} \alpha \left(\frac{u_r}{\delta} \right)^2 \left[1 - 2 \left(\frac{u_n}{\delta} \right) + \left(\frac{u_n}{\delta} \right)^2 \right] \right. \\
&\quad \left. + \frac{1}{2} \alpha \left(\frac{u_b}{\delta} \right)^2 \left[1 - 2 \left(\frac{u_n}{\delta} \right) + \left(\frac{u_n}{\delta} \right)^2 \right] \right\} \quad (2.4)
\end{aligned}$$

for $u_n \leq \delta$, where σ_{\max} is the maximum traction carried by the interface undergoing a purely normal separation ($u_r = u_b = 0$), δ is a characteristic length and α specifies the ratio of shear to normal stiffness of the interface. When $u_n > \delta$, $\phi = \phi_{\text{sep}}$, where ϕ_{sep} is the work of separation.

The interfacial tractions are obtained by differentiating equation (2.4) to give

$$\begin{aligned}
T_n = & \frac{-27}{4} \sigma_{\max} \left\{ \left(\frac{u_n}{\delta} \right) \left[1 - 2 \left(\frac{u_n}{\delta} \right) + \left(\frac{u_n}{\delta} \right)^2 \right] \right. \\
& \left. + \alpha \left(\frac{u_r}{\delta} \right)^2 \left[\left(\frac{u_n}{\delta} \right) - 1 \right] + \alpha \left(\frac{u_b}{\delta} \right)^2 \left[\left(\frac{u_n}{\delta} \right) - 1 \right] \right\} \quad (2.5)
\end{aligned}$$

$$T_t = \frac{-27}{4} \sigma_{\max} \left\{ \alpha \left(\frac{u_t}{\delta} \right) \left[1 - 2 \left(\frac{u_n}{\delta} \right) + \left(\frac{u_n}{\delta} \right)^2 \right] \right\} \quad (2.6)$$

$$T_b = \frac{-27}{4} \sigma_{\max} \left\{ \alpha \left(\frac{u_b}{\delta} \right) \left[1 - 2 \left(\frac{u_n}{\delta} \right) + \left(\frac{u_n}{\delta} \right)^2 \right] \right\} \quad (2.7)$$

for $u_n \leq \delta$ and $T_n = T_t = T_b = 0$ when $u_n > \delta$.

The motivation for choosing a potential of the form (2.4) is to obtain a response of the type shown in Fig. 1 where the normal traction, T_n , is plotted as a function of u_n with $u_t = u_b = 0$. The particular functional form (2.4) was chosen for analytical convenience; other forms can readily be used in the present framework. As can be seen in Fig. 1, the maximum interfacial stress is achieved at $u_n = \delta/3$ and complete separation occurs when $u_n = \delta$. The work of separation (in Fig. 1, the area under the curve between $u_n = 0$ and $u_n = \delta$) is

$$\phi_{\text{sep}} = 9\sigma_{\max} \delta / 16 \quad (2.8)$$

With $u_t \neq u_b \neq 0$, T_n , T_t , and T_b all vanish when $u_n = \delta$ so that, in general, δ serves as a characteristic length. Furthermore, due to the existence of a potential, equation (2.8) gives the work of separation regardless of the path. Equation (2.8) is regarded as defining the characteristic interface length δ by $\delta = 16 \phi_{\text{sep}} / 9 \sigma_{\max}$. Although δ has dimensions of length, it does not necessarily correspond to any physical distance.

The interface description adopted here is a phenomenological one characterized by the three parameters σ_{\max} , δ and α . In the numerical examples parameter values representative of iron carbide particles in spheroidized carbon steels will be used. Based on the results of Argon et al. (1975), Goods and Brown (1979), and Fisher and Gurland (1981), the order of magnitude of δ can be estimated for this case; $\sigma_{\max} \approx 10^3$ MPa and ϕ_{sepp} is in the range of 1 to 10 Jm^{-2} so that $\delta \approx 10^{-9}$ to 10^{-8} m .

There does not appear to be any similar basis for specifying a value of the shear stiffness parameter α . In the calculations carried out here, the value of α is arbitrarily set to 10, the presumption being that the interface exhibits a stiffer response for relative sliding than for the normal displacement leading to separation. However, as will be illustrated subsequently, the numerical results in the specific cases analyzed are not very sensitive to the choice of α .

The finite element analysis is based on a convected coordinate Lagrangian formulation of the field equations with the initial unstressed state taken as reference. All field quantities are considered to be functions of convected coordinates, x^i , which serve as particle labels, and time t . This formulation has been employed extensively in previous finite element analyses, e.g., Needleman (1972) and Tvergaard (1976), and is reviewed by Needleman (1982).

Attention is confined to quasi-static deformations and, with body forces neglected, the principal of virtual work is written as

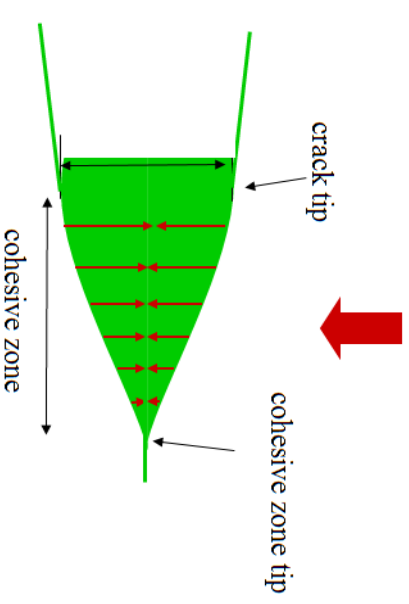
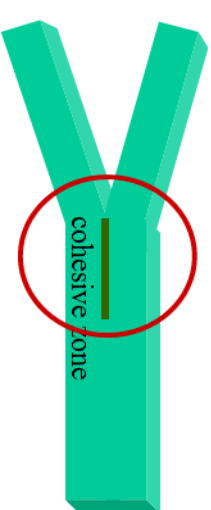
$$\int_V \tau^{ij} \delta E_{ij} dV + \int_{S_{\text{int}}} \delta \phi dS = \int_{S_{\text{ext}}} T^i \delta u_i dS \quad (3.1)$$

Here, τ^{ij} are the contravariant components of Kirchhoff stress ($\tau = J\sigma$, with σ the Cauchy stress) on the deformed convected coordinate net, V , S_{ext} , and S_{int} are the total volume (inclusion plus matrix), external surface and interfacial surface, respectively, of the body in the reference configuration, and

Cohesive Zone Modeling

Overview

- Theoretical basis: cohesive zone modeling of fracture
- Dugdale (1960), Barenblatt (1962)
- First general (2D) FE modeling of fracture by Alan Needleman (1987)
- CES used same approach in 1970s to model crack propagation in concrete beams (Hillerborg)
- Much research over past 20 yrs
- Driven by apparent simplicity of approach



A. Hillerborg, et al, "Analysis of crack formation and crack growth in concrete by means of fracture mechanics and finite elements," Cement and concrete research, Vol 6, 773-782, 1976



A. Needleman

A Continuum Model for Void Nucleation by Inclusion Debonding

A. Needleman

Division of Engineering,
Brown University,
Providence, RI 02912

A cohesive zone model, taking full account of finite geometry changes, is used to provide a unified framework for describing the process of void nucleation from initial debonding through complete decohesion. A boundary value problem simulating a periodic array of rigid spherical inclusions in an isotropically hardening elastic-viscoplastic matrix is analyzed. Dimensional considerations introduce a characteristic length into the formulation and, depending on the ratio of this characteristic length to the inclusion radius, decohesion occurs either in a "ductile" or "brittle" manner. The effect of the triaxiality of the imposed stress state on nucleation is studied and the numerical results are related to the description of void nucleation within a phenomenological constitutive framework for progressively cavitating solids.

1 Introduction

The nucleation of voids from inclusions and second phase particles plays a key role in limiting the ductility and toughness of plastically deforming solids, including structural metals and composites. The voids initiate either by inclusion cracking or by decohesion of the interface, but here attention is confined to consideration of void nucleation by interfacial decohesion.

Theoretical descriptions of void nucleation from second phase particles have been developed based on both continuum and dislocation concepts, e.g., Brown and Stobbs (1971), Argon et al. (1975), Chang and Asaro (1978), Goods and Brown (1979), and Fisher and Gurland (1981). These models have focussed on critical conditions for separation and have not explicitly treated propagation of the debonded zone along the interface. Interface debonding problems have been treated within the context of continuum linear elasticity theory; for example, the problem of separation of a circular cylindrical inclusion from a matrix has been solved for an interface that supports neither shearing nor tensile normal tractions (Keer et al., 1973). The growth of a void at a rigid inclusion has been analyzed by Taya and Patterson (1982), for a nonlinear viscous solid subject to overall uniaxial straining and with the strength of the interface neglected.

The model introduced in this investigation is aimed at describing the evolution from initial debonding through complete separation and subsequent void growth within a unified framework. The formulation is a purely continuum one using a cohesive zone (Barenblatt, 1962; Dugdale, 1960) type model for the interface but with full account taken of finite geometry

changes. Constitutive relations are specified independently for the matrix, the inclusion, and the interface. The constitutive equation for the interface is such that, with increasing interfacial separation, the traction across the interface reaches a maximum, decreases, and eventually vanishes so that complete decohesion occurs. Since the mechanical response of the interface is specified in terms of both a critical interfacial strength and the work of separation per unit area, dimensional considerations introduce a characteristic length.

Arbitrary inclusion geometries and quite general matrix and inclusion constitutive relations can be incorporated into the formulation. The specific boundary value problem analyzed here is one simulating a periodic array of rigid spherical inclusions in an isotropically hardening elastic-viscoplastic matrix. The aggregate is subject to both axial and radial stresses and a circular cylinder surrounding each inclusion is required to remain cylindrical throughout the deformation history in order to simulate the constraint of the surrounding material. By considering histories with different ratios of radial to axial stress, the effect of stress triaxiality on nucleation is studied. The numerical results are related to the description of void nucleation within the phenomenological constitutive framework of Gurson (1975, 1977).

2 Interface Model

Attention is directed toward an interface supporting a nominal traction field \mathbf{T} (force/unit reference area) which, in general, has both normal and shearing components. Two material points, A and B , initially on opposite sides of the interface, are considered and the interfacial traction is taken to depend only on the displacement difference across the interface, $\Delta \mathbf{u}_{AB}$. At each point of the interface, we define

$$u_n = \mathbf{n} \cdot \Delta \mathbf{u}_{AB}, \quad u_t = \mathbf{t} \cdot \Delta \mathbf{u}_{AB}, \quad u_b = \mathbf{b} \cdot \Delta \mathbf{u}_{AB} \quad (2.1)$$

and

$$T_n = \mathbf{n} \cdot \mathbf{T}, \quad T_t = \mathbf{t} \cdot \mathbf{T}, \quad T_b = \mathbf{b} \cdot \mathbf{T} \quad (2.2)$$

Contributed by the Applied Mechanics Division for presentation at the Winter Annual Meeting, Boston, MA, December 13-18, 1987, of the American Society of Mechanical Engineers.

Discussion on this paper should be addressed to the Editorial Department, ASME, United Engineering Center, 345 East 47th Street, New York, NY, 10017, and will be accepted until two months after final publication of the paper itself in the JOURNAL OF APPLIED MECHANICS. Manuscript received by ASME Applied Mechanics Division, October 28, 1986; final revision, February 17, 1987. Paper No. 87-WA/APM-9.

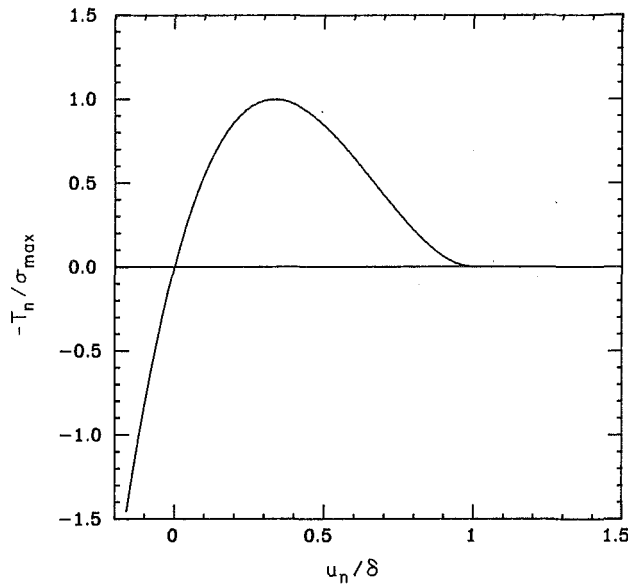


Fig. 1 Normal traction across the interface as a function of u_n with $u_t = u_b = 0$

In equations (2.1) and (2.2), \mathbf{n} , \mathbf{t} , \mathbf{b} form a right-hand coordinate system chosen so that positive u_n corresponds to increasing interfacial separation and negative u_n corresponds to decreasing interfacial separation.

The mechanical response of the interface is described through a constitutive relation that gives the dependence of the tractions T_n , T_t , and T_b on u_n , u_t , and u_b . Here, this response is specified in terms of a potential $\phi(u_n, u_t, u_b)$, where

$$\phi(u_n, u_t, u_b) = - \int_0^u [T_n du_n + T_t du_t + T_b du_b] \quad (2.3)$$

As the interface separates, the magnitude of the tractions increases, achieves a maximum, and ultimately falls to zero when complete separation occurs. The magnitude of the tractions is taken to increase monotonically for negative u_n . Relative shearing across the interface leads to the development of shear tractions, but the dependence of the shear tractions on u_t and u_b is taken to be linear. The specific potential function used is

$$\begin{aligned} \phi(u_n, u_t, u_b) &= \frac{27}{4} \sigma_{\max} \delta \left\{ \frac{1}{2} \left(\frac{u_n}{\delta} \right)^2 \left[1 - \frac{4}{3} \left(\frac{u_n}{\delta} \right) + \frac{1}{2} \left(\frac{u_n}{\delta} \right)^2 \right] \right. \\ &\quad + \frac{1}{2} \alpha \left(\frac{u_t}{\delta} \right)^2 \left[1 - 2 \left(\frac{u_n}{\delta} \right) + \left(\frac{u_n}{\delta} \right)^2 \right] \\ &\quad \left. + \frac{1}{2} \alpha \left(\frac{u_b}{\delta} \right)^2 \left[1 - 2 \left(\frac{u_n}{\delta} \right) + \left(\frac{u_n}{\delta} \right)^2 \right] \right\} \quad (2.4) \end{aligned}$$

for $u_n \leq \delta$, where σ_{\max} is the maximum traction carried by the interface undergoing a purely normal separation ($u_t = u_b = 0$), δ is a characteristic length and α specifies the ratio of shear to normal stiffness of the interface. When $u_n > \delta$, $\phi = \phi_{\text{sep}}$, where ϕ_{sep} is the work of separation.

The interfacial tractions are obtained by differentiating equation (2.4) to give

$$\begin{aligned} T_n &= \frac{-27}{4} \sigma_{\max} \left\{ \left(\frac{u_n}{\delta} \right) \left[1 - 2 \left(\frac{u_n}{\delta} \right) + \left(\frac{u_n}{\delta} \right)^2 \right] \right. \\ &\quad \left. + \alpha \left(\frac{u_t}{\delta} \right)^2 \left[\left(\frac{u_n}{\delta} \right) - 1 \right] + \alpha \left(\frac{u_b}{\delta} \right)^2 \left[\left(\frac{u_n}{\delta} \right) - 1 \right] \right\} \quad (2.5) \end{aligned}$$

$$T_t = \frac{-27}{4} \sigma_{\max} \left\{ \alpha \left(\frac{u_t}{\delta} \right) \left[1 - 2 \left(\frac{u_n}{\delta} \right) + \left(\frac{u_n}{\delta} \right)^2 \right] \right\} \quad (2.6)$$

$$T_b = \frac{-27}{4} \sigma_{\max} \left\{ \alpha \left(\frac{u_b}{\delta} \right) \left[1 - 2 \left(\frac{u_n}{\delta} \right) + \left(\frac{u_n}{\delta} \right)^2 \right] \right\} \quad (2.7)$$

for $u_n \leq \delta$ and $T_n = T_t = T_b = 0$ when $u_n > \delta$.

The motivation for choosing a potential of the form (2.4) is to obtain a response of the type shown in Fig. 1 where the normal traction, T_n , is plotted as a function of u_n with $u_t = u_b = 0$. The particular functional form (2.4) was chosen for analytical convenience; other forms can readily be used in the present framework. As can be seen in Fig. 1, the maximum interfacial stress is achieved at $u_n = \delta/3$ and complete separation occurs when $u_n = \delta$. The work of separation (in Fig. 1, the area under the curve between $u_n = 0$ and $u_n = \delta$) is

$$\phi_{\text{sep}} = 9 \sigma_{\max} \delta / 16 \quad (2.8)$$

With $u_t \neq u_b \neq 0$, T_n , T_t , and T_b all vanish when $u_n = \delta$ so that, in general, δ serves as a characteristic length. Furthermore, due to the existence of a potential, equation (2.8) gives the work of separation regardless of the path. Equation (2.8) is regarded as defining the characteristic interface length δ by $\delta = 16 \phi_{\text{sep}} / 9 \sigma_{\max}$. Although δ has dimensions of length, it does not necessarily correspond to any physical distance.

The interface description adopted here is a phenomenological one characterized by the three parameters σ_{\max} , δ and α . In the numerical examples parameter values representative of iron carbide particles in spheroidized carbon steels will be used. Based on the results of Argon et al. (1975), Goods and Brown (1979), and Fisher and Gurland (1981), the order of magnitude of δ can be estimated for this case; $\sigma_{\max} \approx 10^3$ MPa and ϕ_{sep} is in the range of 1 to 10 Jm^{-2} so that $\delta \approx 10^{-9}$ to 10^{-8} m.

There does not appear to be any similar basis for specifying a value of the shear stiffness parameter α . In the calculations carried out here, the value of α is arbitrarily set to 10, the presumption being that the interface exhibits a stiffer response for relative sliding than for the normal displacement leading to separation. However, as will be illustrated subsequently, the numerical results in the specific cases analyzed are not very sensitive to the choice of α .

3 Finite Element Formulation

The finite element analysis is based on a convected coordinate Lagrangian formulation of the field equations with the initial unstressed state taken as reference. All field quantities are considered to be functions of convected coordinates, x^i , which serve as particle labels, and time t . This formulation has been employed extensively in previous finite element analyses, e.g., Needleman (1972) and Tvergaard (1976), and is reviewed by Needleman (1982).

Attention is confined to quasi-static deformations and, with body forces neglected, the principal of virtual work is written as

$$\int_V \tau^{ij} \delta E_{ij} dV + \int_{S_{\text{int}}} \delta \phi dS = \int_{S_{\text{ext}}} T^i \delta u_i dS \quad (3.1)$$

Here, τ^{ij} are the contravariant components of Kirchhoff stress ($\tau = J\sigma$, with σ the Cauchy stress) on the deformed convected coordinate net, V , S_{ext} , and S_{int} are the total volume (inclusion plus matrix), external surface and interfacial surface, respectively, of the body in the reference configuration, and

$$T^i = (\tau^{ij} + \tau^{kj} u_{,k}^i) \nu_j \quad (3.2)$$

$$E_{ij} = \frac{1}{2} (u_{i,j} + u_{j,i} + u_{,i}^k u_{,j}^k) \quad (3.3)$$

where ν is the surface normal in the reference configuration, u_j are the components of the displacement vector on base vectors

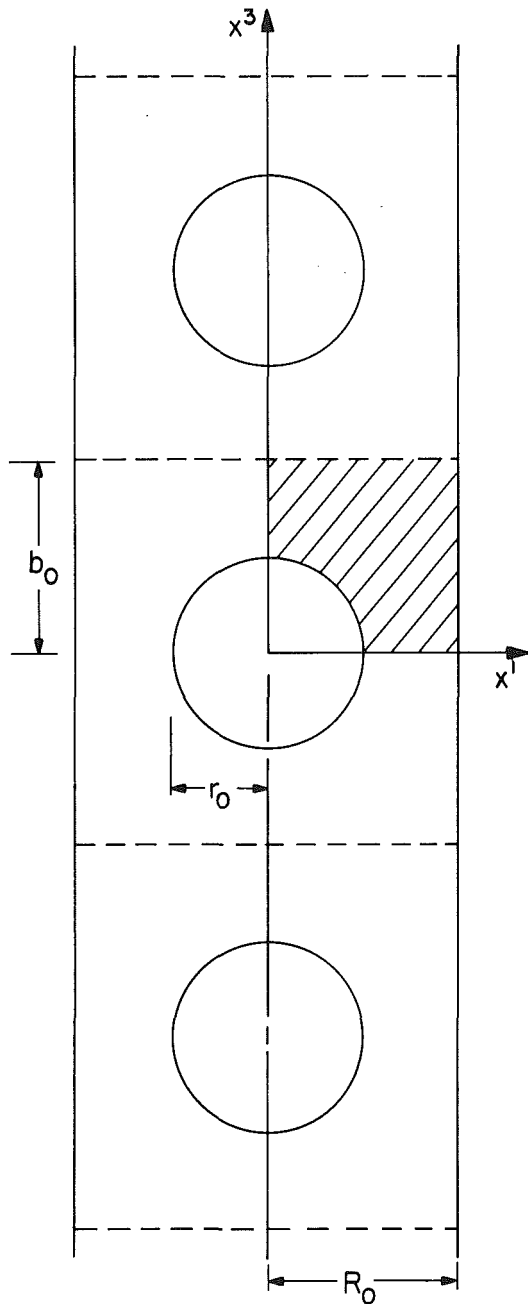


Fig. 2 Axisymmetric model of a material containing an array of spherical voids. Due to the assumed symmetry, only the shaded quadrant is analyzed numerically.

in the reference configuration and $()_{,i}$ denotes covariant differentiation in the reference frame.

For the specific boundary value problem considered here, we use a cylindrical coordinate system with radial coordinate x^1 , circumferential angle x^2 , and axial coordinate x^3 . As sketched in Fig. 2, we consider spherical particles of radius r_0 located along the axis of a circular cylinder with an initial spacing of $2b_0$ between particle centers. The cylinder has initial radius R_0 and attention is confined to axisymmetric deformations so that all field quantities are independent of x^2 . Furthermore, the circular cylindrical cell surrounding each particle is required to remain a circular cylinder throughout the deformation history and within each cell symmetry is assumed about the cell center line so that only the shaded region is analyzed numerically. As discussed by Tvergaard (1982), this axisymmetric configuration can be considered an

approximation to a three dimensional array of hexagonal cylinders.

The boundary conditions for the axisymmetric region analyzed numerically are

$$\dot{u}^3 = 0, \quad \dot{T}^1 = 0, \quad \dot{T}^2 = 0, \quad \text{on } x^3 = 0 \quad (3.4)$$

$$\dot{u}^3 = \dot{U}_3 = \dot{\epsilon}_\infty b, \quad \dot{T}^1 = 0, \quad \dot{T}^2 = 0, \quad \text{on } x^3 = b_0 \quad (3.5)$$

$$\dot{u}^1 = \dot{U}_1, \quad \dot{T}^3 = 0, \quad \dot{T}^2 = 0, \quad \text{on } x^1 = R_0 \quad (3.6)$$

Here, $(\dot{\quad}) = \partial(\quad)/\partial t$ and $\dot{\epsilon}_\infty$ is a prescribed constant while \dot{U}_1 is determined by the analysis. With these boundary conditions, the deformed circular cylindrical cell has radius $R = R_0 + U_1$, and height $2b = 2b_0 + 2U_3$.

The lateral displacement rate, \dot{U}_1 is determined from the condition that the average macroscopic true stresses acting on the cell follow the proportional history

$$\frac{\Sigma_1}{\Sigma_3} = \frac{\dot{\Sigma}_1}{\dot{\Sigma}_3} = \rho \quad (3.7)$$

with ρ a prescribed constant and

$$\Sigma_1 = \frac{R_0 b_0}{R b} \left\{ \frac{1}{b_0} \int_0^{b_0} [T^1]_{x^1=R_0} dx^3 \right\} \quad (3.8)$$

$$\Sigma_3 = \frac{R_0^2}{R^2} \left\{ \frac{2}{R_0^2} \int_0^{R_0} [T^3]_{x^3=b_0} x^1 dx^1 \right\} \quad (3.9)$$

The matrix material is characterized as an elastic-viscoplastic isotropically hardening solid. The total rate of deformation, \mathbf{D} , is written as the sum of an elastic part, \mathbf{D}^e , and a plastic part \mathbf{D}^p , with

$$\mathbf{D}^e = \frac{1+\nu}{E} \hat{\tau} - \frac{\nu}{E} (\hat{\tau}:\mathbf{I})\mathbf{I} \quad (3.10)$$

$$\mathbf{D}^p = \frac{3\dot{\epsilon}}{2\bar{\sigma}} \tau' \quad (3.11)$$

where $\hat{\tau}$ is the Jaumann rate of Kirchhoff stress, \mathbf{I} is the identity tensor, $\hat{\tau}:\mathbf{I}$ is the trace of $\hat{\tau}$, $\dot{\epsilon}$ is the effective plastic strain rate, E is Young's modulus, ν is Poisson's ratio and

$$\tau' = \tau - \frac{1}{3} (\tau:\mathbf{I})\mathbf{I}, \quad \bar{\sigma}^2 = \frac{3}{2} \tau':\tau' \quad (3.12)$$

$$\dot{\epsilon} = \dot{\epsilon}_0 [\bar{\sigma}/g(\bar{\epsilon})]^{1/m},$$

$$g(\bar{\epsilon}) = \sigma_0 (\bar{\epsilon}/\epsilon_0 + 1)^N, \quad \epsilon_0 = \sigma_0/E \quad (3.13)$$

Here, $\bar{\epsilon} = \int \dot{\epsilon} dt$ and the function $g(\bar{\epsilon})$ represents the effective stress versus effective strain response in a tensile test carried out at a strain-rate such that $\dot{\epsilon} = \dot{\epsilon}_0$. Also, σ_0 is a reference strength and N and m are the strain hardening exponent and strain rate hardening exponent, respectively.

Expanding equation (3.1) about a state of approximate equilibrium gives

$$\begin{aligned} \Delta t \int_V [\hat{\tau}^{ij} \delta E_{ij} + \tau^{ij} \dot{u}_i^k \delta u_{k,j}] dV \\ + \Delta t \int_{S_{\text{int}}} [S^{nn} \dot{u}_n \delta u_n + S^{nt} (\dot{u}_n \delta u_t + \dot{u}_t \delta u_n) \\ + S^{tt} \dot{u}_t \delta u_t] dS = \Delta t \int_{S_{\text{ext}}} \hat{T}^i \delta u_i dS - \left[\int_V \tau^{ij} \delta E_{ij} dV \right. \\ \left. + \int_{S_{\text{int}}} \delta \phi dS - \int_{S_{\text{ext}}} T^i \delta u_i dS \right] \quad (3.14) \end{aligned}$$

where $S^{ij} = \partial^2 \phi / \partial u_i \partial u_j$. In equation (3.14), the integral over S_{int} has been specialized to the case of axisymmetric deformations with the b direction identified with that of the circumferential angle so that $u_b \equiv 0$. The term in square brackets on the right-hand side of equation (3.14) is an equilibrium correction term that vanishes when the known state is an exact equilibrium state.

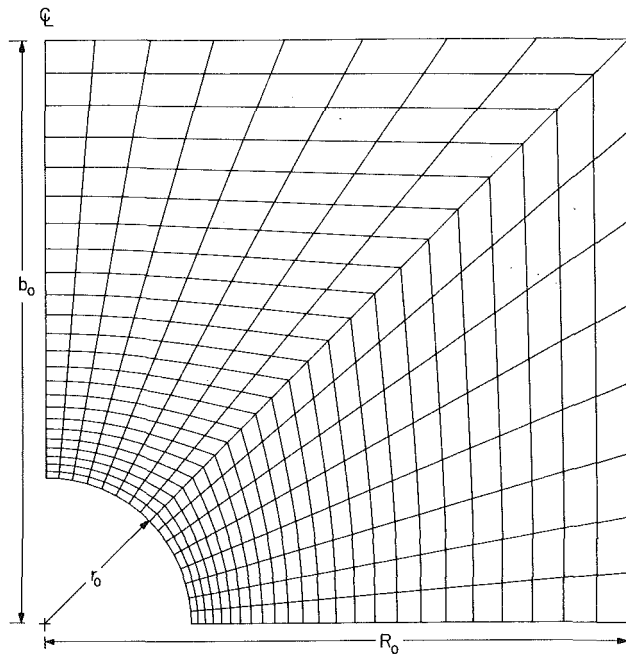


Fig. 3 The 16×24 finite element mesh used in the calculations. Each quadrilateral consists of four linear displacement "crossed" triangular elements.

The set of equations for the unknown displacement rates is obtained by combining equations (3.10) and (3.11) and then using the relation between the Jaumann and convected stress rates in equation (3.14). The finite element mesh used in the numerical calculations is shown in Fig. 3. The mesh has 16 quadrilaterals around the inclusion and 24 quadrilaterals in the radial direction. Each quadrilateral consists of four "crossed" triangles. The circular inclusion is approximated by a polygon consisting of linear segments that are the sides of the elements along the interface. The method for evaluating the integrals along S_{int} in equation (3.14) is similar to an approach used in surface diffusion calculations by Needleman and Rice (1980). The integration scheme uses four Gauss points within each linear segment and the interfacial tractions are evaluated at the Gauss integration points rather than at the finite element nodes. This permits partial debonding within a linear segment.

The deformation history is calculated in a linear incremental manner and, in order to increase the stable time step, the rate tangent modulus method of Peirce et al. (1984) is used. This is a forward gradient method based on an estimate of the plastic strain rate in the interval between t and $t + \Delta t$. The incremental boundary value problem is solved using a combined finite element Rayleigh-Ritz method (Tvergaard, 1976).

In most cases, the prescribed overall strain rate, $\dot{\epsilon}_\infty$ is taken constant and equal to the reference strain rate $\dot{\epsilon}_0$. However, equilibrium solutions do not necessarily exist to the boundary value problem so posed. For a certain range of interface characterizations, equilibrium solutions only exist if U_3 decreases during decohesion. In such cases, the boundary value problem is modified so that equilibrium solutions are sought for increasing interfacial separation and the prescribed velocity condition in equation (3.5) is replaced by $\dot{u}_3 = \text{constant}$ along $x^3 = b_0$; $\dot{\epsilon}_\infty$ then becomes an unknown determined by the solution procedure.

4 Numerical Results

In the numerical calculations carried out here, the inclusion volume fraction and geometry, as well as the matrix material properties, remain fixed; only the interface characteristics are

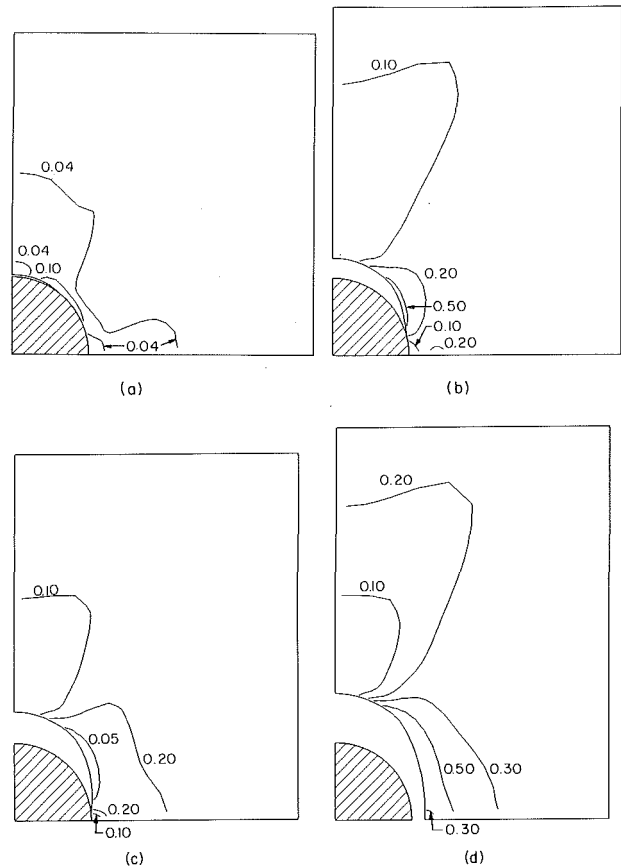


Fig. 4 Contours of constant plastic strain, $\bar{\epsilon}$, in the deformed configuration of the quadrant analyzed numerically. The rigid inclusion is shaded. The volume fraction of inclusions is 1.04 percent. The interface is characterized by $\sigma_{max} = 3\sigma_0$, $b/r_0 = 0.01$, $\alpha = 10.0$ and the stress triaxiality parameter, ρ , in equation (3.7) is 0.5. (a) $\epsilon_a = 0.040$; (b) $\epsilon_a = 0.121$; (c) $\epsilon_a = 0.169$; (d) $\epsilon_a = 0.240$.

varied. The inclusion geometry is specified by $b_0/R_0 = 1$ and $r_0/R_0 = 0.25$, giving an inclusion volume fraction of 1.04 percent. The matrix material properties are $E = 500 \sigma_0$, $\nu = 0.3$, $N = 0.1$, and $m = 0.01$. In most calculations, the value $\sigma_{max} = 3 \sigma_0$ is employed which is a plausible value for iron carbide particles in a spheroidized steel, e.g., with a yield strength of 350 to 450 MPa and an interfacial cohesive strength in the range 1000 to 1400 MPa (Argon et al., 1975; Goods and Brown, 1979; Cialone and Asaro, 1979; and Brownrigg et al., 1983).

Figure 4 shows contours of constant plastic strain, $\bar{\epsilon}$, at various stages of the nucleation process. While the matrix and inclusion remain bonded, the main strain concentration occurs along the inclusion surface at about 45 deg from the tensile axis. Debonding does not begin at the axis of symmetry; it begins at the end of the strain concentration nearest the symmetry axis. The crack rather rapidly propagates to the axis of symmetry and then a spherical cap void opens. Already, at the stage of deformation shown in Fig. 4(a), the maximum normal displacement is on the symmetry axis and there are "dead" zones at 0 deg and 90 deg. As the decohering region propagates toward the midsection, the deformation pattern changes to one where the maximum straining is near the midsection.

Curves of effective stress, Σ_e , versus axial strain, $\epsilon_a = \ln(1 + U_3/b_0)$, are plotted in Fig. 5 for three values of δ/r_0 , where, for the axisymmetric configuration analyzed, we define

$$\Sigma_e = |\Sigma_3 - \Sigma_1|, \quad \Sigma_h = \frac{1}{3} (\Sigma_3 + 2\Sigma_1) \quad (4.1)$$

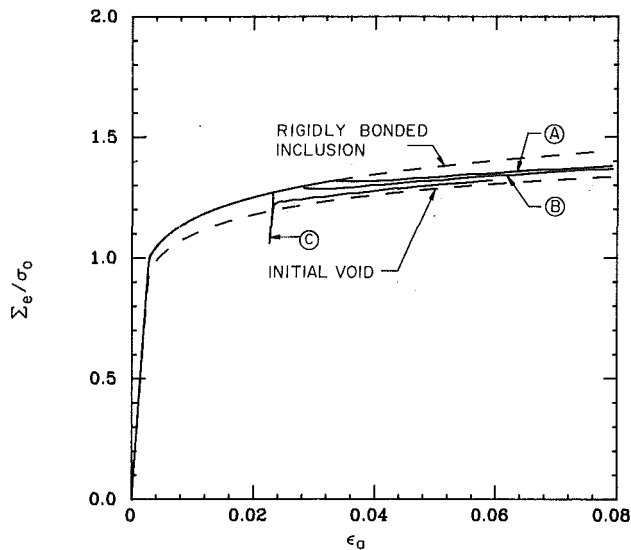


Fig. 5 Curves of aggregate effective stress, Σ_e , versus axial strain, ϵ_a , for a 1.04 percent volume fraction of inclusions with $\rho = 0.5$ in equation (3.7) and using three interface characterizations. In all three cases $\sigma_{\max} = 3\sigma_0$ and $\alpha = 10.0$; (A) $\delta/r_0 = 0.01$; (B) $\delta/r_0 = 0.006$; (C) $\delta/r_0 = 0.002$. For comparison purposes, corresponding curves for a 1.04 percent volume fraction of perfectly bonded inclusions and for a 1.04 percent volume fraction of initial voids are also shown.

With regard to iron carbide particles in spheroidized carbon steels, these values of δ/r_0 correspond to particle sizes of the order of 1 micron (10^{-6} m).

The variation of δ/r_0 can be regarded either in terms of a variation in ϕ_{sep} at fixed particle size or as a variation in particle size at fixed work of separation. A sufficiently small value of δ/r_0 gives rise to "brittle" interface behavior, while larger values lead to a more ductile mode of separation. For comparison purposes, the corresponding curves for a rigidly bonded inclusion and for an initial void are shown.

As debonding progresses, the overall stress-strain behavior changes from that characteristic of a matrix reinforced by rigid inclusions to one weakened by an equal volume fraction of voids. For the larger two values of δ/r_0 , this transition takes place gradually and with increasing extension. As δ/r_0 decreases, the stress drop becomes more abrupt and, for the case with $\delta/r_0 = 0.002$, the stress drop cannot be affected with continued plastic loading. Even though explicit elastic unloading is not incorporated into the material description, the material response is essentially linear elastic during this abrupt stress drop and, as can be seen in Fig. 5, the stress drop occurs with the initial elastic slope. Initial debonding occurs in the element nearest the axis of symmetry, in contrast to the situation for a more ductile interface, where debonding initiates off the axis. The stress drop occurs before initial debonding, when the traction across this interface segment is on the descending branch of the traction versus displacement curve in Fig. 1. After initial debonding, the stress increases, although, as can be seen in Fig. 5, there are slight oscillations (which may be an artifact of the numerics) in the overall stress-strain curve as debonding propagates along the interface.

As illustrated in Fig. 4, void nucleation is a process that occurs over a range of strain. A void nucleation strain, ϵ_N , can be defined in various ways, with the appropriate definition depending on the context in which it is to be used. For example, the void nucleation strain can be identified with the strain at which initial debonding takes place or with the strain at which complete separation occurs. In the phenomenological constitutive framework of Gurson (1975, 1977), a void created by inclusion debonding has been regarded as equivalent to a void occupying the same fraction as the inclusion being

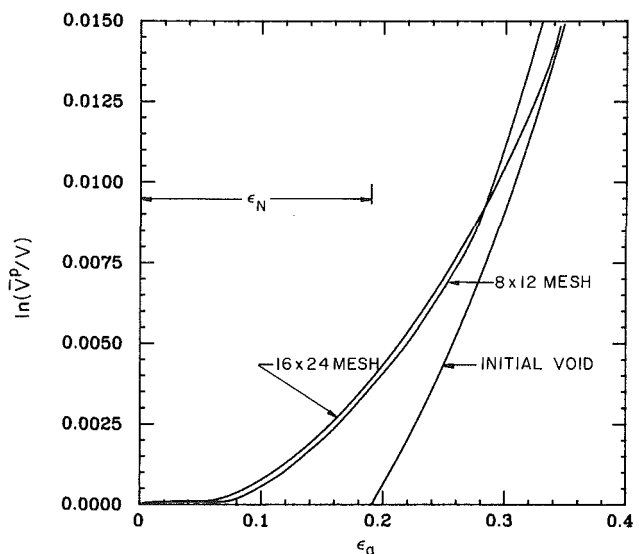


Fig. 6 Curves of normalized logarithmic plastic volume change, $\ln(\bar{V}^p/V)$, versus axial strain, ϵ_a , for a 1.04 percent volume fraction of inclusions with $\rho = 0.5$ in equation (3.7) and $\sigma_{\max} = 3\sigma_0$, $\alpha = 10.0$ and $\delta/r_0 = 0.04$. Numerical results are shown obtained from a coarse 8×12 mesh as well as results obtained using the 16×24 mesh shown in Fig. 3. The normalized logarithmic plastic volume change, $\ln(\bar{V}^p/V)$, versus axial strain, ϵ_a , curve for a 1.04 percent volume fraction of initial voids is shown shifted by an amount ϵ_N along the strain axis.

abruptly introduced into the material at ϵ_N . To define a nucleation strain in this context, the normalized logarithmic plastic volume change, $\ln(\bar{V}^p/V)$, is calculated via

$$\ln\left(\frac{\bar{V}^p}{V}\right) = \ln\left(\frac{b}{b_0}\right) + 2\ln\left(\frac{R}{R_0}\right) - \frac{1-2\nu}{E} \Sigma_h \quad (4.2)$$

The expression (4.2) is approximate because the effect of the inclusions is not accounted for in the elastic volume change term, but this is not of significance for the present purpose.

In Fig. 6, plastic volume change versus axial strain curves are plotted using two different finite element meshes; one is a coarse 8×12 mesh, while the other is the 16×24 mesh shown in Fig. 3 and used in all the remaining calculations reported on here. The results in Fig. 6 are for a rather "ductile" interface; $\delta/r_0 = 0.04$. Initial debonding takes place at $\epsilon_a = 0.068$ with the 16×24 mesh and at $\epsilon_a = 0.08$ with the coarse mesh. On the other hand, complete separation occurs somewhat earlier for the coarse mesh; at $\epsilon_a = 0.29$ as compared with $\epsilon_a = 0.34$ with the finer mesh. The more rapid separation with the coarse mesh is expected since the last points to debond are in the low strain region near the x^1 axis and the strain depression is resolved better in the fine mesh calculation. In the 16×24 mesh calculation complete debonding has occurred in all elements except the last one at $\epsilon_a = 0.31$. The strain interval over which debonding occurs depends on the value of δ/r_0 . With $\delta/r_0 = 0.01$, but all other parameters as in Fig. 6, initial debonding takes place at $\epsilon_a = 0.034$ and complete separation at $\epsilon_a = 0.18$.

A plastic volume change versus axial strain curve is also shown in Fig. 6 (using the 16×24 mesh) for an initial void of the same size as the inclusion. The curve of $\ln(\bar{V}^p/V)$ versus axial strain for the void is shifted an amount ϵ_N . The value of ϵ_N for which the $\ln(\bar{V}^p/V)$ versus ϵ_a curves nearly coincide at the larger volume changes shown (i.e., volume changes of the order of 1 percent) is taken as the nucleation strain. The fine mesh calculation gives a nucleation strain of 0.19, as shown, while the coarse mesh calculation implies $\epsilon_N = 0.17$.

This definition of nucleation strain is inherently imprecise. The sensitivity to the particular volume fraction at which the values of $\ln(\bar{V}^p/V)$ are matched depends on the "ductility" of

the interface, with more ductile interfaces being more sensitive to the value of $\ln(\bar{V}^p/V)$ chosen. In Fig. 6 where $\delta/r_0 = 0.04$, the above values of ϵ_N were based on matching the response at $\ln(\bar{V}^p/V) = 0.015$. Using $\ln(\bar{V}^p/V) = 0.01$ gives nucleation strains of 0.172 and 0.176 for the 8×12 and 16×24 meshes, respectively. With $\delta/r_0 = 0.01$, but all other parameters as in Fig. 6, defining ϵ_N based on $\ln(\bar{V}^p/V) = 0.015$, 0.01, and 0.005 leads to $\epsilon_N = 0.084$, 0.082, and 0.079.

Some calculations were carried out to explore the dependence of the nucleation strain, as defined above, on interface properties. A series of calculations were carried out using three values of δ/r_0 , i.e., for three sizes of inclusion. The model predicts a definite size effect and the results will be discussed in connection with void nucleation criteria in the context of Gurson's (1975, 1977) constitutive framework. There is a stronger dependence of nucleation strain on interfacial strength than on size. To illustrate this, two sets of interface parameters were chosen that have values of ϕ_{sep} in (2.8) 60 percent of that for the case with $\sigma_{max} = 3\sigma_0$ and $\delta/r_0 = 0.01$; in one case $\sigma_{max} = 3\sigma_0$ and $\delta/r_0 = 0.006$, while in the other case $\sigma_{max} = 1.8\sigma_0$ and $\delta/r_0 = 0.01$. These give rise to nucleation strains of 0.060 and 0.024, respectively, while in the reference case $\epsilon_N = 0.084$.

The role of the shear stiffness parameter, α , was investigated for the case $\rho = 0.4$, $\sigma_{max} = 3\sigma_0$, $\delta/r_0 = 0.02$. With $\alpha = 10.0$, the nucleation strain is 0.23. Increasing α to 50 increases the nucleation strain to 0.25, while with $\alpha = 1$, $\epsilon_N = 0.20$. In fact, taking $\alpha = 0$ in this case gives a nucleation strain of 0.18. Hence, for the geometry and loading conditions here, the interface shear stiffness plays a relatively minor role. This may not be the case for other inclusion geometries and for imposed stress states with a large shear component.

5 Void Nucleation Criterion

Within the constitutive framework for progressively cavitating solids introduced by Gurson (1975, 1977), the voids are represented in terms of a single parameter, the void volume fraction, f . The evolution equation for the void volume fraction includes contributions from both void growth and void nucleation,

$$\dot{f} = \dot{f}_{growth} + \dot{f}_{nucleation} \quad (5.1)$$

The void growth contribution is determined from the plastic flow rule using the condition that the matrix material is plastically incompressible whereas the void nucleation contribution is specified separately. Although various void nucleation criteria can be formulated within this framework, two have been used in practice (Gurson, 1975, 1977; Needleman and Rice, 1978). One is a plastic strain criterion for which

$$\dot{f}_{nucleation} = D\dot{\epsilon} \quad (5.2)$$

while the other is the stress-based criterion

$$\dot{f}_{nucleation} = B(\dot{\Sigma}_e + \dot{\Sigma}_h) \quad (5.3)$$

In equation (5.3), Σ_e is identified with the matrix effective stress appearing in the Gurson (1975, 1977) flow potential. As long as the void volume fraction is zero, as it is prior to nucleation, the matrix effective stress and the macroscopic effective stress are equal. In (5.2), D is considered a function of $\bar{\epsilon}$, while analogously in equation (5.3), B is taken to be a function of $(\Sigma_e + \Sigma_h)$ so that the quantity $(\Sigma_e + \Sigma_h)$ plays the role of a nucleation stress.

Analyses of localization, carried out within the Gurson (1975, 1977) framework, indicate that equations (5.2) and (5.3) can lead to quite different predictions of macroscopic ductility (Needleman and Rice, 1978; Saje et al. 1982). What is of particular significance in this regard is that the hydrostatic stress dependence of void nucleation in equation (5.3) leads to

Table 1 Nucleation strain and stress for various values of stress triaxiality. The interface is characterized by $\sigma_{max}/\sigma_0 = 3$, $\alpha = 10$ and $\delta/r_0 = 0.02$.

ρ	Σ_h/Σ_e	ϵ_N	$(\Sigma_e)_N/\sigma_0$	$(\Sigma_e + c\Sigma_h)_N/\sigma_0$
				$c = 0.35$
0.250	0.667	0.56	1.732	2.137
0.333	0.833	0.33	1.627	2.102
0.400	1.00	0.23	1.555	2.099
0.500	1.33	0.12	1.443	2.117
0.625	2.00	0.048	1.268	2.156
			Ave.	2.122

Table 2 Nucleation strain and stress for various values of stress triaxiality. The interface is characterized by $\sigma_{max}/\sigma_0 = 3$, $\alpha = 10$ and $\delta/r_0 = 0.01$.

ρ	Σ_h/Σ_e	ϵ_N	$(\Sigma_e)_N/\sigma_0$	$(\Sigma_e + c\Sigma_h)_N/\sigma_0$
				$c = 0.35$ $c = 0.39$
0.250	0.667	0.50	1.723	2.125 2.171
0.333	0.833	0.27	1.594	2.058 2.111
0.400	1.00	0.17	1.509	2.038 2.098
0.500	1.33	0.084	1.388	2.036 2.110
0.625	2.00	0.024	1.192	2.027 2.122
			Ave.	2.057 2.122

Table 3 Nucleation strain and stress for various values of stress triaxiality. The interface is characterized by $\sigma_{max}/\sigma_0 = 3$, $\alpha = 10$ and $\delta/r_0 = 0.04$.

ρ	Σ_h/Σ_e	ϵ_N	$(\Sigma_e)_N/\sigma_0$	$(\Sigma_e + c\Sigma_h)_N/\sigma_0$
				$c = 0.35$ $c = 0.314$
0.250	0.667	0.61	1.752	2.161 2.119
0.333	0.833	0.40	1.664	2.149 2.099
0.400	1.00	0.31	1.605	2.167 2.109
0.500	1.33	0.19	1.501	2.201 2.129
0.625	2.00	0.070	1.322	2.248 2.152
			Ave.	2.185 2.122

a strong nonnormality in the plastic flow rule which promotes early flow localization.

In order to explore the predicted hydrostatic stress dependence of the void nucleation strain, ϵ_N , calculations were carried out for various values of the stress ratio ρ in equation (3.7). In each case ϵ_N is defined in the manner sketched in Fig. 6. Tables 1 to 3 illustrate the hydrostatic stress dependence of ϵ_N for interfaces characterized by three values of δ/r_0 . The other interface parameters are kept fixed at $\sigma_{max} = 3\sigma_0$ and $\alpha = 10$.

For low stress triaxiality, $\Sigma_h/\Sigma_e = 0.667$, the nucleation strain varies between 0.50 and 0.61 as δ/r_0 is increased by a factor of four, from 0.01 to 0.04. At higher values of the stress triaxiality, the absolute magnitude of the variation in ϵ_N is smaller, but the relative variation is greater; for example, when $\Sigma_h/\Sigma_e = 2.00$, the nucleation strain increases from 0.024 to 0.070 as δ/r_0 is varied over the same range. With δ regarded as fixed, this corresponds to a decrease in nucleation strain with increasing particle size at fixed volume fraction.

Also shown in Tables 1 to 3 is the outcome of correlating the results in terms of an effective nucleation stress, written as

$$\Sigma_N = \Sigma_e + c\Sigma_h \quad (5.4)$$

where Σ_e and Σ_h are obtained from equation (4.1) at $\epsilon_a = \epsilon_N$.

For the case $\delta/r_0 = 0.02$, $c = 0.35$ leads to a mean nucleation stress, Σ_N , of 2.122 σ_0 . If equation (5.4) held precisely, the value of Σ_N would be independent of ρ in Table 1. The maximum deviation from the mean is 1.5 percent and this occurs for the lowest nucleation strain where the work hardening

is highest; more significant is the deviation from the mean for $\Sigma_h/\Sigma_e = 0.667$ since this occurs at large strains where the work hardening rate is low.

Tables 2 and 3 show the results of calculating nucleation stresses for $\delta/r_0 = 0.01$ and $\delta/r_0 = 0.04$ in two ways; one calculation uses a constant c , while in the other calculation c is chosen so that the average value of Σ_N is the same for all three cases. A somewhat better correlation is obtained by varying c suggesting that more "brittle" interfaces (larger particles) may be characterized by a more strongly hydrostatic stress dependent nucleation stress.

With $c = 1$ in equation (5.4), the nucleation stress appearing in equation (5.3) is recovered, and with $c = 1$ and $\Sigma_h/\Sigma_e = 0.667$ a nucleation stress of 2.887 is obtained; at $\Sigma_h/\Sigma_e = 1.00$, $\Sigma_N (c = 1) = 3.109$ and at $\Sigma_h/\Sigma_e = 2.00$, $\Sigma_N (c = 1) = 3.806$. Although it is interesting to note that these values, particularly for the cases with lower stress triaxiality, are reasonably close to σ_{max} , use of $c = 1$ in equation (5.4) gives rise to a strongly hydrostatic stress dependent nucleation stress. Values of c less than unity in equation (5.4) can be thought of as due to part of the remote hydrostatic stress being "converted" to local shearing stresses around the inclusion, the magnitude of which are limited by the work hardening capacity of the material.

6 Concluding Remarks

The cohesive zone interface model developed here provides a unified description of void initiation from initial debonding through complete separation and subsequent void growth. This cohesive zone model is particularly attractive when, as is often the case, interfacial strengths are relatively weak, say of the order of several times the yield strength of the matrix material. Then the very high stress gradients associated with cracks in homogeneous bodies do not develop and standard finite-strain finite-element methods can be extended to incorporate the interface integrals. The model is a purely continuum one, so that discrete dislocation effects are not accounted for, but the formulation provides a framework for analyzing the effects of matrix and inclusion material properties, inclusion size and shape, and imposed stress state and loading rate on the nucleation process.

Dimensional considerations introduce a characteristic interface length into the model and numerical results exhibit a ductile to brittle transition in the mode of separation. For sufficiently large inclusions (relative to the characteristic length) equilibrium solutions do not exist for increasing extension during debonding. The interface debonds in a "brittle" manner, with an abrupt stress drop. One can speculate that if this were to occur at a particular weak inclusion, the stress drop could lead to load shedding to nearby inclusions. The increased stress could then precipitate further nucleation, leading to another stress redistribution and so on, so that a profusion of voids are nucleated over a rather narrow strain interval. In actuality, in such a case, debonding would occur dynamically and dynamic effects may well play a significant role in the mechanics of the stress redistribution. By way of contrast, the smooth load drop associated with a more "ductile" interface (smaller inclusions) suppresses this mechanism of void profusion. In this regard it is important to note that the range of strain over which voids nucleate can affect stability against flow localization; void profusion over a narrow range of strain is potentially destabilizing (Needleman and Rice, 1978; Saje et al., 1980).

The onset of nucleation at various levels of triaxiality of the imposed stress state has been correlated, within the framework of Gurson's (1975, 1977) constitutive relation for progressively cavitating solids, in terms of a critical nucleation stress. This critical nucleation stress depends linearly on the hydrostatic tension, but with a coefficient that is less than unity.

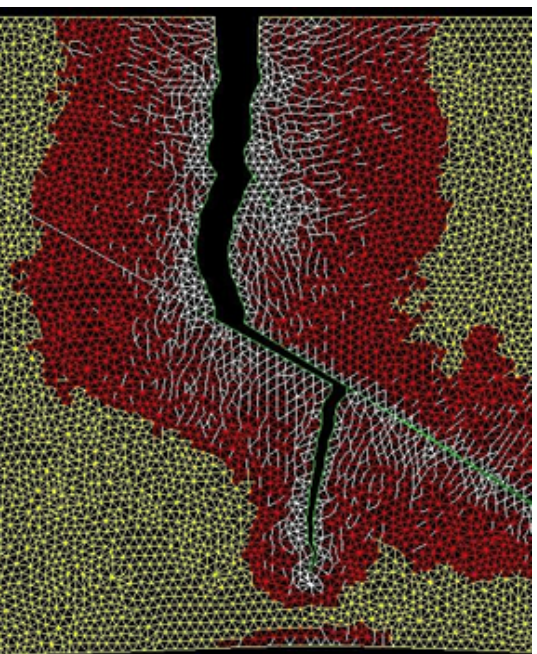
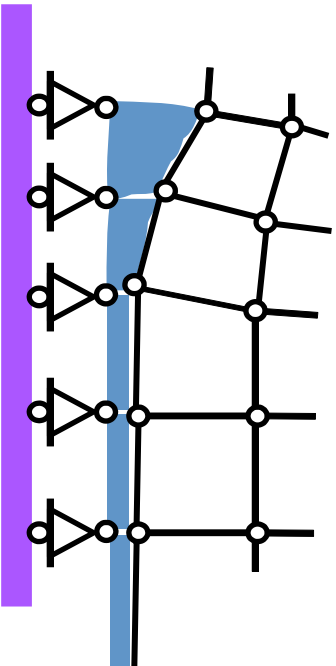
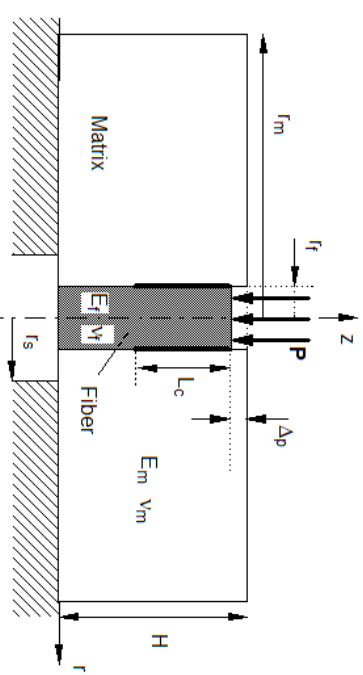
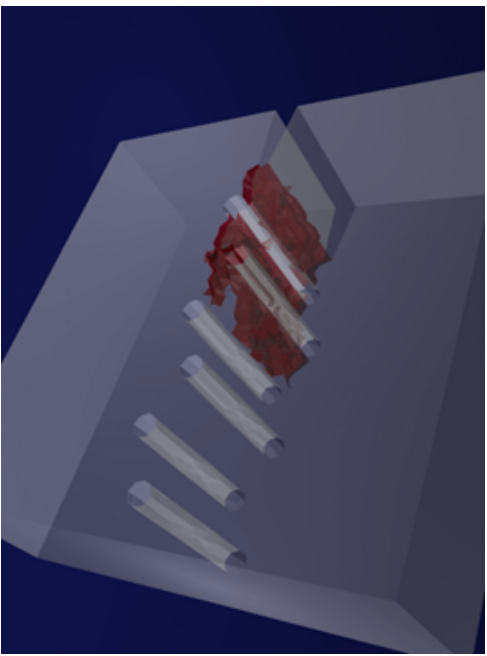
Acknowledgments

The support of the National Science Foundation (Solid Mechanics Program) through grant MSM-8419338 is gratefully acknowledged. The computations reported on here were carried out at the John von Neumann Center for Scientific Computing and at the Pittsburgh Supercomputer Center. Access to these facilities was made possible through a National Science Foundation program to provide supercomputer access to researchers.

References

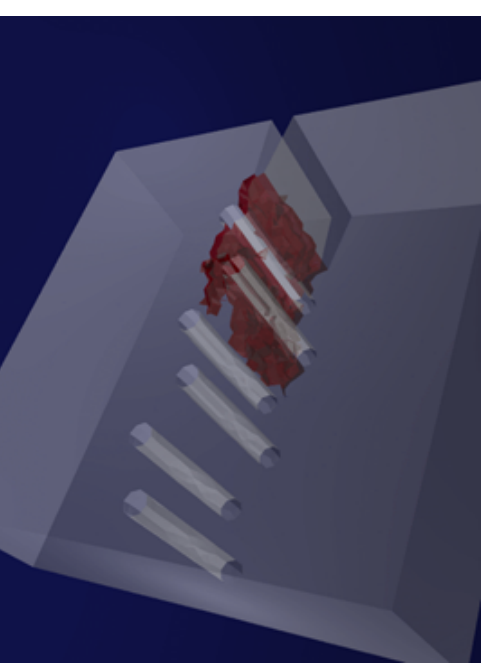
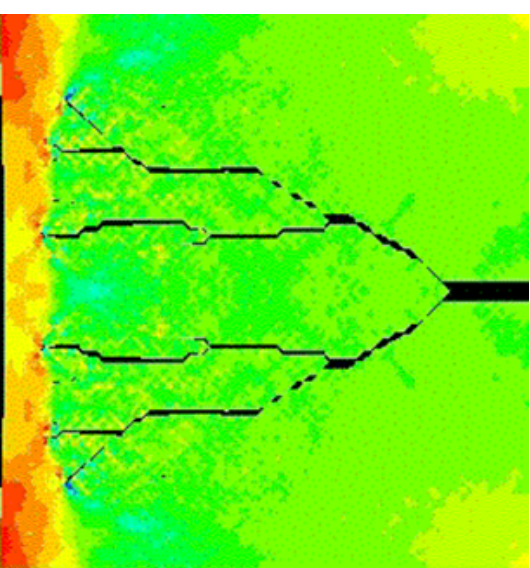
- Argon, A. S., Im, J., and Safoglu, R., 1975, "Cavity Formation from Inclusions in Ductile Fracture," *Met. Trans.*, Vol. 6A, pp. 825-837.
- Barenblatt, G. I., 1962, "Mathematical Theory of Equilibrium Cracks," *Adv. Appl. Mech.*, Vol. 7, pp. 56-129.
- Brown, L. M., and Stobbs, W. M., 1971, "The Work-Hardening of Copper-Silica II. The Role of Plastic Relaxation," *Phil. Mag.*, Vol. 23, pp. 1201-1233.
- Brownrigg, A., Spitzig, W. A., Richmond, O., Tierlinck, D., and Embury, J. D., 1983, "The Influence of Hydrostatic Pressure on the Flow Stress and Ductility of a Spheroidized 1045 Steel," *Acta Metall.*, Vol. 31, pp. 1141-1150.
- Chang, Y. W., and Asaro, R. J., 1978, "Bauschinger Effects and Work Hardening in Spheroidized Steels," *Metal Science*, Vol. 12, pp. 277-284.
- Cialone, H., and Asaro, R. J., 1978, "The Role of Hydrogen in the Ductile Fracture of Plain Carbon Steels," *Met. Trans.*, Vol. 10A, pp. 367-375.
- Dugdale, D. S., 1960, "Yielding of Steel Sheets Containing Slits," *J. Mech. Phys. Solids*, Vol. 8, pp. 100-104.
- Fisher, J. R., and Gurland, J., 1981, "Void Nucleation in Spheroidized Carbon Steels; Part 2: Model," *Metal Science*, Vol. 15, pp. 193-202.
- Goods, S. H., and Brown, L. M., 1979, "The Nucleation of Cavities by Plastic Deformation," *Acta Metall.*, Vol. 27, pp. 1-15.
- Gurson, A. L., 1975, "Plastic Flow and Fracture Behavior of Ductile Materials Incorporating Void Nucleation, Growth and Interaction," Ph.D. Thesis, Brown University.
- Gurson, A. L., 1977, "Continuum Theory of Ductile Rupture by Void Nucleation and Growth; Part I: Yield Criterion and Flow Rules for Porous Ductile Materials," *J. Engr. Mat. Tech.*, Vol. 99, pp. 2-15.
- Keer, L. M., Dundurs, J., and Kiattikomol, K., 1973, "Separation of a Smooth Circular Inclusion from a Matrix," *International Journal of Engineering Science*, Vol. 11, pp. 1221-1233.
- Needleman, A., 1972, "A Numerical Study of Necking in Circular Cylindrical Bars," *J. Mech. Phys. Solids*, Vol. 20, pp. 111-120.
- Needleman, A., 1982, "Finite Elements for Finite Strain Plasticity Problems," *Plasticity of Metals at Finite Strain: Theory, Computation and Experiment*, E. H. Lee and R. L. Mallett, eds., pp. 387-436.
- Needleman, A., and Rice, J. R., 1978, "Limits to Ductility Set by Plastic Flow Localization," *Mechanics of Sheet Metal Forming*, Koistinen, D. P., and Wang, N.-M., eds., pp. 237-265.
- Needleman, A., and Rice, J. R., 1980, "Plastic Creep Flow Effects in the Diffusive Cavitation of Grain Boundaries," *Acta Metall.*, Vol. 28, pp. 1313-1332.
- Pearce, D., Shih, C. F., and Needleman, A., 1984, "A Tangent Modulus Method for Rate Dependent Solids," *Comp. Struct.*, Vol. 18, pp. 875-887.
- Saje, M., Pan, J., and Needleman, A., 1982, "Void Nucleation Effects on Shear Localization in Porous Plastic Solids," *Int. J. Fract.*, Vol. 19, pp. 163-182.
- Taya, M., and Patterson, W. G., 1982, "Growth of a Debonded Void at a Rigid Secondary Particle in a Viscous Metal," *J. Matl. Sci.*, Vol. 17, pp. 115-120.
- Tvergaard, V., 1976, "Effect of Thickness Inhomogeneities in Internally Pressurized Elastic-Plastic Spherical Shells," *J. Mech. Phys. Solids*, Vol. 24, pp. 291-304.
- Tvergaard, V., 1982, "On Localization in Ductile Materials Containing Spherical Voids," *Int. J. Fract.*, Vol. 18, pp. 237-252.

CVFE: cohesive/volumetric finite elements Warp3D Implementation - Dadds



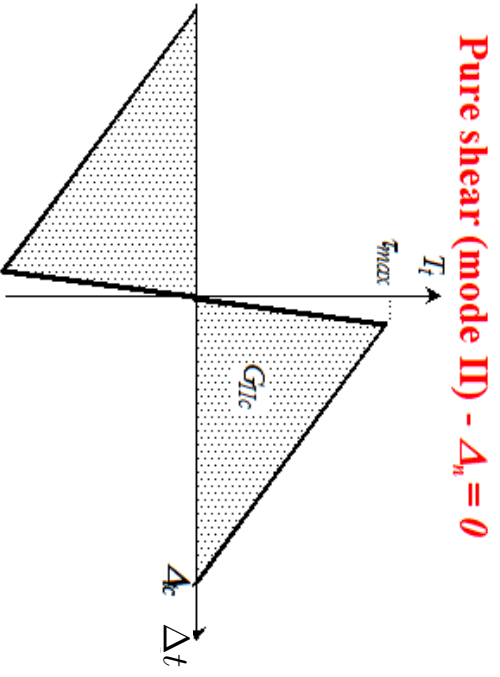
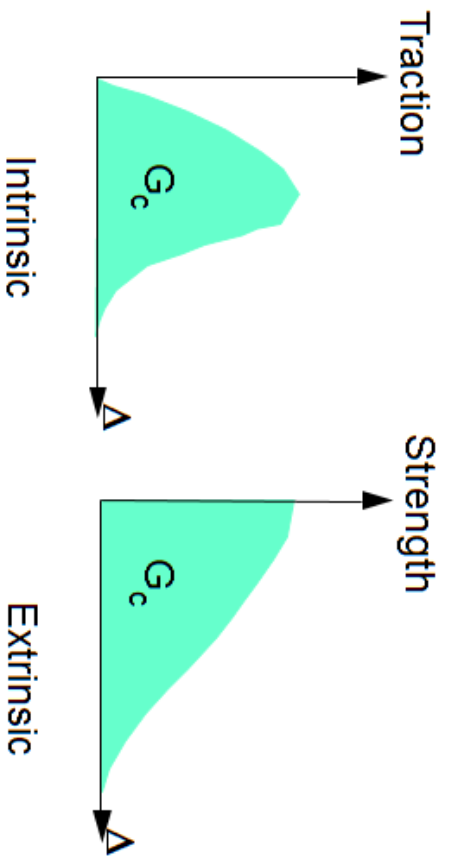
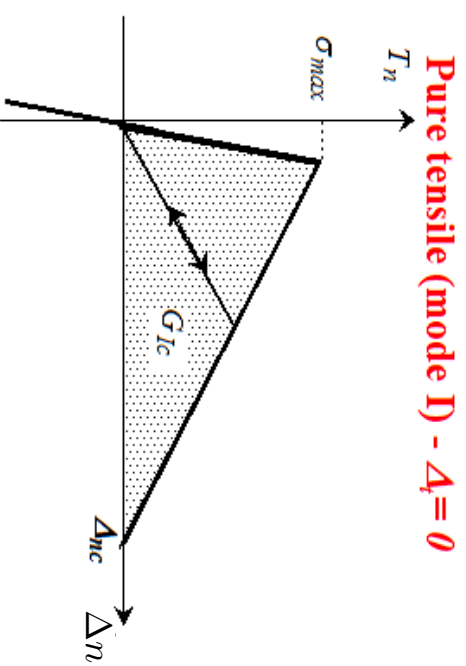
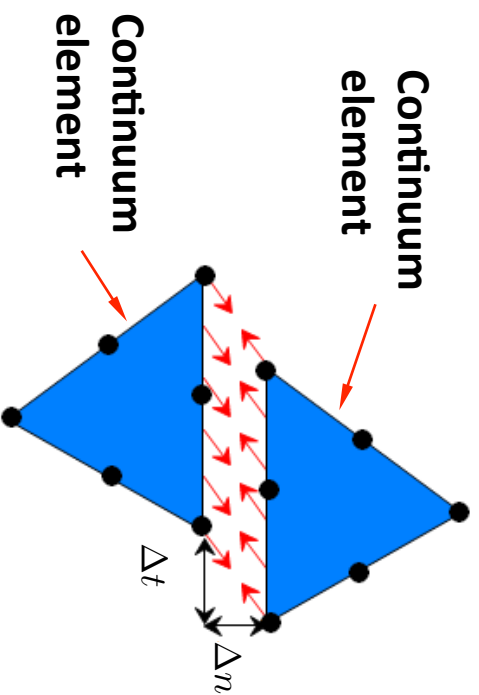
Overview

- CVFE is a numerical scheme for crack formation & propagation
- Retains flexibility of conventional finite element methods in geometry, loading and material properties
- Enables spontaneous initiation, propagation and arrest of cracks
- Brittle and ductile materials
- Metals, ceramics, concrete, wood, composites, nano, etc.
- Wide applications but also has many issues



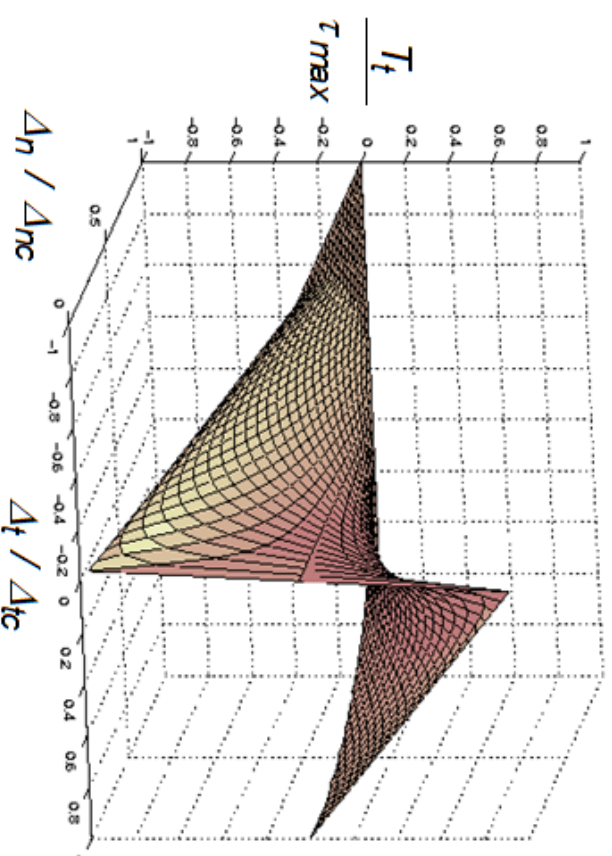
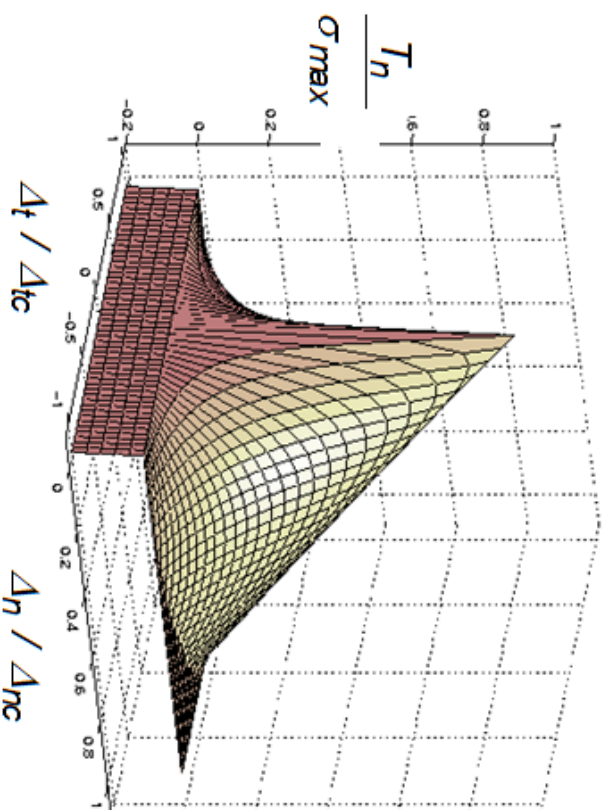
Key ideas

Traction-displacement rather than stress-strain



Constitutive models

Normal cohesive traction



Shear cohesive traction

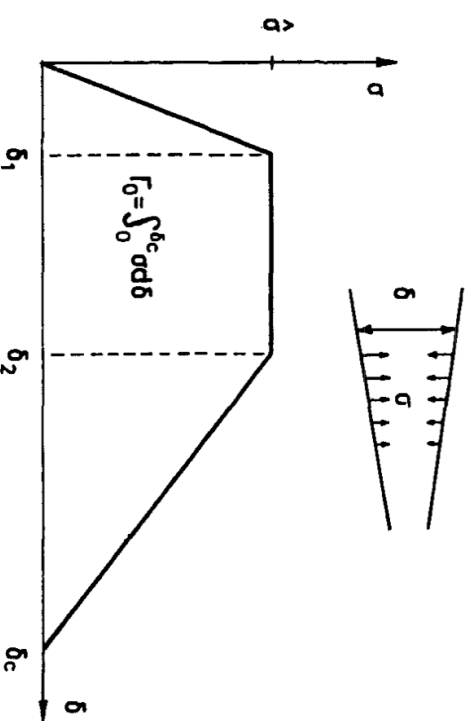
Newest coupled models formulated on better mechanics theories (less ad hoc)

K Park, G Paulino, J Roesler, A unified potential-based cohesive model of mixed-mode fracture,
Journal of the Mechanics and Physics of Solids, Vol 57, 2009, pg 891-908

Effects modeled

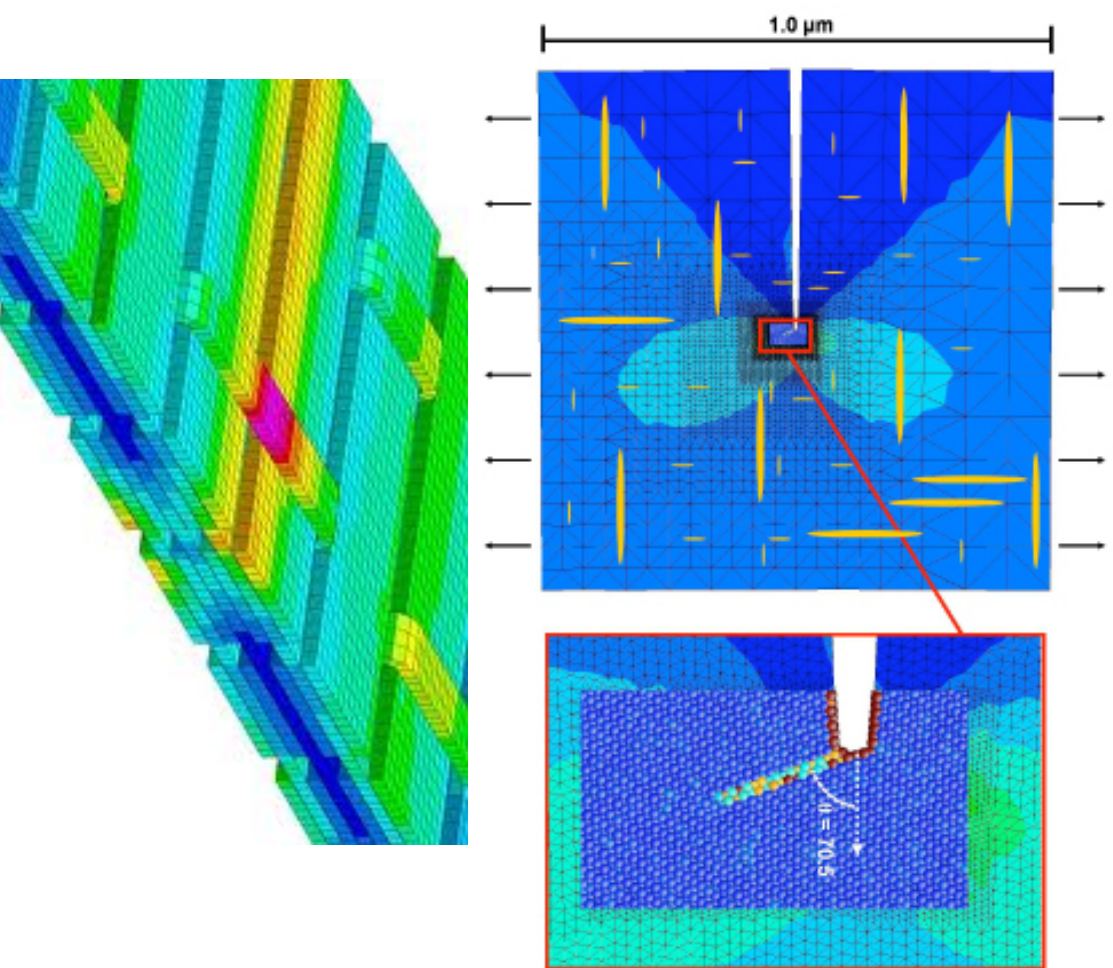
The traction-displacement concept of CZMs extended to include:

- Strain rate effects
- Temperature effects
- Viscoelastic effects
- Fatigue damage
- Hydrogen degradation
- Spatial gradation of material properties
- Various forms of post-peak behavior
- Much work ongoing today...

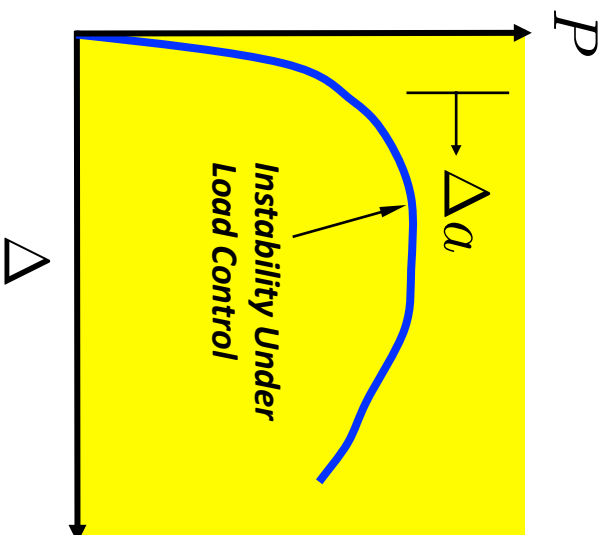
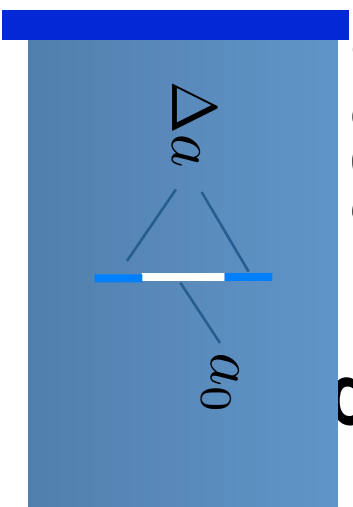


Some applications

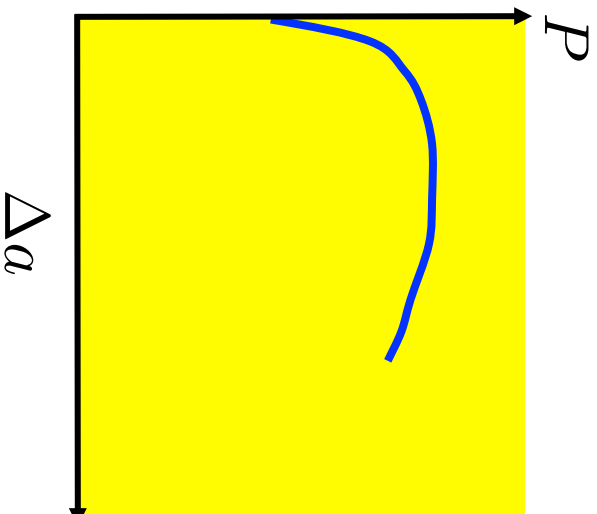
- Crack propagation in structural metals
- Debonding of particles in metals, around rebars in concrete, around aggregate in concrete
- Quasi-static and dynamic fiber pushout in model composites
- Fragmentation during ballistic impact
- Accident scenarios in solid propellant rockets
- Fatigue failure of (self-healing) polymers
- 3-D and adaptive dynamic fracture simulations
- μm scale simulations of material failure
- ... many, many more ...



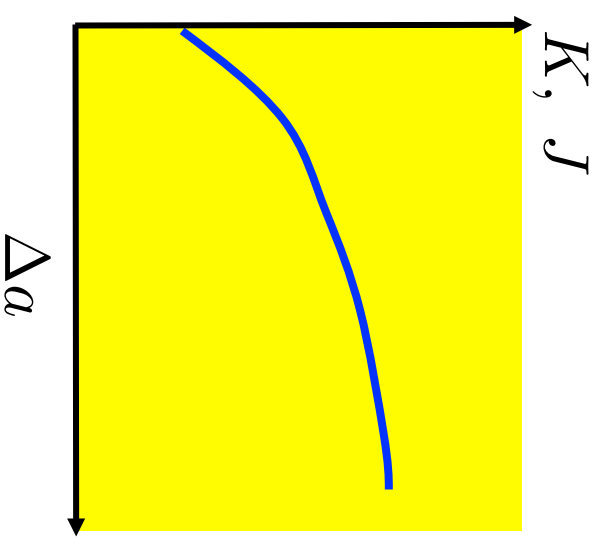
Application: tearing in Al panels



Net section loss overcomes strain hardening of background material



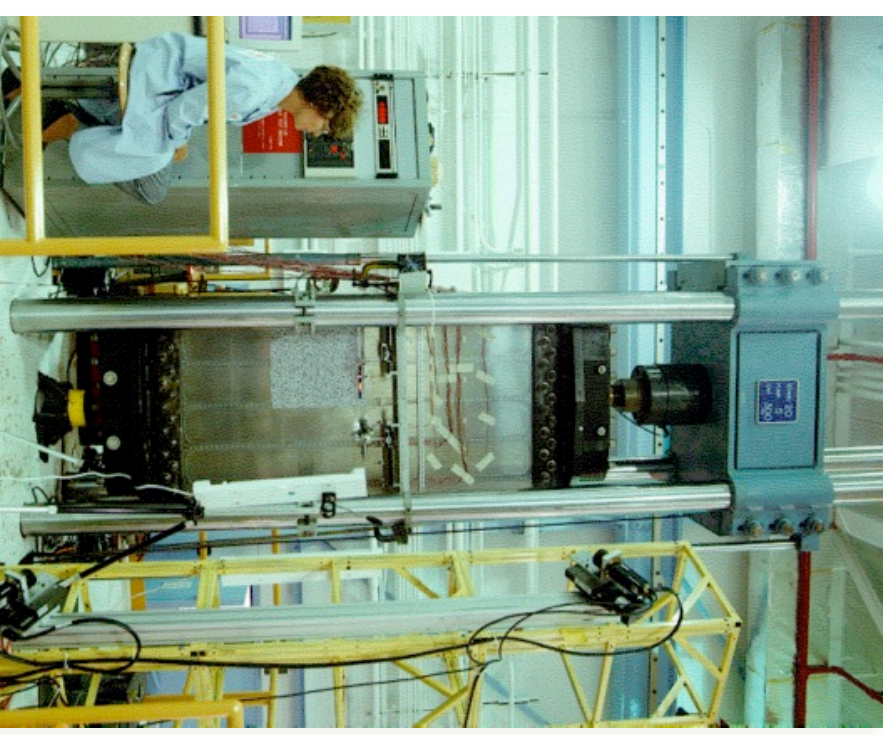
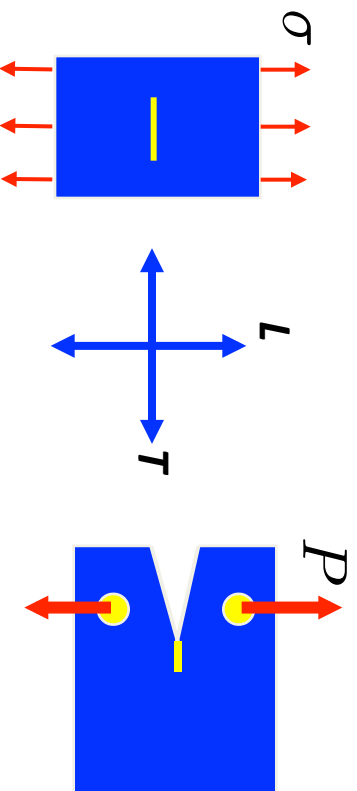
Remote plasticity increases monotonically: pre-damages material



NASA tests: aging aircraft pgm

NASA-Langley (Dawicke / Newman)

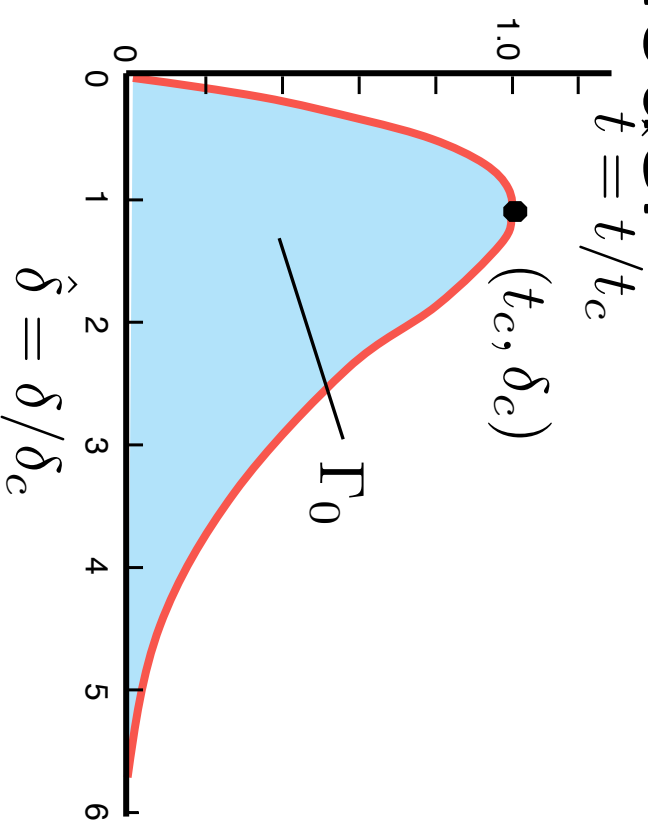
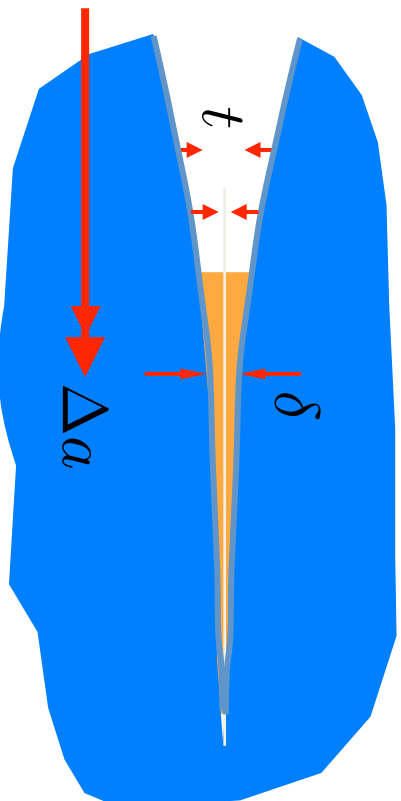
- Material -- Al 2024-T3 (L-T)
- Thickness -- 2.3 mm
- Yield Stress -- 345 MPa
- Specimens -- C(T) and M(T)
- Size -- 50 mm to 1000 mm
- a/W ratios -- 0.33 to 0.5
- Flat-to-slant fracture transition
- Out-of-plane bending: constrained or unconstrained



[1] Newman JC, Dawicke DS, Seshadri BR. Residual strength analyses of stiffened and un-stiffened panels – Part I. Laboratory specimens. Engng Fract Mech 2003;70:493–507.

[2] Seshadri BR, Newman JC, Dawicke DS. Residual strength analyses of stiffened and unstiffened panels – Part II. Wide panels. Engng Fract Mech 2003;70:509–24.

Mode I cohesive model



- ◆ Curve shape fixed (exponential decay)
- ◆ δ_c , t_c , Γ_0 (2 of 3 are independent)
- ◆ Curve shape not overly critical for ductile metals
- ◆ Post-peak curve is key factor for brittle materials

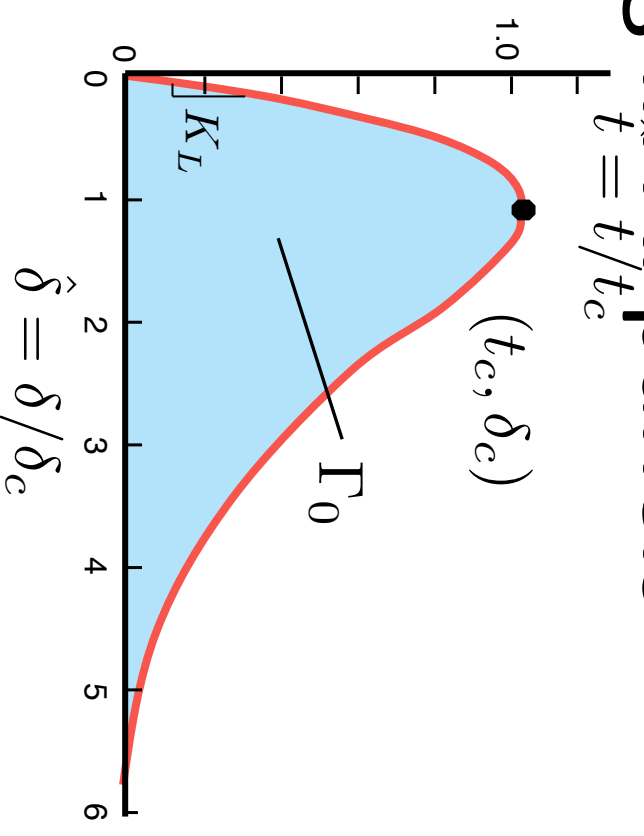
Application: tearing in Al panels

Traction-separation for the simple exponential model

$$t(\delta) = \exp(1) t_c \frac{\delta}{\delta_c} \exp\left(-\frac{\delta}{\delta_c}\right)$$

$$\Gamma_0 = \int_0^{\infty} t d\delta = \exp(1) t_c / \delta_c$$

$$K_L = \frac{\partial t}{\partial \delta} (\delta = 0) = \exp(1) t_c / \delta_c$$



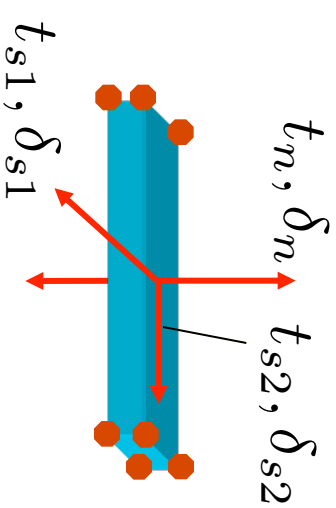
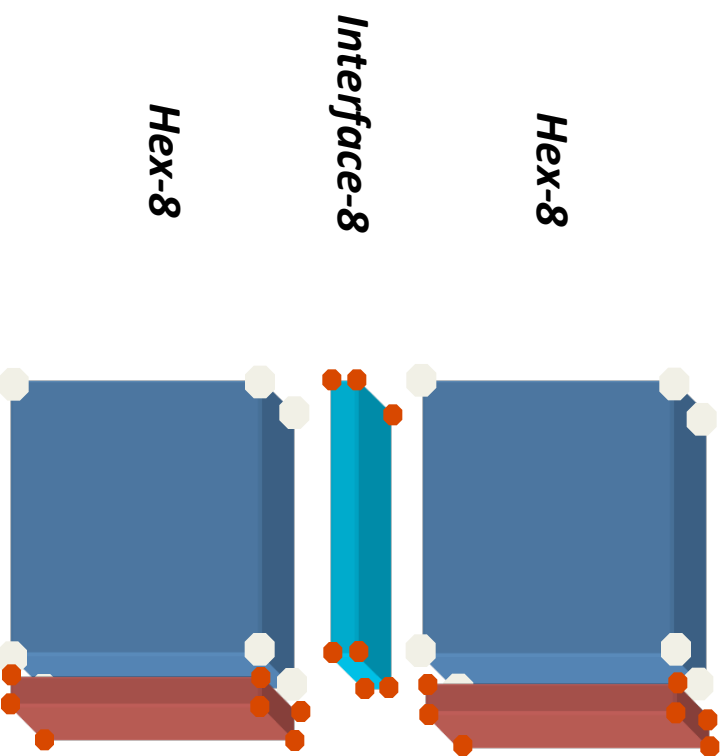
$$\delta = \sqrt{\beta^2 (\delta_{s1}^2 + \delta_{s2}^2) + \delta_n^2}$$

$$t = \sqrt{\beta^{-2} (t_{s1}^2 + t_{s2}^2) + t_n^2}$$

Mode I : $\beta = 0$; $t = t_n$; $\delta = \delta_n$

Roychowdhury, S.; Roy, Y. D. A. & Dodds, R. H. Ductile tearing in thin aluminum panels: Experiments and analyses using large-displacement, 3-D surface cohesive elements. *Eng. Frac. Mech.*, 2002, 69, pp. 983-1002.

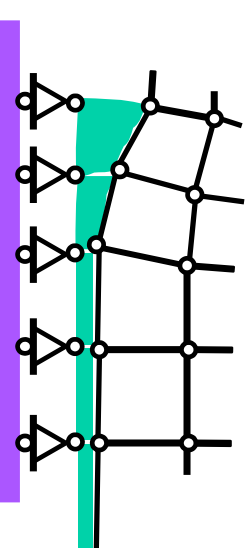
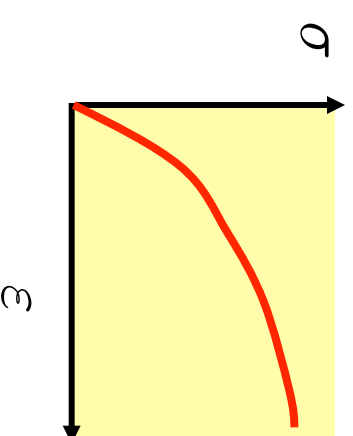
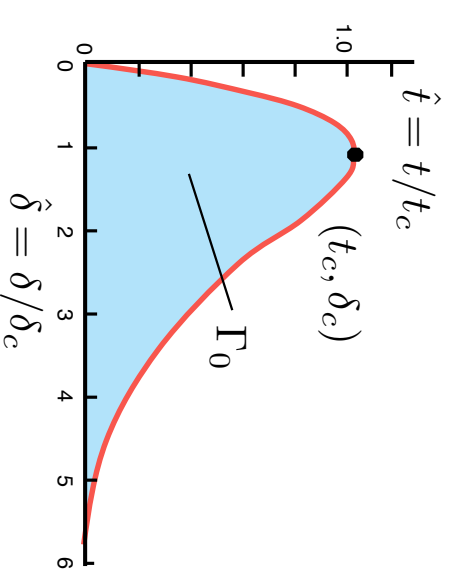
3D model definition



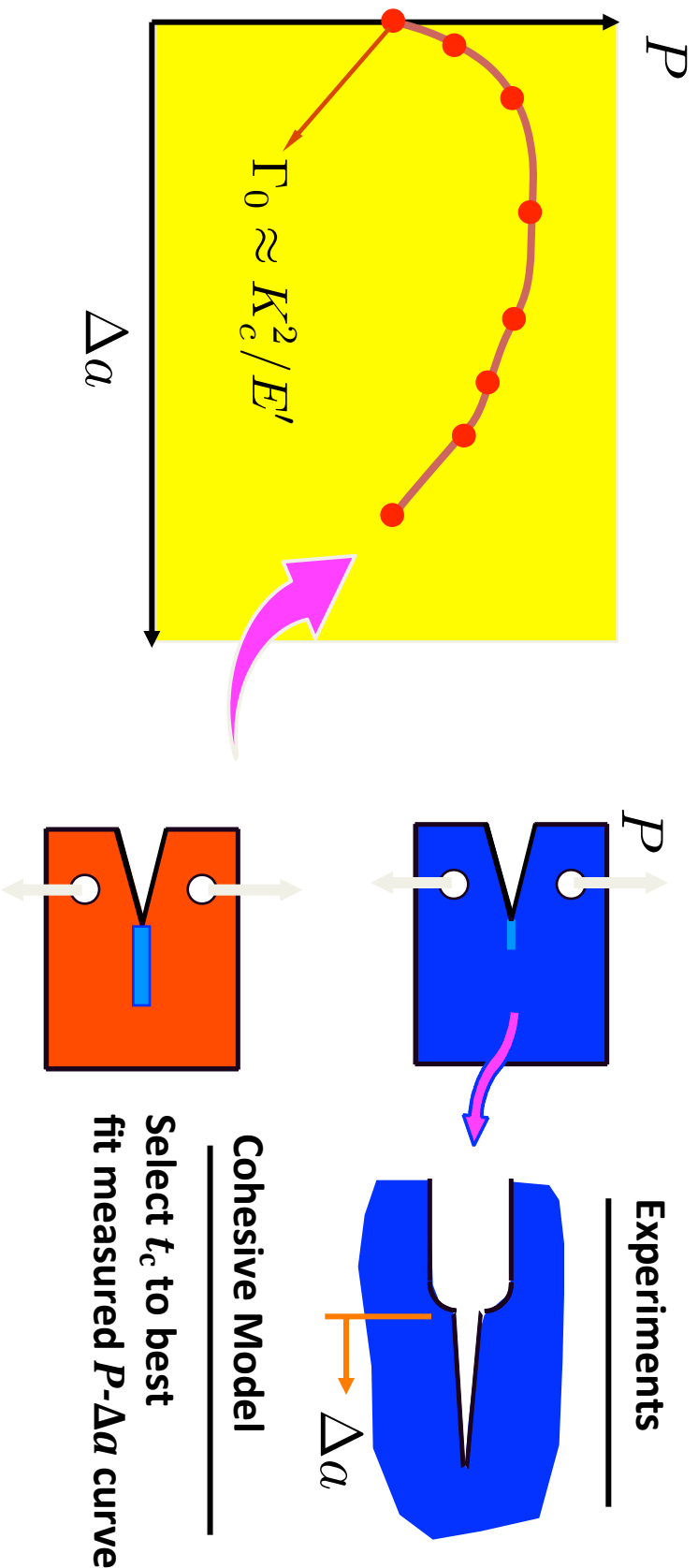
- 8-node interface element
- Mixed modes (normal, shear)
- Zero initial thickness
- Isoparametric formulation
- Large-displacements in interface elements
- Finite strains in solid elements

Tearing model calibration

- **Cohesive constitutive parameters**
 - t_c, Γ_0, δ_c
 - β not involved for Mode I ($=0$)
 - δ_c fixed by curve shape
 - Provides material length-scale thru Γ_0
- **Background material**
 - True stress-true strain curve
- **Mesh refinement**
 - Sufficient to resolve fields in background material
 - Interface element sizes do not provide length-scale (advantage compared to computational cells)
 - Typically interface $l_e < 50\delta_c$



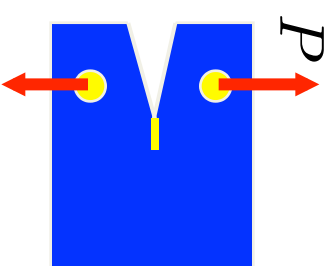
C(T) tests for calibration



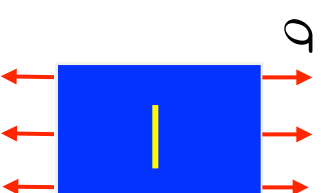
Γ_0 from measured K_c (SSY @ First Δa for this Al)
 t_c fitted to measured (surface) crack growth data
=> Calibration pair (Γ_0 , t_c) is not unique

Calibration and application

- CZM calibration using 150 mm C(T) tested specimens
 - No out-of-plane (buckling) displacements
 - Positive T -stress (high in-plane constraint)
 - Flat mode of fracture enforced in analysis
- Prediction of σ - Δa in unconstrained M(T) tests
 - 4 layers of 8 node elements on crack plane over B , 20 node bricks elsewhere for bending: 30-65 K nodes
 - Ability to predict the measured out-of-plane displacements
 - Negative T -stress (low in-plane constraint)
- WARP3D research code (Illinois)

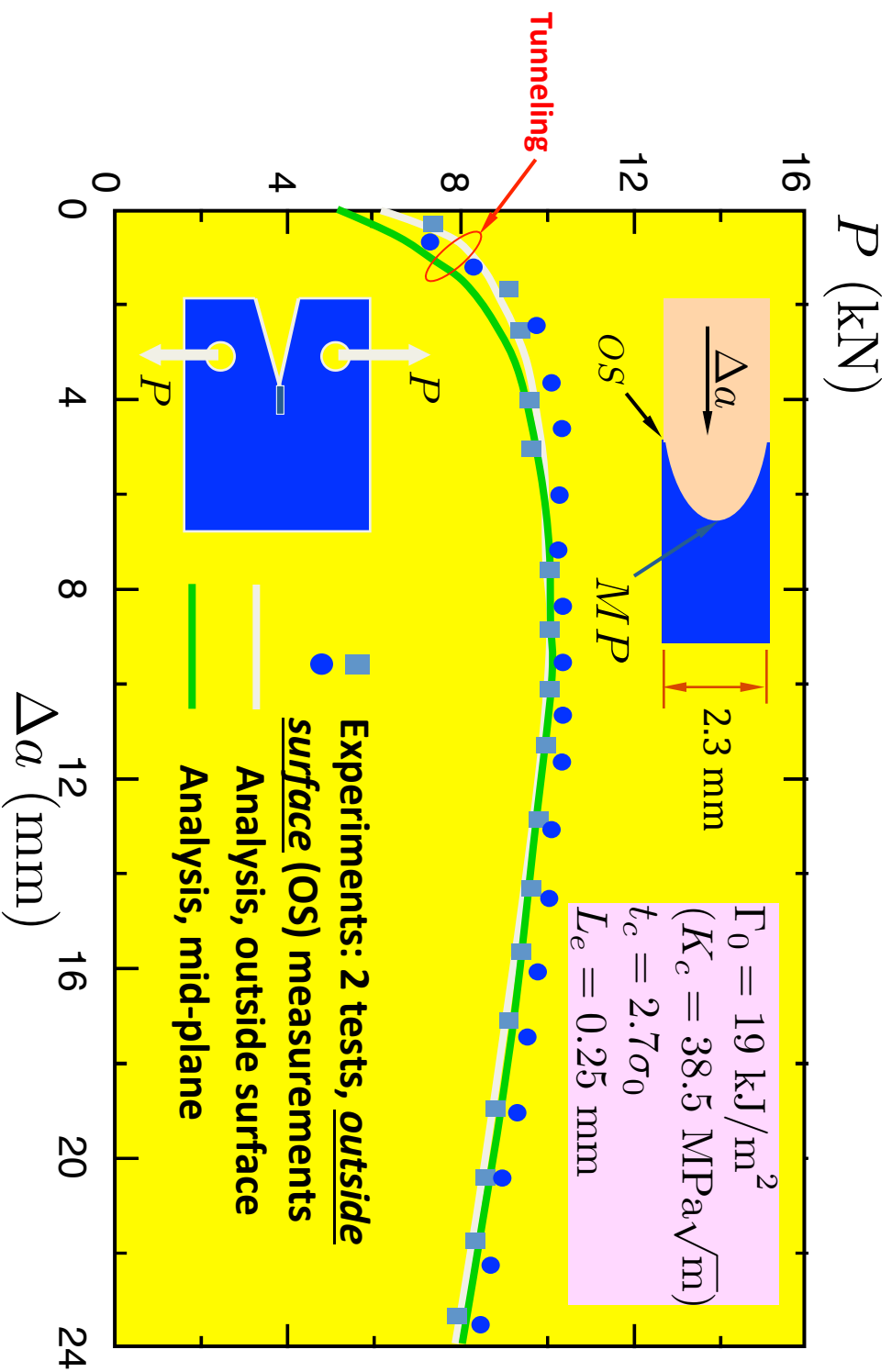


Compact Tension: C(T)



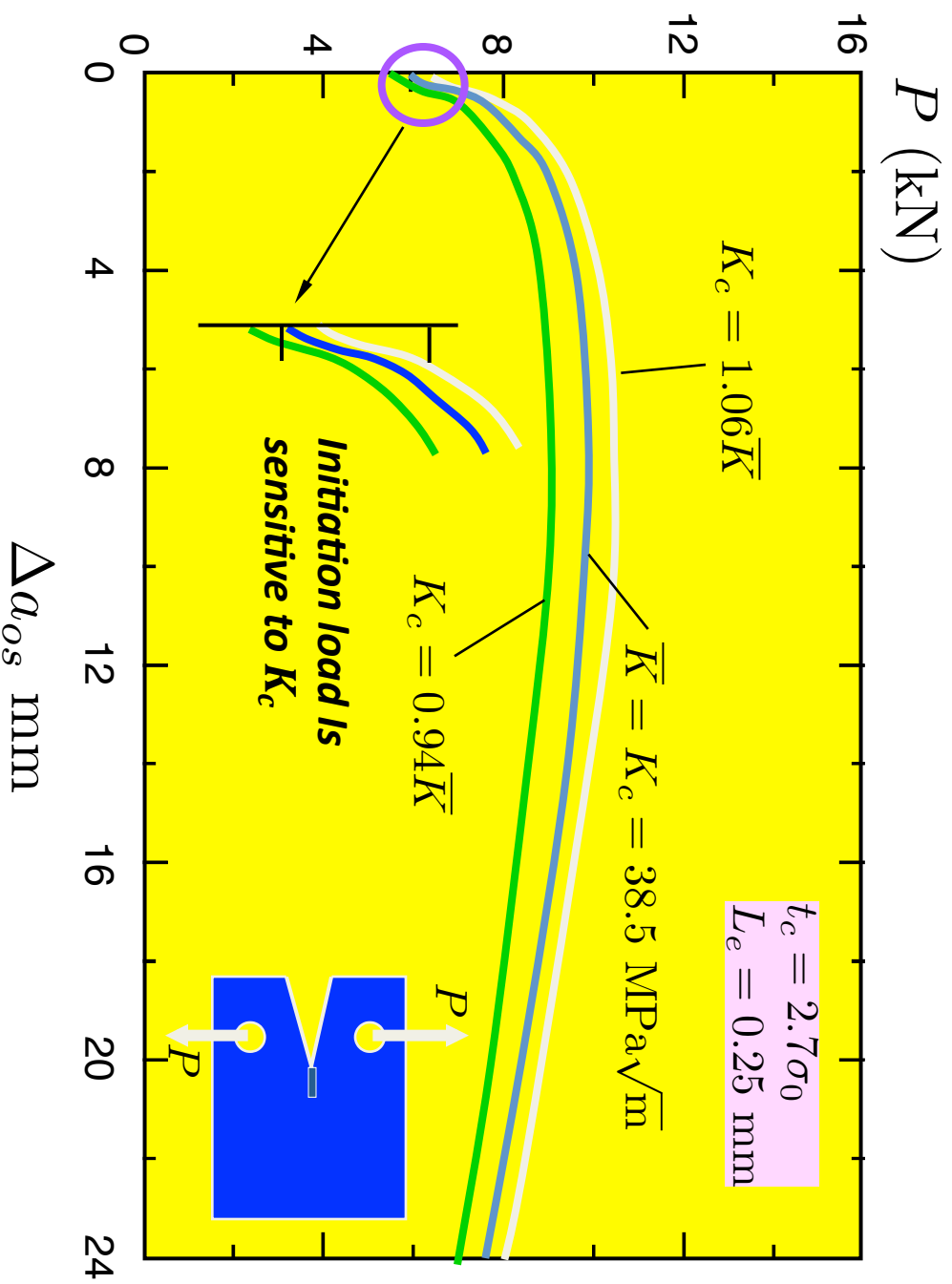
Middle Crack Tension: M(T)

C(T) calibration: $W = 150 \text{ mm}$, $a/W = 0.4$

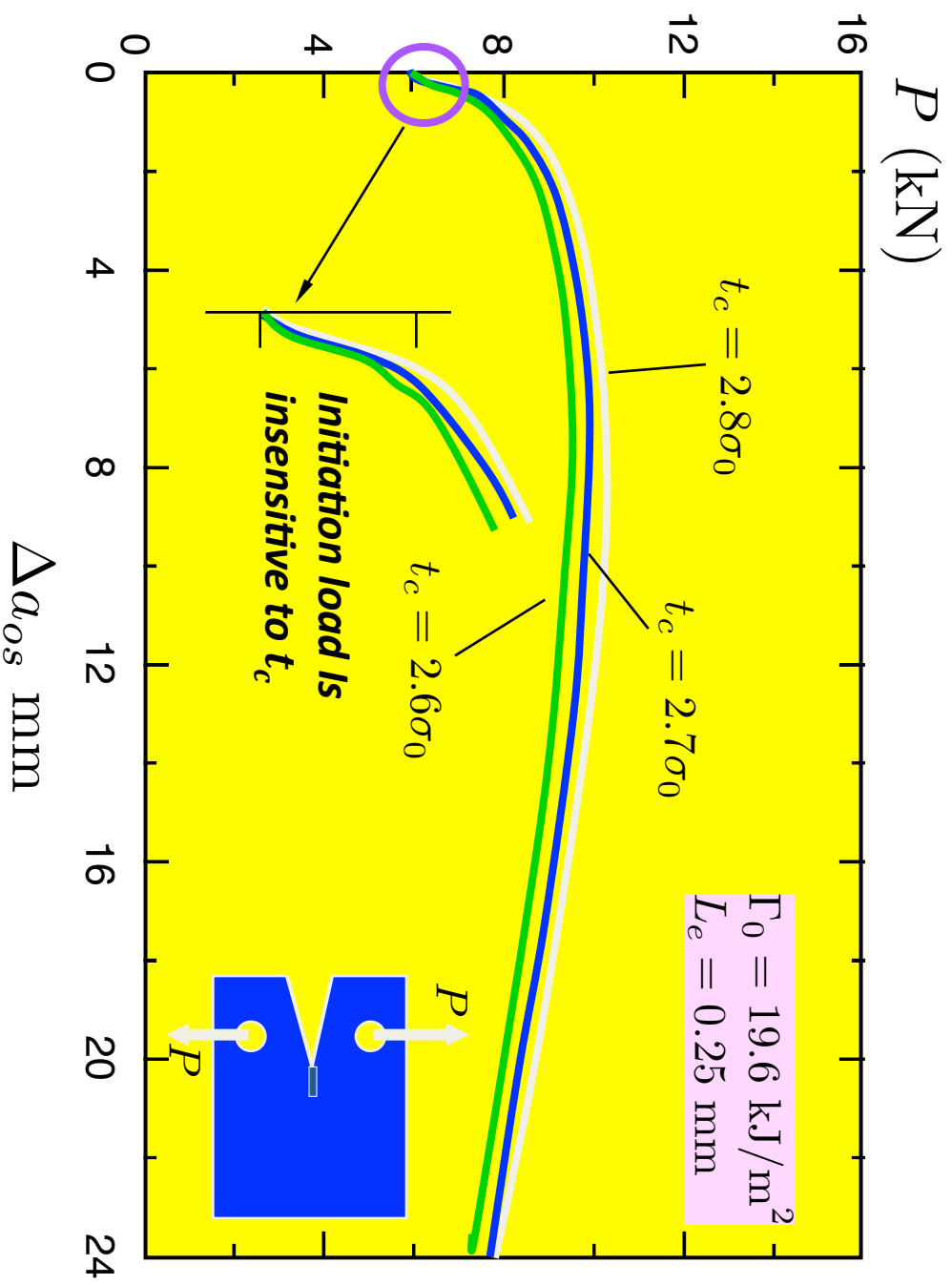


****Specimen w/ Most Crack Tip Triaxiality****

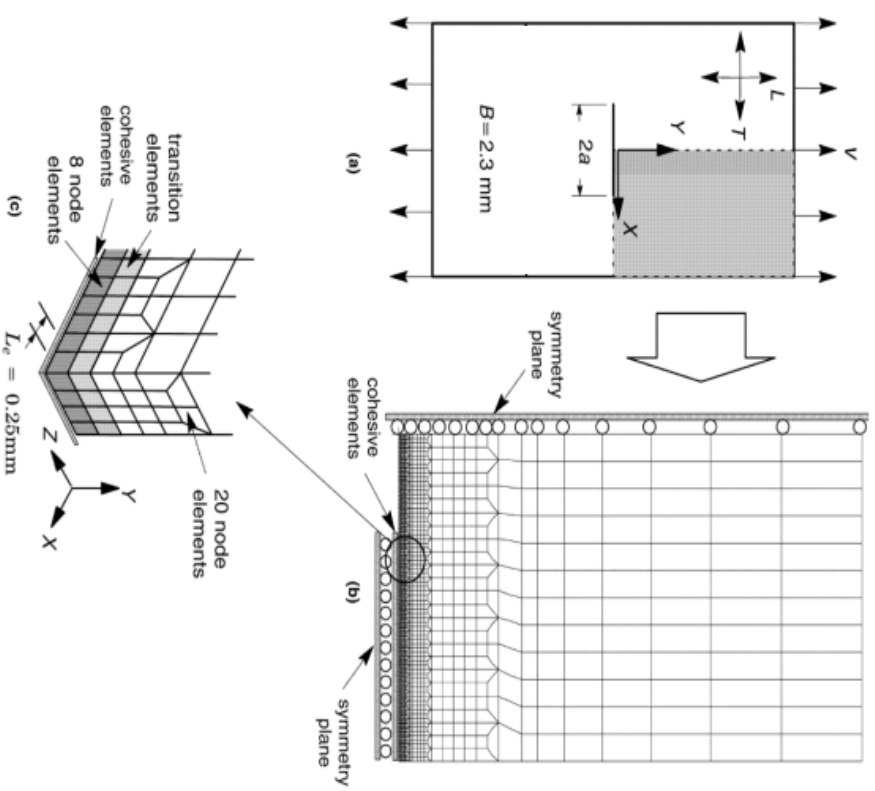
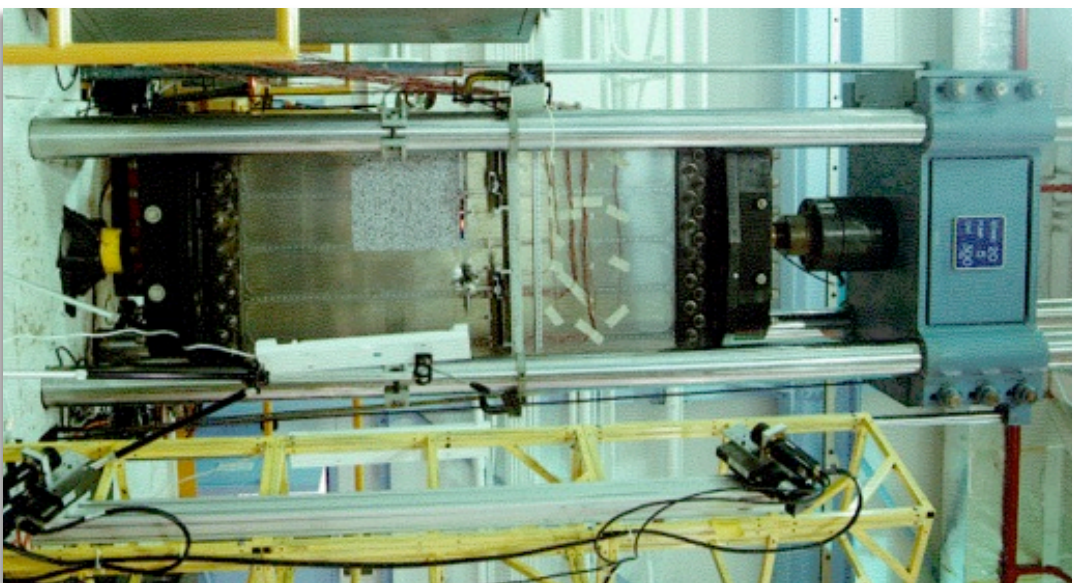
Calibration: sensitivity to Γ_0 (i.e. K_c)



Calibration: sensitivity to t_c



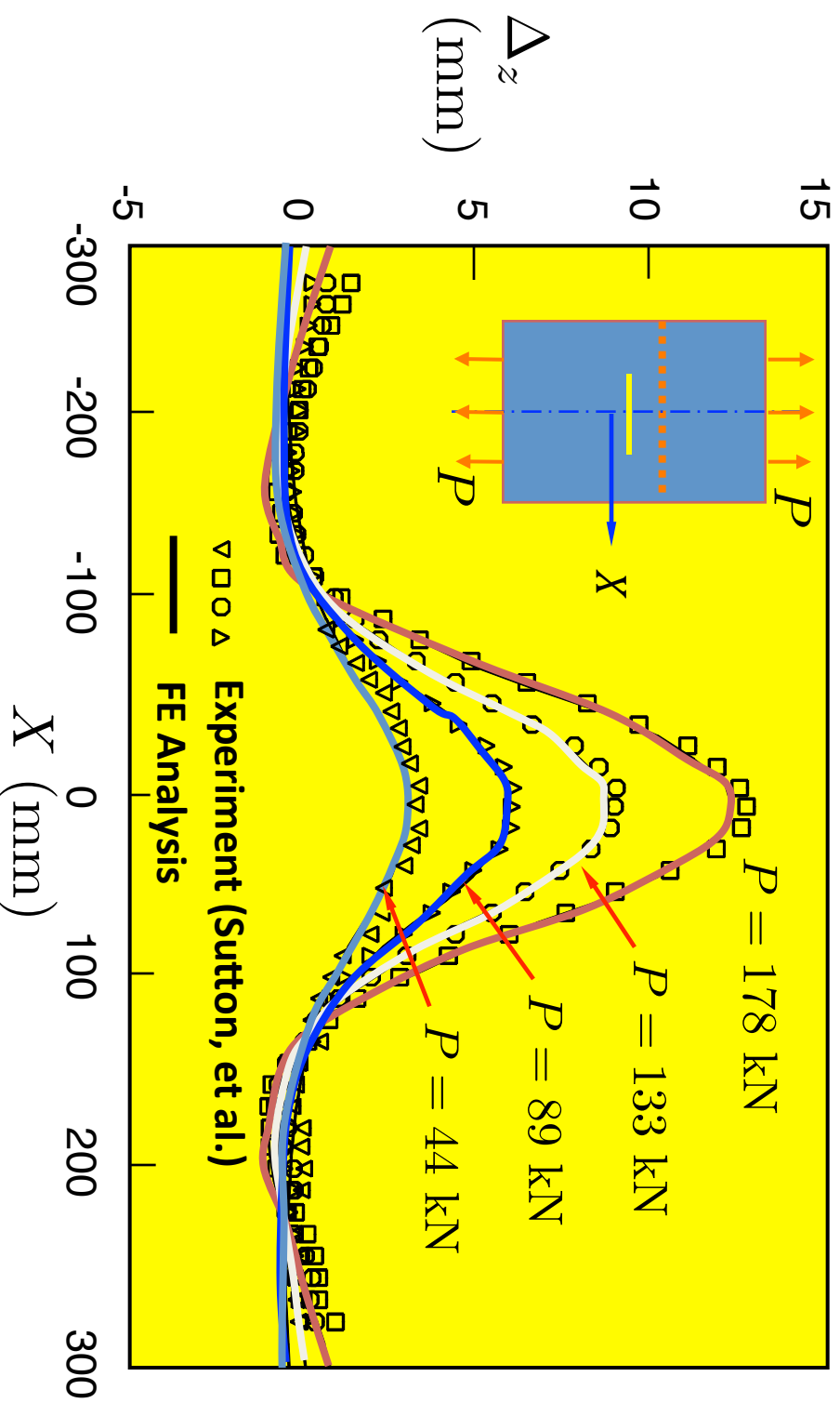
FE model for M(T) specimens



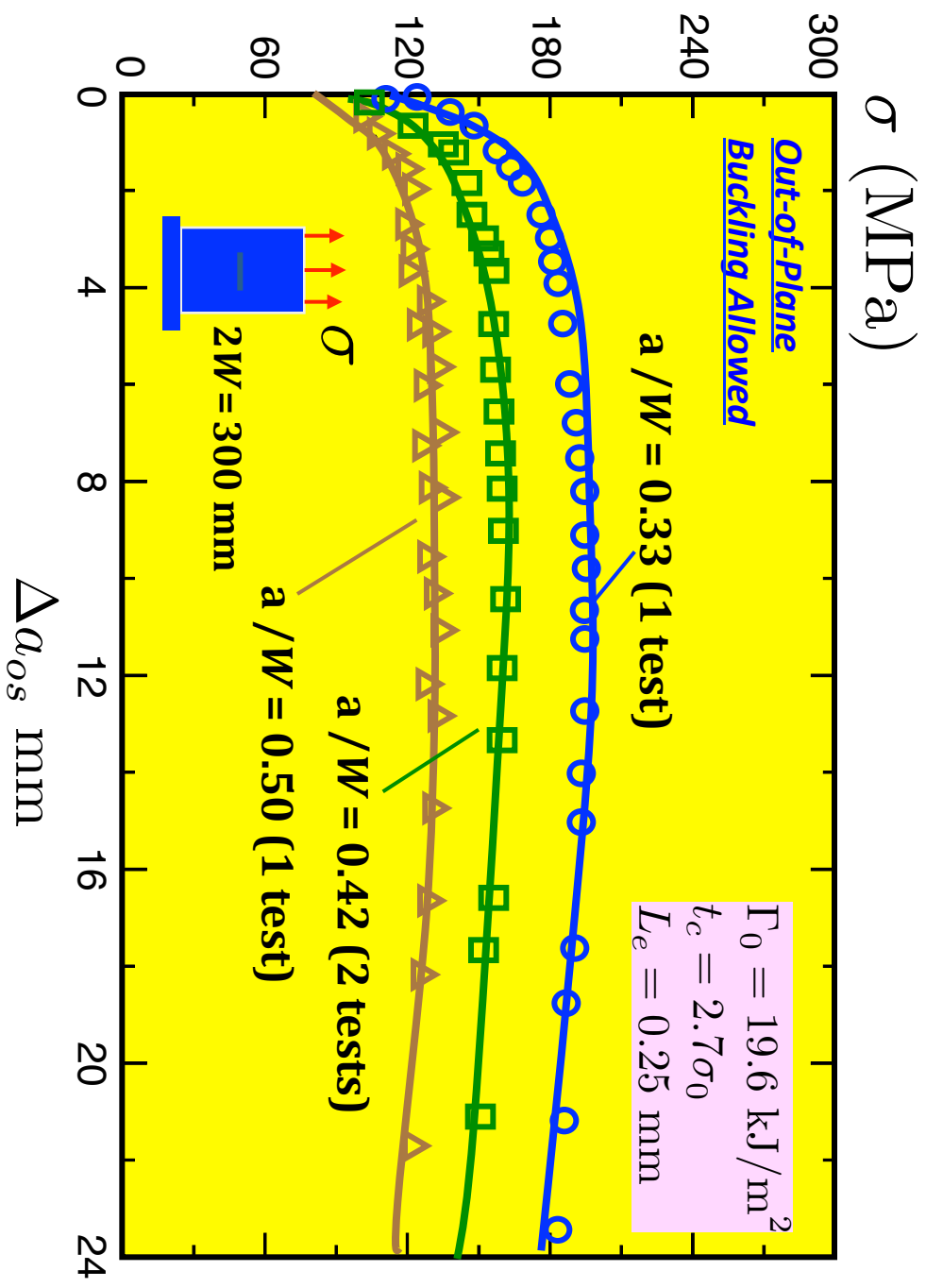
Out-of-plane displacements

$M(T)$, $W = 600$ mm, $a/W = 0.33$
(Tearing suppressed by hole drilling)

No buckling preventers used in test.
Out-of-plane displacements driven by
negative T -stress.



Tearing in $W=300$ mm M(T)s

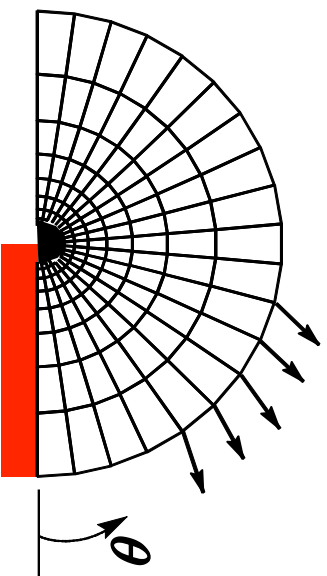


Negative T -stress elevates crack initiation load
 30-40% above LEFM predictions: CZM captures the effect

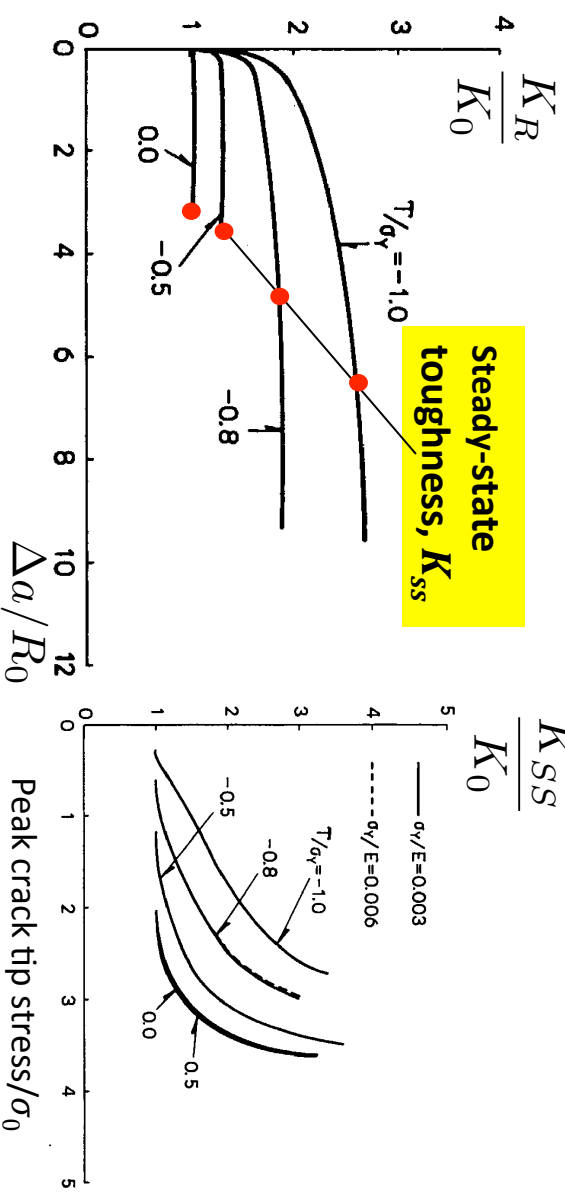
Ductile growth in SSY

- SSY conditions provide a very clear picture of constraint effects on ductile tearing (J - Δa) curves
- T -stress provides 1st order model for specimen geometries and loading types (tension vs. bending)

$R \gg r_p$ K_I, T varies



Cohesive zone model solutions for ductile stress levels and cohesive strengths. Tvergaard & Hutchinson, JMPS, 1994

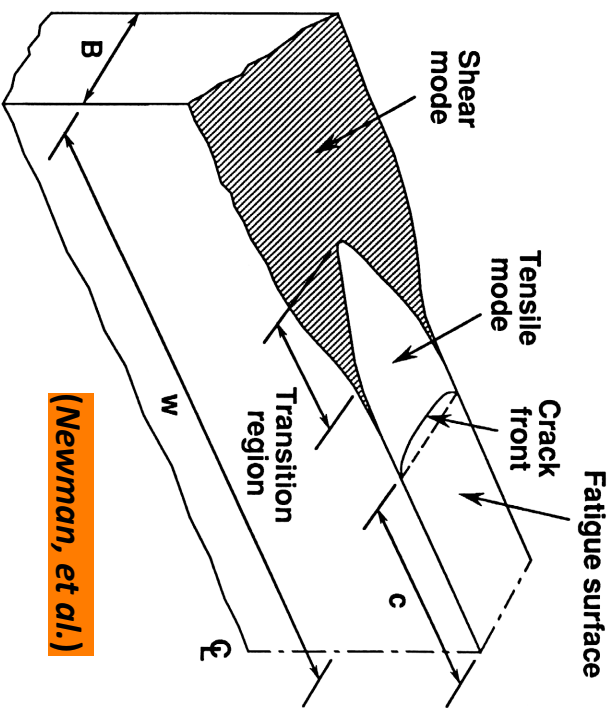


K_0 = cohesive toughness = $\sqrt{E'\Gamma_0}$
 R_0 = plastic zone size at K_0

CZM comments

- 3-D solid model with interface elements & cohesive constitutive law predicts very well:
 - In-plane constraint (T -stress) effects
 - Out-of-plane (buckling) displacements
 - Load vs. crack extension relationships
 - Early flat tearing mode & tunneling
- Challenges:
 - Modeling slant vs. flat vs “V” fracture modes & the transitions between modes
 - Crack turning caused by anisotropic toughness coupled with T -stress effects
 - Thickness dependence of cohesive parameters: CZM parameters should vary with triaxiality in background material (include Rice-Tracey type void effects)
 - Transferability of calibrated model to wider range of conditions is not yet established
 - Artificial anisotropy when CZM elements are inserted over large regions of mesh
 - Complexity of mesh generation with CZM elements
 - Many more CZMs are not a panacea!

Slant fracture, crack turning



**Flat to slant crack
mode transition**



**Crack turning & flat to slant crack mode
transition**

Constitutive Law for Hydrogen Induced Plasticity (Sofronis + Dodds + WARP 3D).

Deformation Rate tensor, D_{ij} (for small deformations)

$$\dot{\epsilon}_{ij} = \dot{\epsilon}_{ij}^e + \dot{\epsilon}_{ij}^h + \dot{\epsilon}_{ij}^p$$

$$\dot{\epsilon}_{ij}^e = \frac{1}{2G} \dot{S}_{ij} + \frac{1}{9K} \dot{\sigma}_{kk} \delta_{ij}$$

where $S_{ij} = \sigma_{ij} - \frac{1}{3} \delta_{ij} \sigma_{kk}$.

$$\dot{\epsilon}_{ij}^h = \dot{\epsilon}^h \delta_{ij}$$

$$\epsilon^h = \ln \left[1 + \frac{\lambda (c - c_0)}{3} \right]$$

- represents time differentiation

$$\lambda = \Delta V / \Omega$$

ΔV = volume change per atom of hydrogen introduced into solution

Ω = mean atomic volume of the host metal atom.

Then,

$$\dot{\epsilon}_{ij}^h = \frac{1}{3} \Lambda(c) \dot{c} \delta_{ij}$$

where $\Lambda(c) = \lambda / [1 + \lambda(c - c_0)/3]$

for small concentrations

$$\Lambda(c) \approx \lambda$$

Then, we have

$$\dot{\epsilon}_{ij}^h = \dot{c} (AV/3\Omega) \delta_{ij}$$

Rate independent material,

c_0 = reference state initial
solute concentration

$$f = \sigma_e - \sigma_y(\epsilon^p, c) = 0$$

(Eqn 23
Sofronis)

$$\sigma_e = \left(\frac{3}{2} s_{ij} s_{ij} \right)^{1/2}$$

$$\epsilon^P = \int \sqrt{\frac{2}{3} \dot{\epsilon}_{ij}^P \dot{\epsilon}_{ij}^P}$$

$$\sigma_y = \sigma_0^H \left(1 + \frac{\epsilon^P}{\epsilon_0} \right)^{1/n}$$

σ_0^H = initial yield stress
in presence of hydrogen
concentration this value
decreases.

ϵ^P = strain in uniaxial tension

ϵ_0 = initial yield strain

$$\sigma_0^H = \phi(c) \sigma_0$$

$$\phi(c) = (\xi - 1)c + 1$$

$$\text{If } c=1 \quad \phi = \xi; \quad \sigma_0^H = \xi \sigma_0$$

denotes the ratio of yield stress in
the presence of hydrogen, σ_0^H ,

that in the absence of hydrogen
 σ_0 . Max. hydrogen concentration
is 1.

c = hydrogen concentration in both
NILS and trapping sites.

Plastic part of strain,

$$\dot{\epsilon}_{ij}^P = \dot{\epsilon}^P \frac{3}{2} \frac{s_{ij}}{\bar{\sigma}}$$

Consistency condition,

$$\dot{f} = \frac{\partial f}{\partial \sigma_{ij}} \dot{\sigma}_{ij} + \frac{\partial f}{\partial \dot{\epsilon}^P} \dot{\epsilon}^P + \frac{\partial f}{\partial c} \dot{c} = 0$$

We note that c is a function of σ_{kk} and ϵ^P .

$$c = \beta \left[\theta_L(\sigma_{kk}) + \theta_{TL}(\sigma_{kk}, \epsilon^P) \right]$$

Then,

$$\dot{\epsilon}_{ij}^P = \frac{\left[\frac{3 s_{ij}}{2 \bar{\sigma}} - \frac{\partial \sigma_y}{\partial c} \frac{\partial c}{\partial \sigma_{pp}} \delta_{kl} \delta_{mn} \right] \frac{3 s_{ij} \dot{\sigma}_k}{2 \bar{\sigma}}}{\left(\frac{\partial \sigma_y}{\partial \dot{\epsilon}^P} + \frac{\partial \sigma_y}{\partial c} \frac{\partial c}{\partial \dot{\epsilon}^P} \right)}$$

(Eqn 27 Sigfronius provides the full description of strain rate - stress relationship)

Hydrogen induced shear localization of the plastic flow in metals and alloys

P. Sofronis^{a,*}, Y. Liang^a, N. Aravas^b

^a *University of Illinois at Urbana-Champaign, Department of Theoretical and Applied Mechanics,
104 South Wright Street, Urbana, IL 61801, USA*

^b *University of Thessaly, Department of Mechanical and Industrial Engineering, Pedion Areos, 38334 Volos, Greece*

(Received 19 March 2001; revised and accepted 3 September 2001)

Abstract – Hydrogen enhanced localized plasticity (HELP) is a viable mechanism for hydrogen embrittlement supported by experimental observations. According to the HELP mechanism, hydrogen induced premature failures result from hydrogen induced plastic instability which leads to hydrogen assisted localized ductile processes. The objective of this work is to reveal the role of hydrogen in possibly localizing the macroscopic deformation into bands of intense shear using solid mechanics methodology. The hydrogen effect on material deformation is modeled through the hydrogen induced volume dilatation and the reduction in the local flow stress upon hydrogen dissolution into the lattice. Hydrogen is assumed to reside in both normal interstitial lattice sites (NILS) and reversible traps associated with the plastic deformation. The analysis of the plastic deformation and the conditions for plastic flow localization are carried out in plane strain uniaxial tension. For a given initial hydrogen concentration in the unstressed specimen, a critical macroscopic strain is identified at which shear localization commences. © 2001 Éditions scientifiques et médicales Elsevier SAS

hydrogen / embrittlement / plasticity / localization

1. Introduction

Hydrogen embrittlement, or hydrogen-induced fracture, is a severe environmental type of failure (Birnbaum, 1979, 1983, 1984, 1994; Birnbaum and Sofronis, 1994; Birnbaum et al., 1997; Hirth, 1980, 1984; Johnson, 1984). When hydrogen is present, materials fail at load levels that are very low compared with those that a hydrogen-free material can sustain. Of the many suggestions for an explanation of the hydrogen related failures, the mechanism of hydrogen enhanced localized plasticity (HELP) appears to be a viable one (Beachem, 1972; Meyers et al., 1992; Sirois et al., 1992; Birnbaum, 1988, 1994; Shih et al., 1988; Birnbaum and Sofronis, 1994). Arguments in support of the HELP mechanism are based on experimental observations (Sirois et al., 1992 and Sirois and Birnbaum, 1992) and theoretical calculations (Sofronis and Birnbaum, 1995 and Sofronis, 1995) that in a range of temperatures and strain rates, the presence of hydrogen in solid solution decreases the barriers to dislocation motion, thereby increasing the amount of deformation that occurs in a localized region adjacent to the fracture surface (Tabata and Birnbaum, 1983, 1984; Robertson and Birnbaum, 1986; Bond et al., 1987, 1988; Rozenak et al., 1990; Eastman et al., 1981). The fracture process is a highly localized ductile rupture process rather than an embrittlement (Lee et al., 1977, 1979-a, 1979-b and Onyewenyi and Hirth, 1983). This counterintuitive argument says that the macroscopic ductility is limited by the onset of extensive localized plasticity and is supported by microscopic observations. High-resolution fractography of hydrogen embrittled metals, such as Ni and Fe, show extensive plastic deformation localized along the fracture surfaces (Eastman et al., 1981 and Matsumoto et al., 1981). The technique of in-situ environmental cell deformation and fracture

* Correspondence and reprints.

E-mail address: sofronis@uiuc.edu (P. Sofronis).

carried out for bcc, fcc, and hcp metals having various solute contents, precipitation strengthened alloys, and intermetallics (Tabata and Birnbaum, 1983, 1984; Robertson and Birnbaum, 1984, 1986; Bond et al., 1987, 1988; Rozenak et al., 1990; Xiao, 1993) demonstrates the same localized plasticity character of hydrogen embrittlement despite some differing details among the various cases.

The underlying principle in the HELP mechanism is the shielding of the elastic interactions between dislocations and obstacles by the hydrogen solutes (Sirois and Birnbaum, 1992; Birnbaum and Sofronis, 1994; Sofronis and Birnbaum, 1995; Sofronis, 1995). Reduction of the interaction energies between elastic stress centers results in enhanced dislocation mobility. This phenomenon is supported by strong experimental evidence and has been observed in fcc (Robertson and Birnbaum, 1986), bcc (Tabata and Birnbaum, 1984), and hcp (Shih et al., 1988) systems and in relatively pure materials, in solid solutions alloys, in precipitation strengthened alloys (Bond et al., 1987), and in γ' strengthened alloys (Robertson and Birnbaum (unpublished work on gamma prime strengthened alloys, 1987); Robertson et al., 1984). As a consequence, the intrinsic material flow stress varies with position in an inhomogeneous distribution of hydrogen and is lower where the hydrogen concentration is greater.

The critical question though that still remains unanswered is how this hydrogen induced material softening at the microscale can cause shear localization at the macroscale. As Birnbaum et al. (1997) discuss, it is clear that the flow stress in the region of localization is reduced relative to the flow stress in the homogeneously deforming volume, but the mechanism by which hydrogen causes shear localization has not been established as of yet.

The purpose of this work is to provide a theoretical explanation for the onset of the shear localization in the presence of hydrogen from a solid mechanics point of view. First, the amount of hydrogen in the specimen is calculated by considering the extent of plastic straining (trapped hydrogen) and hydrostatic stress (normal interstitial hydrogen). In view of the very high mobility of the hydrogen solute, hydrogen concentration in trapping sites is assumed always to be in equilibrium with hydrogen in interstitial sites, which is also assumed to be in equilibrium with local hydrostatic stress. The calculated hydrogen concentration is then used to estimate the amount of material softening along the lines of the experimental observations by Tabata and Birnbaum (1983). The underlying idea is that by accounting for the hydrogen effect on the material constitutive law one can predict the onset of plastic instability in a homogeneously deforming specimen stressed in uniaxial tension. The criterion for the inception of such deformation instability is based on the analytical framework established by the work of Rice (1976) and Rudnicki and Rice (1975).

It should be pointed out that the numerical predictions of shear localization in our chosen model system, e.g. niobium, turn out to be independent of the amount of trapped hydrogen. However, this result is an exception rather than the rule and only a consequence of the trapping model assumed, as discussed in Section 6. To preserve the generality of the present model, as it could apply to other systems with different trapping mechanisms and characteristics, the trapping effect is included in the analysis.

2. Equilibrium hydrogen populations in normal interstitial lattice sites (NILS) and trapping sites

Hydrogen is assumed to reside either at normal interstitial lattice sites or reversible trapping sites at microstructural defects generated by plastic deformation. The two populations are always in equilibrium according to Oriani's theory (1970), such that:

$$\frac{\theta_T}{1 - \theta_T} = \frac{\theta_L}{1 - \theta_L} K_T, \quad (1)$$

where θ_L denotes the occupancy of the interstitial sites, θ_T denotes the occupancy of the trapping sites,

$$K_T = \exp(W_B/RT) \quad (2)$$

represents the equilibrium constant, W_B is the trap binding energy, R is the gas constant equal to $8.31 \text{ J mole}^{-1} \text{ K}^{-1}$ and T is the absolute temperature. The hydrogen concentration C_T , measured in atoms per unit volume, in trapping sites can be phrased as:

$$C_T = \theta_T \alpha N_T, \quad (3)$$

where α denotes the number of sites per trap and N_T denotes the trap density measured in number of traps per unit volume. The hydrogen concentration C_L , measured in hydrogen atoms per unit volume, in interstitial sites can be stated as:

$$C_L = \theta_L \beta N_L, \quad (4)$$

where β denotes the number of NLS per solvent atom and N_L denotes the number of solvent atoms per unit lattice volume given by:

$$N_L = N_A/V_M, \quad (5)$$

where $N_A = 6.0232 \times 10^{23}$ atoms per mole is Avogadro's number and V_M is the molar volume of the host lattice measured in units of volume per lattice mole.

Hydrogen concentrations in the NLS are studied under equilibrium conditions with local Cauchy stress σ_{ij} . The Fermi–Dirac form (Hirth and Carnahan, 1978) is used to calculate the equilibrium hydrogen concentration C_L in terms of the unstressed lattice concentration C_0 (initial NLS concentration in the absence of any stress, measured in hydrogen atoms per unit volume) as:

$$\frac{\theta_L}{1 - \theta_L} = \frac{\theta_L^0}{1 - \theta_L^0} K_L, \quad (6)$$

where $\theta_L^0 = C_0/\beta N_L$ denotes the initial NLS occupancy,

$$K_L = \exp(\sigma_{kk} V_H/3RT) \quad (7)$$

is the equilibrium constant dominated by the first-order interaction of hydrogen with stress, V_H is the partial molar volume of hydrogen in solution, and the standard summation convention is used over repeated indices throughout. Transient effects of the type calculated by Fuentes-Samaniego et al. (1984) are not accounted for.

If c_L is the hydrogen concentration in NLS denoting hydrogen atoms per solvent atom:

$$c_L = C_L/N_L = \beta \theta_L \quad (8)$$

by equation (4). Then, the relationship between the corresponding measures for the initial NLS concentration in the unstressed lattice is $c_0 = C_0/N_L$. Similarly, introducing a trapping site concentration c_T measured in trapped hydrogen atoms per solvent atom such that:

$$c_T = C_T/N_L = \beta \theta_T, \quad (9)$$

one calculates $\theta_{TL} = \alpha N_T \theta_T / \beta N_L$ by equation (3). In order for the maximum concentration in both NLS and trapping sites not to exceed that for the MH structure, that is, for the metal hydride, the side condition:

$$c = c_T + c_L \leq 1 \quad (10)$$

is imposed, where c is the total hydrogen concentration in both NILS and trapping sites and is measured in hydrogen atoms per solvent atom.

In this paper the hydrogen trap sites are associated with dislocations in the deforming metal (Thomas, 1980 and Angelo et al., 1996). Assuming one trap site per atomic plane threaded by a dislocation (Thomas, 1980; Tien et al., 1976; McLellan, 1979), one finds that the trap site density in traps per cubic meter is given by:

$$N_T = \sqrt{2} \rho / a, \quad (11)$$

where ρ is the dislocation density and a is the lattice parameter. Lufrano et al. (1998) maintain that this assumption is consistent with the experimental work of Thomas (1980) in which the best fit to the experimental data was obtained with a trapping radius of only 1 to 2 atomic spacings. The dislocation density ρ measured in dislocation line length per cubic meter was considered to vary linearly with logarithmic strain ε^p (Gilman, 1969):

$$\rho = \begin{cases} \rho_0 + \gamma \varepsilon^p & \text{for } \varepsilon^p < 0.5, \\ 10^{16} & \text{for } \varepsilon^p \geq 0.5, \end{cases} \quad (12)$$

where $\rho_0 = 10^{10}$ line length/m³ denotes the dislocation density for the annealed material and $\gamma = 2.0 \times 10^{16}$ line length/m³.

Combination of equations (1)–(3), (6)–(12) yields the total hydrogen concentration as a function of both the hydrostatic stress and the equivalent plastic strain, that is:

$$c = \beta [\theta_L(\sigma_{kk}) + \theta_{TL}(\sigma_{kk}, \varepsilon^p)], \quad (13)$$

where

$$\theta_L(\sigma_{kk}) = \theta_L^0 K_L / [(1 - \theta_L^0) + \theta_L^0 K_L] \quad (14)$$

and

$$\theta_{TL}(\sigma_{kk}, \varepsilon^p) = \frac{\alpha N_T(\varepsilon^p)}{\beta N_L} \frac{K_T \theta_L(\sigma_{kk})}{1 - \theta_L(\sigma_{kk}) + K_T \theta_L(\sigma_{kk})}. \quad (15)$$

3. Continuum description of the hydrogen induced softening effect

Birnbaum and Sofronis (1994) have argued that at temperatures and strain rates in which hydrogen embrittlement is experimentally observed, hydrogen induces material softening at the microscale by enhancing the dislocation mobility. In a continuum sense, softening can be described through a local flow stress that decreases with increasing hydrogen concentration. It is important to emphasize here that the term ‘local flow stress’ denotes the intrinsic flow characteristics of a small volume of material in the microscale, most likely in the neighborhood of a stress raiser, where hydrogen has concentrated by deformation. ‘Local flow stress’ should not be confused with the flow stress measured ‘macroscopically,’ say, in a tensile test. The reason is that while the intrinsic material flow stress decreases with hydrogen (Meyers et al., 1992), the macroscopically measured flow stress may either decrease (Beachem, 1972; Matsui et al., 1979-a, 1979-b; Moriya et al., 1979; Eastman et al., 1982) or increase with hydrogen (Asano and Otsuka, 1976; Abraham and Altstetter, 1995) depending on the degree of hydrogen induced shear localization and the magnitude of the local softening due to the removal of dislocation barriers (Birnbaum, 1994; Birnbaum and Sofronis, 1994).

Indeed, Birnbaum (1994) and Birnbaum and Sofronis (1994) demonstrated that when softening induced shear localization takes place, the number of moving dislocations within the specimen reduces since the bulk of

the material outside the shear band(s) ceases to deform. As a result, the dislocation velocity increases in order for the macroscopically imposed machine strain rate to be maintained. Since stress is a response function, this increased dislocation velocity results in an increase of the macroscopic stress (macroscopic hardening). On the other hand, in the absence of shear localization, the macroscopic stress decreases because the dislocations throughout the specimen can keep moving with the same velocity at a lower stress due to shielding of their interactions by hydrogen (macroscopic softening). For example, in the case of stainless steels severe slip localization on a limited number of slip planes is accompanied by significant increases in the macroscopic flow stress (Ulmer and Altstetter, 1991; Abraham and Altstetter, 1995). On the other hand, macroscopic flow stress reduction is observed in the aluminum–hydrogen system (Zeides, 1986) because initial hydrogen clusters which act as barriers to dislocation motion are removed (cut through) by hydrogen enhanced dislocation mobility set by the initial deformation.

It is notable that the experimental procedures used to demonstrate hydrogen-induced hardening have been subject to criticism. Near surface damage by the severe concentration gradients on the surface due to hydrogen charging, phase transformations, and stress induced hydrides at dislocation cores have often been suggested to be the true mechanisms in the observed hydrogen induced hardening (Kimura and Birnbaum, 1987; Birnbaum and Sofronis, 1994). A detailed presentation and discussion of experimental studies of hydrogen induced macroscopic hardening and softening can be found in the work by Abraham and Altstetter (1995).

Based on microscopic studies of the effect of hydrogen on dislocation behavior in iron, Tabata and Birnbaum (1983) determined the local flow stress of the material as a decreasing function of the hydrogen pressure in the environmental cell. Such an experimental observation warrants a continuum description of the hydrogen effect on the local flow stress σ_Y in the form of:

$$\sigma_Y = \sigma_0^H \left(1 + \frac{\varepsilon^P}{\varepsilon_0} \right)^{1/n}, \quad (16)$$

where σ_0^H is the initial yield stress in the presence of hydrogen that decreases with increasing hydrogen concentration, ε_0 is the initial yield strain in the absence of hydrogen, ε^P is the logarithmic strain in uniaxial tension, and n is the hardening exponent that is assumed unaffected by hydrogen. Equation (16) suggests that the hydrogen effect on the local continuum flow characteristics is modeled through the initial yield stress, assumed to be given by:

$$\sigma_0^H = \phi(c)\sigma_0, \quad (17)$$

where $\phi(c)$ is a monotonically decreasing function of the local hydrogen concentration c measured in atoms per solvent lattice atom, and σ_0 is the initial yield stress in the absence of hydrogen. It is assumed that local hydrogen concentrations are such that $c \leq 1$, which is typical in bcc systems in which the MH (Metal hydride) structure is allowed to be formed. A possible suggestion for $\phi(c)$ is a linear form:

$$\phi(c) = (\xi - 1)c + 1, \quad (18)$$

where $\xi < 1$ is a parameter. Note that if $c = 1$, then $\phi = \xi$ and $\sigma_0^H = \xi\sigma_0$ denote the ratio of the yield stress in the presence of hydrogen, σ_0^H , to that in the absence of hydrogen, σ_0 , at the maximum hydrogen concentration of 1.

The proposed model of equations (16)–(18) for the hydrogen induced material softening should be understood not as a precise and exhaustive description of the experimental findings. Rather, the model should be viewed as an attempt to quantify the experimental understanding of the hydrogen effect on dislocation mobility in a continuum sense. By requiring that ξ is finite and positive, the model does not allow for the

material yield stress to vanish as the hydrogen content c approaches unity. This is indeed an expected realistic feature of the model if one considers that dislocation motion has not been observed to increase indefinitely with hydrogen. In fact, in the present investigation and for low or moderate initial concentrations, that is, for $c_0 \leq 0.3$ H/M (H/M denotes hydrogen atoms per metal atom), the function ϕ never assumes values less than 0.69. Therefore, hydrogen never causes the yield stress to reduce by more than 31% in this concentration range. Since the work hardening exponent in equation (1) is treated as independent of hydrogen, the model does not suggest a hydrogen induced change in the deformation mechanism at the microscale. This is also in accordance to the emerging understanding in recent years (Birnbbaum et al., 1997) that hydrogen induces material degradation not by altering the local material deformation mechanism, but rather by intensifying it.

4. Constitutive law and conditions for shear localization

4.1. Elastoplastic constitutive law

The total deformation rate tensor D_{ij} (which equals the symmetric part of the velocity gradient in spatial coordinates) is written as the sum of an elastic part, a part due to the presence of hydrogen, and a plastic part:

$$D_{ij} = D_{ij}^e + D_{ij}^h + D_{ij}^p. \quad (19)$$

The elastic behavior of the material is modeled as hypo-elastic, linear and isotropic:

$$D_{ij}^e = \frac{1}{2G} \overset{\nabla}{\sigma}'_{ij} + \frac{1}{9K} \overset{\nabla}{\sigma}_{kk} \delta_{ij}, \quad (20)$$

where the superposed ∇ denotes the Jaumann or co-rotational stress rate (which exhibits proper material invariance for rigid spin), $\overset{\nabla}{\sigma}'_{ij} = \sigma_{ij} - \sigma_{kk} \delta_{ij} / 3$ is the deviatoric stress, δ_{ij} is the Kronecker delta, and G and K are the elastic shear and bulk moduli respectively.

The stress-free solid at initial solute concentration c_0 is taken as the reference state for measuring strain due to hydrogen induced lattice distortion. The mechanical effect of the hydrogen solute atoms is purely dilatational (Peisl, 1978) and is phrased in terms of the deformation rate as:

$$D_{ij}^h = \dot{\varepsilon}^h \delta_{ij}, \quad \text{where } \varepsilon^h = \ln \left[1 + \frac{\lambda(c - c_0)}{3} \right], \quad (21)$$

a superposed dot denotes material time differentiation, $\lambda = \Delta v / \Omega$, Δv is the volume change per atom of hydrogen introduced into solution that is directly related to the partial molar volume of hydrogen $V_H = \Delta v N_A$ in solution, and Ω is the mean atomic volume of the host metal atom. In view of the definition of ε^h , the expression for D_{ij}^h can be written as

$$D_{ij}^h = \frac{1}{3} \Lambda(c) \dot{c} \delta_{ij}, \quad (22)$$

where $\Lambda(c) = \lambda / [1 + \lambda(c - c_0) / 3]$. Note that for small changes of concentration, $\Lambda(c) \approx \lambda$ and equation (22) reduces to the usual infinitesimal strain rate $\dot{\varepsilon}_{ij}^h = (\dot{c} \Delta v / 3 \Omega) \delta_{ij}$ (Sofronis, 1995).

The material is assumed to be rate independent, to yield according to the von-Mises criterion, and to harden isotropically under plastic straining. The yield criterion is of the form:

$$f = \sigma_e - \sigma_Y(\varepsilon^p, c) = 0, \quad (23)$$

where $\sigma_e = (3\sigma'_{ij}\sigma'_{ij}/2)^{1/2}$ is the von-Mises equivalent stress, the equivalent plastic strain ε^p is defined as $\varepsilon^p = \int \sqrt{2D_{ij}^p D_{ij}^p}/3 dt$, and the flow stress $\sigma_Y(\varepsilon^p, c)$ is defined by equations (16) and (17). The plastic part of the deformation rate is defined by the so-called ‘normality condition’:

$$D_{ij}^p = \dot{\varepsilon}^p \frac{\partial f}{\partial \sigma_{ij}} = \dot{\varepsilon}^p \frac{3\sigma'_{ij}}{2\sigma_e}. \tag{24}$$

Using the ‘consistency condition’

$$\dot{f} = \frac{\partial f}{\partial \sigma_{ij}} \dot{\sigma}_{ij} + \frac{\partial f}{\partial \varepsilon^p} \dot{\varepsilon}^p + \frac{\partial f}{\partial c} \dot{c} = 0, \tag{25}$$

and taking into account the fact that c is a function of σ_{kk} and ε^p (see equations (13–15)), one concludes that:

$$D_{ij}^p = \frac{1}{\frac{\partial \sigma_Y}{\partial \varepsilon^p} + \frac{\partial \sigma_Y}{\partial c} \frac{\partial c}{\partial \varepsilon^p}} \left(\frac{3\sigma'_{kl}}{2\sigma_e} - \frac{\partial \sigma_Y}{\partial c} \frac{\partial c}{\partial \sigma_{pp}} \delta_{km} \delta_{lm} \right) \frac{3\sigma'_{ij} \overset{\nabla}{\sigma}_{kl}}{2\sigma_e}. \tag{26}$$

Substitution of equations (20), (22), and (26) into equation (19) yields the full description of the material constitutive law as follows:

$$\begin{aligned} 2D'_{ij} &= \frac{\overset{\nabla}{\sigma}'_{ij}}{G} + \frac{1}{\frac{1}{3} \left(\frac{\partial \sigma_Y}{\partial \varepsilon^p} + \frac{\partial \sigma_Y}{\partial c} \frac{\partial c}{\partial \varepsilon^p} \right)} \frac{3\sigma'_{ij}}{\sigma_e} \left(\frac{\sigma'_{kl} \overset{\nabla}{\sigma}_{kl}}{2\sigma_e} - \frac{1}{3} \frac{\partial \sigma_Y}{\partial c} \frac{\partial c}{\partial \sigma_{kk}} \overset{\nabla}{\sigma}_{mm} \right), \\ D_{kk} &= \frac{\overset{\nabla}{\sigma}_{kk}}{3\bar{K}} + \frac{\frac{\partial c}{\partial \varepsilon^p} \Lambda(c)}{\frac{1}{3} \left(\frac{\partial \sigma_Y}{\partial \varepsilon^p} + \frac{\partial \sigma_Y}{\partial c} \frac{\partial c}{\partial \varepsilon^p} \right)} \left(\frac{\sigma'_{kl} \overset{\nabla}{\sigma}_{kl}}{2\sigma_e} - \frac{1}{3} \frac{\partial \sigma_Y}{\partial c} \frac{\partial c}{\partial \sigma_{kk}} \overset{\nabla}{\sigma}_{mm} \right), \end{aligned} \tag{27}$$

where $\bar{K} = K/[1 + 3(\partial c/\partial \sigma_{kk})K \Lambda(c)]$.

Comparing the constitutive equations (27) to equations (10) of Rudnicki and Rice (1975), one finds direct analogy between material behavior in the presence of hydrogen and the behavior of pressure sensitive dilatant materials considered by Rudnicki and Rice. In order for the respective equations to be identical, the parameter correspondence is as follows:

Present work	Rudnicki and Rice (1975)
$\frac{1}{3} \left(\frac{\partial \sigma_Y}{\partial \varepsilon^p} + \frac{\partial \sigma_Y}{\partial c} \frac{\partial c}{\partial \varepsilon^p} \right)$	$\rightarrow h$
$\frac{\Lambda(c)}{\sqrt{3}} \frac{\partial c}{\partial \varepsilon^p}$	$\rightarrow \beta$
$-\sqrt{3} \frac{\partial \sigma_Y}{\partial c} \frac{\partial c}{\partial \sigma_{kk}}$	$\rightarrow \mu$
\bar{K}	$\rightarrow K$

where the parameters $h, \beta, \mu,$ and K in the work of Rudnicki and Rice denote correspondingly the slope of the effective stress–effective plastic strain curve in shear, the dilatancy factor, the pressure sensitivity of yield, and the material bulk modulus. Clearly, hydrogen affects both the material dilatancy and the sensitivity of yield. In

addition, because $\partial c/\partial \varepsilon^p > 0$ and $\partial \sigma_Y/\partial c < 0$, hydrogen reduces the slope of the equivalent stress–equivalent strain curve, thus favoring localization.

4.2. Conditions for localization

Let $Ox_Ix_{II}x_{III}$ be a Cartesian coordinate system aligned with the principal stress directions, and $\sigma'_I \geq \sigma'_{II} \geq \sigma'_{III}$ be the principal deviatoric stresses. According to Rudnicki and Rice (1975) and Perrin and Leblond (1993) localization of the plastic flow is possible when the hardening modulus:

$$h = \frac{1}{3} \left(\frac{\partial \sigma_Y}{\partial \varepsilon^p} + \frac{\partial \sigma_Y}{\partial c} \frac{\partial c}{\partial \varepsilon^p} \right) \quad (29)$$

reduces upon loading to the critical value:

$$\begin{aligned} \frac{h_{cr}}{G} = & \frac{1 + \bar{\nu}}{9(1 - \bar{\nu})} (\beta - \mu)^2 - \frac{1 + \bar{\nu}}{2} \left(N_{II} + \frac{\beta + \mu}{3} \right)^2 \\ & + \frac{(4 - 3N_{II}^2)(1 + \bar{\nu})}{24\sqrt{3}(1 - \bar{\nu})} (\beta - \mu) (\sin 2\theta_0)^2 \frac{\sigma_e}{G} + O\left(\frac{\sigma_e}{G}\right)^2, \end{aligned} \quad (30)$$

where $\bar{\nu} = (3\bar{K} - 2G)/(6\bar{K} + 2G)$, $\tan \theta_0 = \sqrt{(\xi - N_{III})/(N_I - \xi)}$, $N_i = \sqrt{3}\sigma'_i/\sigma_e$, $i = I, II, III$, $\xi = [(1 + \bar{\nu})(\beta + \mu)/3] - N_{II}(1 - \bar{\nu})$, and the loading is such that $N_{III} < \xi < N_I$. Rudnicki and Rice also show that the unit normal \mathbf{n} to the plane of the shear band is perpendicular to the direction x_{II} , and that the angle θ between \mathbf{n} and direction x_{III} is:

$$\theta = \theta_0 + \frac{1}{\sqrt{3}} \left[\frac{1 + \bar{\nu}}{6} (\mu - \beta) \cot 2\theta_0 - \frac{1}{4} \left(1 - \frac{3}{4} N_{II}^2 \right)^{1/2} \sin 2\theta_0 \right] + O\left(\frac{\sigma_e}{G}\right)^2. \quad (31)$$

5. Hydrogen-induced shear localization in plane strain uniaxial tension

The conditions for shear localization are studied in the case of a specimen loaded in homogeneous uniaxial tension under plane strain deformation (see *figure 1*). Loading is effected incrementally by applying displacement increments along the x_2 -axis. Before the application of the external load, the specimen was assumed to be stress free and at a uniform initial hydrogen concentration c_0 . Upon loading, uniform redistribution of the H solutes occurs within the solid so that hydrogen is always under quasi-static ‘local equilibrium’ conditions with local stress and plastic strain as discussed in Section 2 (cf. equation (13)). Since hydrogen is assumed to be provided by a chemical reservoir, an arrangement corresponding to ‘far field concentration’ kept constant at c_0 , the calculation corresponds to a constant chemical potential for the hydrogen solute. The first increment of the displacement was such that the specimen was brought to yield as determined by equation (17). Subsequently, the loading was continued with the specimen deforming in the elastoplastic regime. Localization of plastic flow is possible when the hardening modulus h , defined by equation (29), reduces upon loading to the critical value h_{cr} , determined by equation (30).

The solution to the problem of plane strain tension was obtained numerically; details of the calculation are reported in the Appendix.

The numerical computations were carried out with regard to the niobium system, as material data are available for this system. The initial trapping site concentration was calculated from equations (1)–(4), with

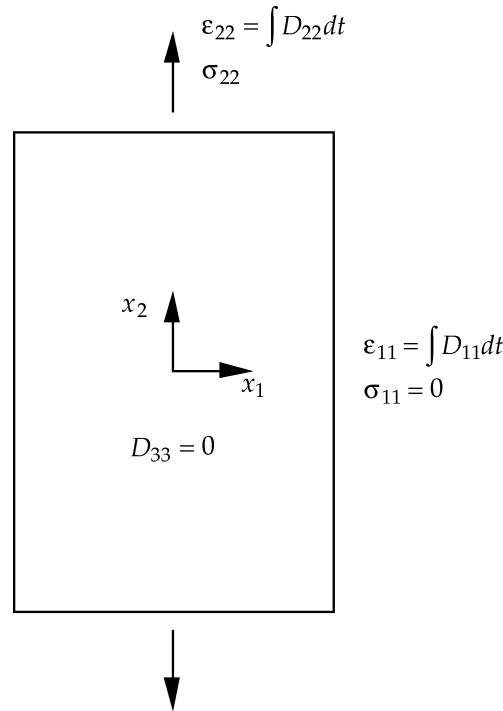


Figure 1. A specimen strained homogeneously in plane strain by displacement increments in the x_2 direction. In the absence of deformation, the specimen is at an initial concentration c_0 measured in hydrogen atoms per solvent atom (H/M).

the parameter α taken to be equal to 1. The parameter β was set equal to 1 and this corresponds to a maximum NLS concentration of 1 hydrogen atom per solvent lattice atom. Hydrogen was assumed to expand the lattice isotropically and its partial molar volume in solution was $V_H = 1.88 \text{ cm}^3/\text{mole}$ which corresponds to $\lambda = 0.174$. The molar volume of niobium was $10.852 \times 10^{-6} \text{ m}^3/\text{mole}$ which implies that the number of the available NLS was $N_L = 5.55 \times 10^{28}$ solvent lattice atoms per m^3 . The lattice parameter was $a = 3.3 \times 10^{-10} \text{ m}$, the Poisson's ratio $\nu = 0.34$, and Young's modulus $E = 115 \text{ GPa}$. The trap binding energy was taken to be equal to $W_B = 29.2 \text{ kJ/mole}$ (Baker and Birnbaum, 1972) and the temperature was 300 K.

Figure 2 shows the normalized stress σ_{22}/σ_0 plotted against the equivalent plastic strain during straining up to the localization event for given initial concentrations c_0 , material yield stress in the absence of hydrogen $\sigma_0 = 400 \text{ MPa}$, and hardening exponent $n = 10$. It is evident that as the initial concentration increases, the material becomes increasingly softer with decreasing tangent modulus, in accordance with the softening behavior described by equations (17) and (18). Notice that while for the hydrogen free material initial yielding is attained at $\sigma_{22}/\sigma_0 = 1.14$, when $c_0 = 0.8 \text{ H/M}$ the corresponding stress is $\sigma_{22}/\sigma_0 = 0.28$. This behavior is strongly dependent on the value of the parameter ξ which defines the reduction of the yield stress at the maximum hydrogen concentration of 1 (see equations (17) and (18)); the value $\xi = 0.1$ is used in the calculations. *Figure 3* shows the normalized concentration c/c_0 plotted against the equivalent plastic strain as a function of c_0 . The relative elevation of the concentration c above the initial concentration c_0 reduces with increasing c_0 . This is a direct consequence of the softening-induced decrease in the stress triaxiality $\sigma_{kk} = \sigma_{22} + \sigma_{33}$ with increasing initial concentration. *Figure 4* shows the macroscopic normalized true (logarithmic) strain $\varepsilon_{22}/\varepsilon_0$ at localization plotted against the initial hydrogen concentration c_0 , for work hardening exponents $n = 5$ and 10 and yield stress $\sigma_0 = 400 \text{ MPa}$. The macroscopic strain for localization reduces with initial concentration c_0 provided $c_0 \leq 0.64 \text{ H/M}$ and $c_0 \leq 0.66 \text{ H/M}$ for $n = 5$ and $n = 10$ respectively. On the other hand, for initial concentrations greater than 0.64 H/M and 0.66 H/M respectively for $n = 5$ and $n = 10$, the dependence of

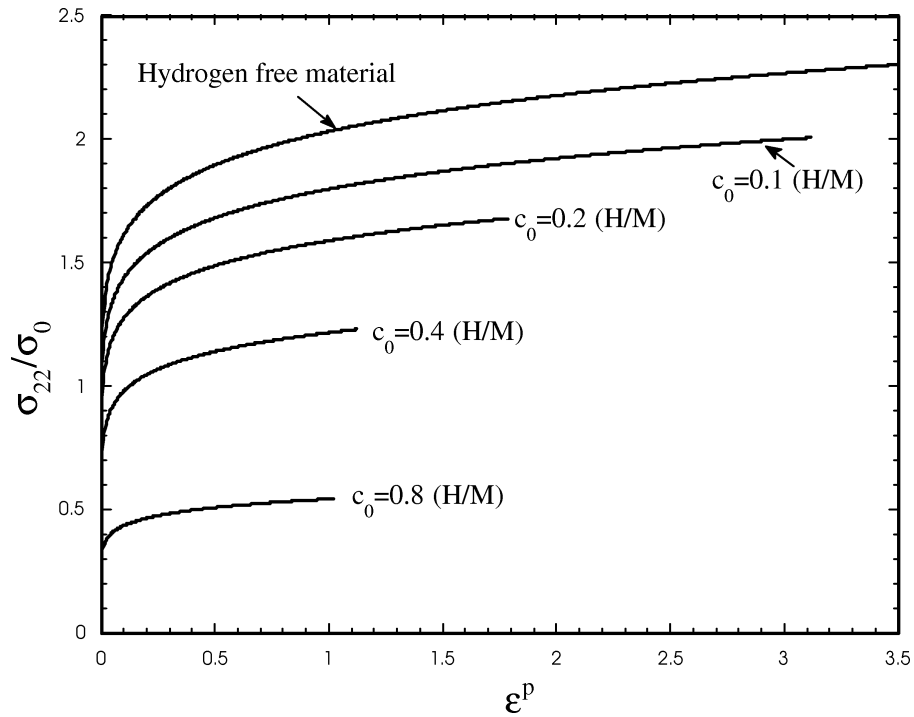


Figure 2. Plot of the normalized stress σ_{22}/σ_0 versus the effective plastic strain ϵ^P for various initial concentrations c_0 . The parameter $\sigma_0 = 400$ MPa is the initial yield stress in the absence of hydrogen. The work hardening exponent was $n = 10$ and the softening parameter ξ was 0.1.

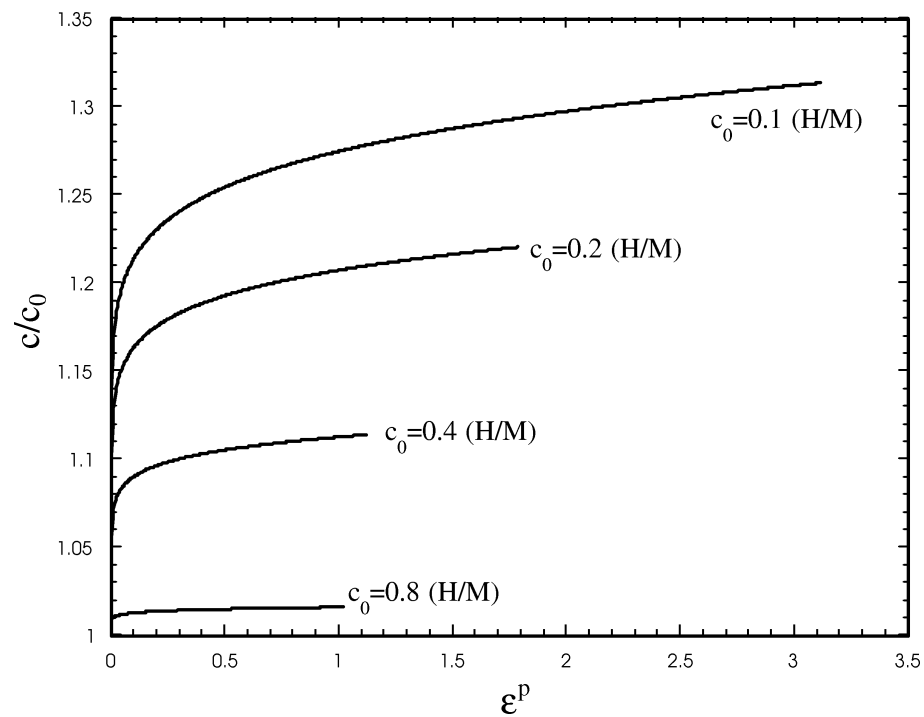


Figure 3. Plot of the normalized hydrogen concentration c/c_0 versus the effective plastic strain ϵ^P for various initial concentrations c_0 . The parameter $\sigma_0 = 400$ MPa is the initial yield stress in the absence of hydrogen. The work hardening exponent was $n = 10$ and the softening parameter ξ was 0.1.

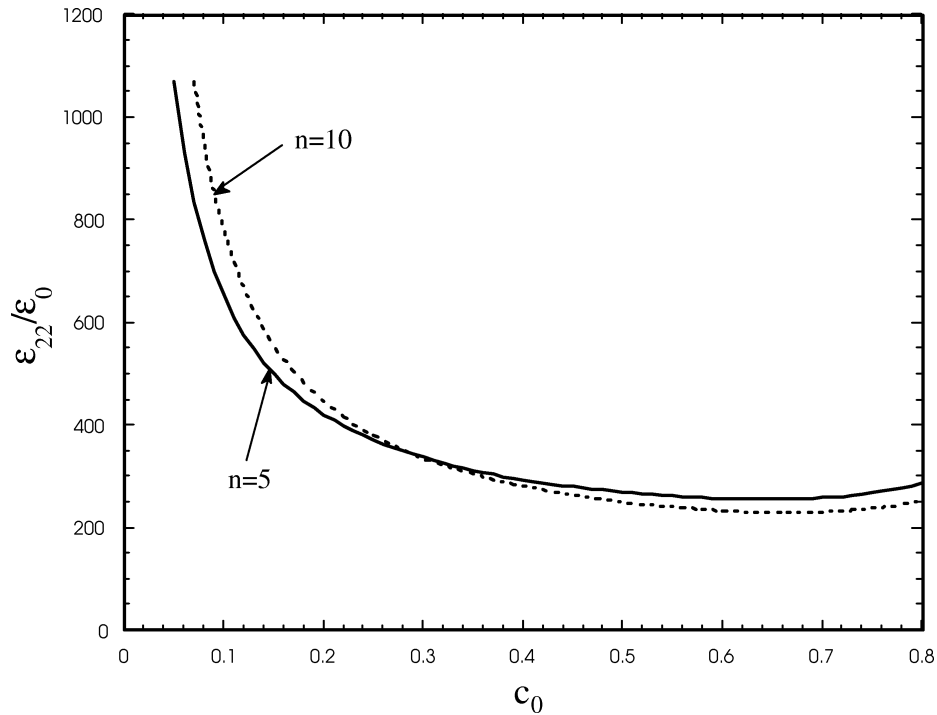


Figure 4. Plot of the normalized macroscopic strain ϵ_{22}/ϵ_0 at localization, bifurcation versus the initial concentrations c_0 for hardening exponents $n = 5, 10$. The parameter ϵ_0 is the initial yield strain corresponding to the yield stress $\sigma_0 = 400$ MPa. The softening parameter ξ was 0.1.

the slope on the initial concentration reverses and the critical strain for localization ϵ_{22} exhibits only a weak dependence on c_0 .

Figure 4 indicates that for initial concentrations c_0 less than 0.29 H/M, the applied strain for localization increases with reducing hardening, i.e. with increasing n . This result is physically plausible because the stress triaxiality necessary to elevate the local concentration c to the levels required for the onset of the localization is achieved at higher strains for the softer material. On the other hand, for initial concentrations greater than 0.29 H/M, the more severe material softening at higher values of n is essentially the factor that governs the condition for localization, and therefore the elevation of triaxiality (i.e. local concentration) required when $n = 10$ is less than that at $n = 5$. This is in accordance with the mild elevations of the hydrogen concentration at high initial concentrations (e.g. $c_0 = 0.8$ H/M) compared to the marked elevations at low initial concentrations (e.g. $c_0 = 0.1$ H/M), as shown in figure 3.

6. Discussion

It was demonstrated theoretically that hydrogen can promote localization of the homogeneous macroscopic plastic deformation into bands of intense shear. The model is based on hydrogen induced intrinsic material softening and lattice dilatation both of which have been experimentally verified. The effect of hydrogen is demonstrated in causing the critical modulus for localization to be positive.

The macroscopic strain at which localization takes place depends strongly on the initial hydrogen concentration c_0 . At high initial concentrations ($c_0 > 0.3$ H/M), localization has been found in the niobium system (with $n = 10$) to take place at a macroscopic strain of less than $336\epsilon_0$ and greater than $230\epsilon_0$. This range corresponds to strains of $80 \div 117\%$. At the initial concentration of $c_0 = 0.3$ H/M, which is moderately

high, localization takes place while the local hydrogen concentration is $c = 0.348 \text{ H/M}$. At this concentration, the model's prediction is based on the assumption that the local initial yield stress has been reduced to 69% of the yield stress in the absence of hydrogen according to equations (17) and (18). This is not an unrealistic underlying model assumption in view of the experimental evidence on the strong effect of hydrogen on dislocation mobility. Using dislocation velocity measurements, Tabata and Birnbaum (1983) calculated that a reduction of the yield stress by 31% can be achieved at low hydrogen pressures.

Although precise experimental measurements on the strain at localization do not exist, it is generally believed that localization takes place at macroscopic strains, which are close to those just after the material begins to yield. Abraham and Altstetter (1995) observed notable slip localization during tensile tests with 310s stainless steel foils containing as little as 8 at % of hydrogen at macroscopic strain of about 2%. The localization was always accompanied by a negative slope (yield point discontinuity: upper and lower yield point) in the macroscopic stress–strain curve. Of course in an inhomogeneous deformation field, in particular close to stress raisers such as internal defects, grain boundary incompatibilities, and microcracks, the local strain may be many times the initial yield strain ε_0 , while the macroscopic strain is just above yield.

Therefore, it can be said that the present model predicts that straining up to fairly high values of macroscopic strain (two orders of magnitude in excess of the material yield strain) is required for the onset of localization in the presence of hydrogen. It is well known that the von Mises flow theory dramatically overestimates the bifurcation strain. Perhaps predictions based on a modified flow model, e.g. one that is based on corner theory, can be one or two orders of magnitude less than those of the present model. However, to adopt such a constitutive model, experimental evidence is required to support that hydrogen can change the flow characteristics of a material in such a way (e.g. yield surface with vertices).

Also the high strains for the onset of localization in the present plane strain study should be viewed in relation to the minimal elevation of the equilibrium hydrogen concentration relatively to the initial concentration. In fact, in the numerical results, equilibrium concentrations c were never larger than the initial concentration c_0 by more than 31%. This is due to the low stress triaxiality attained in plane strain uniaxial tension (*figure 3*) and to the absence of strong hydrogen trapping as discussed below. As a result, both the dilatancy factor ($\sim \partial c / \partial \varepsilon^p$) and the pressure sensitivity of yield ($\sim \partial c / \partial \sigma_{kk}$) were not so dramatically affected (Rudnicki and Rice, 1975) as to allow for shear localization at strains lower than those shown in *figure 4*. It is expected that ahead of a crack tip where the stress triaxiality is higher and the elevation of the hydrogen concentration is much greater (Sofronis and McMeeking, 1989; Taha and Sofronis, 2001), the pressure sensitivity of yield will be higher. It is notable that in the case of high strength steels in which the trapping energy is twice as large as in niobium (Kumnick and Johnson, 1980), the trapped hydrogen concentrations at a crack tip can get as high as 80 times the initial concentration c_0 (Sofronis and McMeeking, 1989; Taha and Sofronis, 2001). Similarly a model of trapping in the form of hydrogen atmospheres around dislocations will also result in higher-pressure sensitivity. Evidently, further studies are required in order to address the sensitivity of the localization condition on the applied macroscopic strain.

In order to quantify the percentage of trapped hydrogen relatively to the total hydrogen in the specimen, one sees that the maximum trap density predicted by equations (11) and (12) is $4.3 \times 10^{25} \text{ traps/m}^3$. Since there are 5.55×10^{28} solvent lattice metal atoms per m^3 , one concludes that the trap density is 8×10^{-4} trap sites per solvent metal atom. At this level of trap site density, even with trap saturation, the amount of trapped hydrogen is very small relative to the interstitial hydrogen. As a result, the effect of the trap binding energy on the localization, bifurcation condition is negligible. Parametric studies with defect binding energies equal to 20 and 40 kJ/mole yielded results identical to those shown in *figure 4*.

7. Closure

The present model simulations predict that hydrogen induced localization of plastic deformation in the form of bands of intense shear is indeed a mechanism of deformation possibly occurring at the macroscale. The model is based on realistic material parameters and experimental studies of the hydrogen effect on dislocation mobility. The numerical results seem to overestimate the macroscopic strain required for localization as predicted by experiments. The calculated hydrogen effect can be intensified quantitatively by considering more effective trapping modes of hydrogen in the presence of higher stress triaxialities such as those ahead of a crack tip. The dependence of the hydrogen-induced localization on the nature of the material yield model will be considered in a subsequent publication.

Acknowledgments

This work was supported by the Department of Energy under grant DEFGO2-96ER45439. The authors would like to thank Professors H.K. Birnbaum and C.J. Altstetter for many helpful discussions on the physics of the hydrogen effect on the materials behavior.

Appendix

For the plane strain uniaxial tension problem described in Section 5, the only non-zero stress and deformation rate components are $\sigma_{22}, \sigma_{33}, D_{11} = \dot{\varepsilon}_{11}$, and $D_{22} = \dot{\varepsilon}_{22}$, where ε_{11} and ε_{22} are the logarithmic strains respectively in directions 1 and 2. The corresponding constitutive equations are:

$$\dot{\varepsilon}_{11} = -\frac{\nu}{E}(\dot{\sigma}_{22} + \dot{\sigma}_{33}) + \dot{\varepsilon}^h + \dot{\varepsilon}^p n_{11}, \quad (\text{A1})$$

$$\dot{\varepsilon}_{22} = \frac{1}{E}\dot{\sigma}_{22} - \frac{\nu}{E}\dot{\sigma}_{33} + \dot{\varepsilon}^h + \dot{\varepsilon}^p n_{22}, \quad (\text{A2})$$

$$\dot{\varepsilon}_{33} = -\frac{\nu}{E}\dot{\sigma}_{22} + \frac{1}{E}\dot{\sigma}_{33} + \dot{\varepsilon}^h + \dot{\varepsilon}^p n_{33} = 0, \quad (\text{A3})$$

where

$$n_{ij} = 3\sigma'_{ij}/2\sigma_e. \quad (\text{A4})$$

The yield condition is given by equation (23) as:

$$\sigma_e - \sigma_Y(\varepsilon^p, c) = 0, \quad (\text{A5})$$

and the hydrogen concentration c is given by equation (13) in the form of:

$$c = c(\sigma_{kk}, \varepsilon^p). \quad (\text{A6})$$

Initial yielding

The specimen yields upon loading when the following conditions are satisfied:

$$\varepsilon_{11} = -\frac{\nu}{E}(\sigma_{22} + \sigma_{33}) + \ln\left[1 + \frac{\lambda(c - c_0)}{3}\right], \quad (\text{A7})$$

$$\varepsilon_{22} = \frac{1}{E}\sigma_{22} - \frac{\nu}{E}\sigma_{33} + \ln\left[1 + \frac{\lambda(c - c_0)}{3}\right], \quad (\text{A8})$$

$$0 = -\frac{\nu}{E}\sigma_{22} + \frac{1}{E}\sigma_{33} + \ln\left[1 + \frac{\lambda(c - c_0)}{3}\right], \quad (\text{A9})$$

$$c = c(\sigma_{kk}, 0), \quad (\text{A10})$$

$$\sigma_{22}^2 + \sigma_{33}^2 - \sigma_{22}\sigma_{33} - \sigma_Y^2(0, c) = 0. \quad (\text{A11})$$

The above set of five non-linear equations is solved for σ_{22} , σ_{33} , ε_{11} , ε_{22} , and c by using the Newton iteration method.

Plasticity solution

Equations (A1) to (A3) are integrated by using a backward Euler scheme and the solution is determined by the following set of equations:

$$\Delta\varepsilon_{11} = -\frac{\nu}{E}(\Delta\sigma_{22} + \Delta\sigma_{33}) + \frac{1}{3}\Lambda(c_{n+1})\Delta c + \Delta\varepsilon^P(n_{11})_{n+1}, \quad (\text{A12})$$

$$\Delta\varepsilon_{22} = \frac{1}{E}\Delta\sigma_{22} - \frac{\nu}{E}\Delta\sigma_{33} + \frac{1}{3}\Lambda(c_{n+1})\Delta c + \Delta\varepsilon^P(n_{22})_{n+1}, \quad (\text{A13})$$

$$0 = -\frac{\nu}{E}\Delta\sigma_{22} + \frac{1}{E}\Delta\sigma_{33} + \frac{1}{3}\Lambda(c_{n+1})\Delta c + \Delta\varepsilon^P(n_{33})_{n+1}, \quad (\text{A14})$$

$$c_{n+1} = c((\sigma_{kk})_{n+1}, \varepsilon_{n+1}^P), \quad (\text{A15})$$

$$(\sigma_{22}^2)_{n+1} + (\sigma_{33}^2)_{n+1} - (\sigma_{22}\sigma_{33})_{n+1} - \sigma_Y^2(\varepsilon_{n+1}^P, c_{n+1}) = 0, \quad (\text{A16})$$

where the notation $A_{n+1} = A_n + \Delta A$ denotes the value of A at the end of the increment under consideration. For every increment, the value of $\Delta\varepsilon_{22}$ is prescribed and the quantities $\Delta\varepsilon_{11}$, $\Delta\sigma_{22}$, $\Delta\sigma_{33}$, Δc , and $\Delta\varepsilon^P$ are determined from the solution of (A12)–(A16) by using the Newton iteration method.

References

- Abraham, D.P., Altstetter, C.J., 1995. The effect of hydrogen on the yield and flow stress of an austenitic stainless steel. *Met. Trans. A* 26, 2849–2858.
- Angelo, J.E., Moody, N.R., Baskes, M.I., 1996. Modeling the segregation of hydrogen to lattice defects in nickel, in: Moody, N.R., Thompson, A.W. (Eds.), *Hydrogen Effects in Materials*. Trans. Met. Soc. AIME, New York, NY, pp. 161–170.
- Asano, S., Otsuka, R., 1976. The lattice hardening due to dissolved hydrogen in iron and steel. *Scr. Met.* 10, 1015–1020.
- Baker, C., Birnbaum, H.K., 1972. On the hydrogen-dislocation interaction in niobium. *Scr. Met.* 6, 851–853.
- Beachem, C.D., 1972. A new model for hydrogen-assisted cracking (hydrogen embrittlement). *Met. Trans.* 3, 437–451.
- Birnbaum, H.K., 1979. Hydrogen related failure mechanisms in metals, in: Foroulis, Z.A. (Ed.), *Environmental Sensitive Fracture of Engineering Materials*, Proceedings of Symposium on Environmental Effects on Fracture, Chicago, Illinois, October 24–26, 1977. Metallurgical Society of AIME, Warrendale, PA, pp. 326–360.
- Birnbaum, H.K., 1983. Hydrogen related fracture of metals, in: Latanision, R.A., Pickens, J.R. (Eds.), *Atomistics of Fracture*, Proceedings of a NATO Advanced Research Institute on Atomistics of Fracture, Calcatoggio, Corsica, France, May 22–31, 1981. Plenum Press, New York, pp. 733–765.
- Birnbaum, H.K., 1984. Hydrogen related second phase embrittlement of solids, in: Gibala, R., Hehemann, R.F. (Eds.), *Hydrogen Embrittlement and Stress Corrosion Cracking*, Proceedings of a Troiano Festschrift Symposium, Case Western Reserve University, June 1–3, 1980. ASM, Ohio, pp. 153–177.

- Birnbaum, H.K., 1988. Environment-induced cracking of metals, in: Gangloff, R.P., Ive, M.B. (Eds.), *Environment-induced Cracking of Metals*, First International Conference, Kohler, Wisconsin, 1988. NACE, Houston, TX, pp. 21–29.
- Birnbaum, H.K., 1994. Hydrogen effects on deformation-relation between dislocation behavior and the macroscopic stress–strain behavior. *Scr. Met.* 31, 149–153.
- Birnbaum, H.K., Sofronis, P., 1994. Hydrogen-enhanced localized plasticity – a mechanism for hydrogen related fracture. *Mater. Sci. & Eng. A* 176, 191–202.
- Birnbaum, H.K., Robertson, I.M., Sofronis, P., Teter, D., 1997. Mechanisms of hydrogen related fracture – A review, in: Magnin, T. (Ed.), *Corrosion Deformation Interactions CDI'96*, Second International Conference, Nice, France, 1996. The Institute of Materials, Great Britain, pp. 172–195.
- Bond, G.M., Robertson, I.M., Birnbaum, H.K., 1987. The influence of hydrogen on deformation and fracture processes in high-strength aluminum alloys. *Acta Metall.* 35, 2289–2296.
- Bond, G.M., Robertson, I.M., Birnbaum, H.K., 1988. Effects of hydrogen on deformation and fracture processes in high-purity aluminum. *Acta Metall.* 36, 2193–2197.
- Eastman, J., Matsumoto, T., Narita, N., Heubaum, N., Birnbaum, H.K., 1981. Hydrogen effects in nickel embrittlement or enhanced ductility?, in: Bernstein, I.M., Thompson, A.W. (Eds.), *Hydrogen in Metals*. Metallurgical Society of AIME, New York, pp. 397–409.
- Eastman, J., Heubaum, N., Matsumoto, T., Birnbaum, H.K., 1982. The effect of hydrogen on the solid solution strengthening and softening of nickel. *Acta Metall.* 30, 1579–1586.
- Fuentes-Samaniego, R., Gasca-Neri, R., Hirth, J.P., 1984. Solute drag on moving edge dislocations. *Phil. Mag. A* 49, 31–43.
- Hirth, J.P., 1980. Effects of hydrogen on the properties of iron and steel. *Met. Trans. A* 11, 861–890.
- Hirth, J.P., 1984. Theories of hydrogen induced cracking of steels, in: Gibala, R., Hehemann, R.F. (Eds.), *Hydrogen Embrittlement and Stress Corrosion Cracking*, Proceedings of a Troiano Festschrift Symposium, Case Western Reserve University, June 1–3, 1980. ASM, Ohio, pp. 29–41.
- Hirth, J.P., Carnahan, B., 1978. Hydrogen adsorption at dislocations and cracks in Fe. *Acta Metall.* 26, 1795–1803.
- Gilman, J.J., 1969. *Micromechanics of Flow in Solids*. McGraw-Hill, New York, pp. 185–199.
- Johnson, H.H., 1984. Overview of hydrogen degradation phenomena, in: Gibala, R., Hehemann, R.F. (Eds.), *Hydrogen Embrittlement and Stress Corrosion Cracking*, Proceedings of a Troiano Festschrift Symposium, Case Western Reserve University, June 1–3, 1980. ASM, Ohio, pp. 3–27.
- Kimura, A., Birnbaum, H.K., 1987. The effects of cathodically charged hydrogen on the flow stress of nickel and nickel-carbon alloys. *Acta Metall.* 35, 1077–1088.
- Kumnick, A.J., Johnson, H.H., 1980. Deep trapping states for hydrogen in deformed iron. *Acta Metall.* 28, 33–39.
- Lee, T.D., Goldenberg, T., Hirth, J.P., 1977. Hydrogen and plastic instability in deformed, spheroidized 1090 steel, in: *Fracture 1977*, Vol. 2. University of Waterloo Press, Waterloo, pp. 243–248.
- Lee, T.D., Goldenberg, T., Hirth, J.P., 1979-a. Effect of hydrogen on fracture of U-notched bend specimens of spheroidized AISI 1095 steel. *Metall. Trans. A* 10, 199–208.
- Lee, T.D., Goldenberg, T., Hirth, J.P., 1979-b. Effect of hydrogen on fracture of U-notched bend specimens of quenched and tempered AISI 4340 steel. *Metall. Trans. A* 10, 439–448.
- Lufrano, J., Sofronis, P., 1998. Enhanced hydrogen concentrations ahead of rounded notches and cracks – competition between plastic strain and hydrostatic stress. *Acta Mater.* 46, 1519–1526.
- Lufrano, J., Symons, D., Sofronis, P., 1998. Hydrogen transport and large strain elastoplasticity near a notch in alloy X-750. *Eng. Fracture Mech.* 59, 827–845.
- Matsui, H., Kimura, H., Moriya, S., 1979-a. The effect of hydrogen on the mechanical properties of high purity iron I. Softening and hardening of high purity iron by hydrogen charging during tensile deformation. *Mat. Sci. Engng* 40, 207–216.
- Matsui, H., Kimura, H., Kimura, A., 1979-b. The effect of hydrogen on the mechanical properties of high purity iron III. The dependence of softening on specimen size and charging current density. *Mat. Sci. Engng* 40, 227–234.
- Matsumoto, T., Eastman, J., Birnbaum, H.K., 1981. Direct observations of enhanced dislocation mobility due to hydrogen. *Scr. Met.* 15, 1033–1037.
- McLellan, R.B., 1979. Thermodynamics of diffusion behavior of interstitial solute atoms in non-perfect solvent crystals. *Acta Metall.* 27, 1655–1663.
- Meyers, S.M. et al., 1992. Hydrogen interactions with defects in crystalline solids. *Rev. Mod. Phys.* 64, 559–617.
- Moriya, S., Matsui, H., Kimura, H., 1979. The effect of hydrogen on the mechanical properties of high purity iron II. Effect of quenched-in hydrogen below room temperature. *Mat. Sci. Engng* 40, 217–226.
- Onyewenyi, O.A., Hirth, J.P., 1983. Effects of hydrogen on Notch ductility and fracture in spheroidized AISI 1090 steel. *Metall. Trans. A* 14, 259–269.
- Oriani, R.A., 1970. The diffusion and trapping of hydrogen in steel. *Acta Metall.* 18, 147–157.
- Peisl, H., 1978. Lattice strains due to hydrogen in metals, in: Alefeld, G., Volkl, J. (Eds.), *Hydrogen in Metals I*, Topics in Applied Physics, Vol. 28. Springer-Verlag, New York, pp. 53–74.
- Perrin, G., Leblond, J.B., 1993. Rudnicki and Rice's analysis of strain localization revisited. *J. Appl. Mech.* 60, 842–846.
- Rice, J.R., 1976. The localization of plastic deformation, in: Koiter, W.T. (Ed.), *Proc. of the 14th Int. Congress on Theoretical and Applied Mechanics*, Delft. North-Holland, pp. 207–220.
- Robertson, I.M., Birnbaum, H.K., 1984. Effect of hydrogen on the dislocation structure of deformed nickel. *Scr. Met.* 18, 269–274.
- Robertson, I.M., Birnbaum, H.K., 1986. An HVEM study of hydrogen effects on the deformation and fracture of nickel. *Acta Metall.* 34, 353–366.
- Robertson, I.M., Tabata, T., Wei, W., Heubaum, F., Birnbaum, H.K., 1984. Hydrogen embrittlement and grain boundary fracture. *Scr. Met.* 18, 841–846.

- Rozenak, P., Robertson, I.M., Birnbaum, H.K., 1990. HEVM studies of the effects of hydrogen on the deformation and fracture of AISI type 316 austenitic stainless steel. *Acta Metall.* 38, 2031–2040.
- Rudnicki, J.W., Rice, J.R., 1975. Conditions for the localization of deformation in pressure-sensitive dilatant materials. *J. Mech. Phys. Solids* 23, 371–394.
- Shih, D., Robertson, I.M., Birnbaum, H.K., 1988. Hydrogen embrittlement of α titanium: in situ TEM studies. *Acta Metall.* 36, 111–124.
- Sirois, E., Birnbaum, H.K., 1992. Effects of hydrogen and carbon on thermally activated deformation in nickel. *Acta Metall.* 40, 1377–1385.
- Sirois, E., Sofronis, P., Birnbaum, H.K., 1992. Effects of hydrogen and carbon on thermally activated deformation in nickel, in: Bruemmer, S.M., Meletis, E.I., Jones, R.H., Gerberich, W.W., Ford, F.P., Staehle, R.W. (Eds.), *Parkins Symposium on Fundamental Aspects of Stress Corrosion Cracking*. The Minerals, Metals & Materials Society, pp. 173–190.
- Sofronis, P., 1995. The influence of mobility of dissolved hydrogen on the elastic response of a metal. *J. Mech. Phys. Solids* 43, 1385–1407.
- Sofronis, P., Birnbaum, H.K., 1995. Mechanics of the hydrogen-dislocation-impurity interactions – I. Increasing shear modulus. *J. Mech. Phys. Solids* 43, 49–90.
- Sofronis, P., McMeeking, R.M., 1989. Numerical analysis of hydrogen transport near a crack tip. *J. Mech. Phys. Solids* 37, 317–350.
- Tabata, T., Birnbaum, H.K., 1983. Direct observations of the effect of hydrogen on the behavior of dislocations in iron. *Scr. Met.* 17, 947–950.
- Tabata, T., Birnbaum, H.K., 1984. Direct observations of hydrogen enhanced crack propagation in iron. *Scr. Met.* 18, 231–236.
- Taha, A., Sofronis, P., 2001. A micromechanics approach to the study of hydrogen transport and embrittlement. *Eng. Fracture Mech.* 68, 803–837.
- Thomas, G.J., 1980. Hydrogen trapping in FCC metals, in: Thompson, A.W., Bernstein, I.M. (Eds.), *Hydrogen Effects in Metals*. Trans. Met. Soc. AIME, New York, pp. 77–85.
- Tien, J.K., Thompson, A.W., Bernstein, I.M., Richards, R.J., 1976. Hydrogen transport by dislocations. *Metall. Trans. A* 7, 821–829.
- Xiao, H.Z., 1993. Effects of hydrogen and stress on the microstructure and microchemistry of Ti₃Al-based intermetallic compounds. PhD thesis, University of Illinois at Urbana-Champaign, Urbana, IL.
- Ulmer, D.G., Altstetter, C.J., 1991. Hydrogen-induced strain localization and failure of austenitic stainless steels at high hydrogen concentrations. *Acta Metall.* 39, 1237–1248.
- Zeides, F., 1986. Effect of hydrogen on the mechanical properties and fracture behavior of high purity aluminum. PhD thesis, University of Illinois at Urbana-Champaign, Urbana, IL.